POLYTECHNIQUE MONTRÉAL

affiliée à l'Université de Montréal

Using the Fringe Field of MRI Scanner for the Navigation of Microguidewires in the Vascular System

ARASH AZIZI

Institut de génie biomédical

Thèse présentée en vue de l'obtention du diplôme de *Philosophiæ Doctor*

Génie biomédical

Août 2019

POLYTECHNIQUE MONTRÉAL

affiliée à l'Université de Montréal

Cette thèse intitulée :

Using the Fringe Field of MRI Scanner for the Navigation of Microguidewires in the Vascular System

présentée par **Arash AZIZI**

en vue de l'obtention du diplôme de *Philosophiæ Doctor*

a été dûment acceptée par le jury d'examen constitué de :

Farida CHERIET, présidente
Sylvain MARTEL, membre et directeur de recherche
Nikola STIKOV, membre
Pierre E. DUPONT, membre externe

DEDICATION

To people and the cats who supported me to get to this point in my life, and myself.

ACKNOWLEDGEMENTS

I believe in Sylvain's ideas. Katie Bouman from Caltech took the first picture of a black hole. Sylvain hacked the tumors by opening a way to its hypoxic zone. As long as one says "impossible" to something, there are people like Sylvain who try to make them happen, and science advances.

I appreciate the unique opportunity and all the supports Dr. Martel gave me to work on the project of Fringe Field Navigation.

RÉSUMÉ

Le traitement du cancer, la prévention des accidents vasculaires cérébraux et le diagnostic ou le traitement des maladies vasculaires périphériques sont tous des cas d'application d'interventions à base de cathéter par le biais d'un traitement invasif minimal. Cependant, la pratique du cathétérisme est généralement pratiquée manuellement et dépend fortement de l'expérience et des compétences de l'interventionniste. La robotisation du cathétérisme a été étudiée pour faciliter la procédure en augmentant les niveaux d'autonomie par rapport à cette pratique clinique. En ce qui concerne ce problème, un des problèmes concerne le placement super sélectif du cathéter dans les artères plus étroites nécessitant une miniaturisation de l'instrument cathéter / fil de guidage attaché. Un microguide qui fonctionne dans des vaisseaux sanguins étroits et tortueux subit différentes forces mécaniques telles que le frottement avec la paroi du vaisseau. Ces forces peuvent empêcher la progression de la pointe du fil de guidage dans les vaisseaux. Une méthode proposée consiste à appliquer une force de traction à la pointe du microguide pour diriger et insérer le dispositif tout en poussant l'instrument attaché à partir de l'autre extrémité n'est plus pratique, et à exploiter le gradient du champ de franges IRM surnommé Fringe Field Navigation (FFN) est proposée comme solution pour assurer cet actionnement. Le concept de FFN repose sur le positionnement d'un patient sur six DOF dans le champ périphérique du scanner IRM afin de permettre un actionnement directionnel pour la navigation du fil-guide.

Ce travail rend compte des développements requis pour la mise en œuvre de la FFN et l'étude du potentiel et des possibilités qu'elle offre au cathétérisme, en veillant au renforcement de l'autonomie. La cartographie du champ de franges d'un scanner IRM 3T est effectuée et la structure du champ de franges en ce qui concerne son uniformité locale est examinée. Une méthode pour la navigation d'un fil de guidage le long d'un chemin vasculaire souhaité basée sur le positionnement robotique du patient à six DOF est développée. Des expériences de FFN guidées par rayons X in vitro et in vivo sur un modèle porcin sont effectuées pour naviguer dans un fil de guidage dans la multibifurcation et les vaisseaux étroits. Une caractéristique unique de FFN est le haut gradient du champ magnétique. Il est démontré in vitro et in vivo que cette force surmonte le problème de l'insertion d'un fil microguide dans des vaisseaux tortueux et étroits pour permettre de faire avancer le fil-guide avec une distale douce au-delà de la limite d'insertion manuelle. La robustesse de FFN contre les erreurs de positionnement du patient est étudiée en relation avec l'uniformité locale dans le champ périphérique. La force élevée du champ magnétique disponible dans le champ de franges IRM peut amener les matériaux magnétiques doux à son état de saturation. Ici, le concept d'utilisation d'un ressort est présenté comme une alternative

déformable aux aimants permanents solides pour la pointe du fil-guide. La navigation d'un microguide avec une pointe de ressort en structure vasculaire complexe est également réalisée in vitro. L'autonomie de FFN en ce qui concerne la planification d'une procédure avec autonomie de tâche obtenue dans ce travail augmente le potentiel de FFN en automatisant certaines étapes d'une procédure.

En conclusion, FFN pour naviguer dans les microguides dans la structure vasculaire complexe avec autonomie pour effectuer le positionnement du patient et contrôler l'insertion du fil de guidage - avec démonstration in vivo dans un modèle porcin - peut être considéré comme un nouvel outil robotique facilitant le cathétérisme vasculaire. tout en aidant à cibler les vaisseaux lointains dans le système vasculaire.

ABSTRACT

Treatment of cancer, prevention of stroke, and diagnosis or treatment of peripheral vascular diseases are all the cases of application of catheter-based interventions through a minimal-invasive treatment. However, performing catheterization is generally practiced manually, and it highly depends on the experience and the skills of the interventionist. Robotization of catheterization has been investigated to facilitate the procedure by increasing the levels of autonomy to this clinical practice. Regarding it, one issue is the super selective placement of the catheter in the narrower arteries that require miniaturization of the tethered catheter/guidewire instrument. A microguidewire that operates in narrow and tortuous blood vessels experiences different mechanical forces like friction with the vessel wall. These forces can prevent the advancement of the tip of the guidewire in the vessels. A proposed method is applying a pulling force at the tip of the microguidewire to steer and insert the device while pushing the tethered instrument from the other end is no longer practical, and exploiting the gradient of the MRI fringe field dubbed as Fringe Field Navigation (FFN) is proposed as a solution to provide this actuation. The concept of FFN is based on six DOF positioning of a patient in the fringe field of the MRI scanner to enable directional actuation for the navigation of the guidewire.

This work reports on the required developments for implementing FFN and investigating the potential and the possibilities that FFN introduces to the catheterization, with attention to enhancing the autonomy. Mapping the fringe field of a 3T MRI scanner is performed, and the structure of the fringe field regarding its local uniformity is investigated. A method for the navigation of a guidewire along a desired vascular path based on six DOF robotic patient positioning is developed. *In vitro* and *in vivo* x-ray Guided FFN experiments on a swine model of are performed to navigate a guidewire in the multibifurcation and narrow vessels. A unique feature of FFN is the high gradient of the magnetic field. It is demonstrated *in vitro* and *in vivo* that this force overcomes the issue of insertion of a microguidewire in tortuous and narrow vessels to enable advancing the guidewire with a soft distal beyond the limit of manual insertion. Robustness of FFN against the error in the positioning of the patient is investigated in relation to the local uniformity in the fringe field. The high strength of the magnetic field available in MRI fringe field can bring soft magnetic materials to its saturation state. Here, the concept of using a spring is introduced as a deformable alternative to solid permanent magnets for the tip of the guidewire. Navigation of a microguidewire with a

spring tip in complex vascular structure is also performed *in vitro*. The autonomy of FFN regarding planning a procedure with Task Autonomy achieved in this work enhances the potential of FFN by automatization of certain steps of a procedure.

As a conclusion, FFN to navigate microguidewires in the complex vascular structure with autonomy in performing tasks of patient positioning and controlling the insertion of the guidewire – with *in vivo* demonstration in swine model – can be considered as a novel robotic tool for facilitating the vascular catheterization while helping to target remote vessels in the vascular system.

TABLE OF CONTENTS

LIST OF TABLES

LIST OF FIGURES

LIST OF SYMBOLS AND ABBREVIATIONS

Cath Lab	Catheterization Laboratory
CE	Conformité Européene
CNC	Computer Numerical Control
DOF	Degree of Freedom
FDA	Food and Drug Administration
Fr	French
FOV	Field of View
ID	Inside Diameter
IP	Internet Protocol
IV	Intravenous
MRI	Magnetic Resonance Imaging
OD	Outside Diameter
RF	Radio Frequency
SNR	Signal to Noise Ratio
TCP	Transmission Control Protocol
TE	Echo Time
TR	Repetition Time

LIST OF APPENDICES

CHAPTER 1 INTRODUCTION

The vascular system of humans consists of a complex and interconnected network of blood vessels that spreads across the body to provide nutrition and oxygen for the living cells metabolism. The range of the diameter of the blood vessels varies with 3000-fold between Aortas as the largest artery with an average diameter of 25000 microns to capillaries with a few microns of diameter [1]. Vascular catheterization is the medical procedure of placing a catheter – a tubular and flexible medical device – inside a vascular path to administer a material such as the embolizing agent or place a device like a stent at a desired location within the body [2, 3]. Medical procedures that are based on the catheterization are considered to be a less-invasive alternative to the medical treatments such as surgeries [4-7] or insertion of a needle [8, 9] to perform a certain therapy. Placing a catheter in blood vessels enables to deliver a therapeutic agent to the desired location inside the body through a vascular rout instead of performing surgery to access the site of the problem or toxication of the whole body similar to the chemotherapy. Catheterization of hardly accessed sites inside the body and placing the catheter instrument in the narrow blood vessels and lessening the arduousity of manual catheterization by raising the level of autonomy of the procedure to make it an easy operation to implement would enhance the quality of current catheter-based procedure while enable introducing novel treatments.

Surgery is a traditional approach to treat the problematic area inside the body[10-12]. The robotic system of Da Vinci [13, 14] was developed to minimize the invasiveness of certain surgeries by performing the operation through the insertion of the robotic endoscopic hands and camera inside the body through small punctures made on its surface to minimize the pain and the post-operation complications for the patients while facilitating the operation by adding robotic precision. Insertion of a needle into the body had also been investigated as a solution to minimize the invasiveness of the surgeries when the treatment requires administration of a drug or ablation of a bulk of malignant cells inside the body [15]. Inserting needles for the RF or cryogenic ablation of cancerous tumors inside the liver [16], prostate [17], pancreas [18], etc. have already translated to the clinical setting. A recent project called EDEN 2020 aims to develop a method for local therapy and drug administration inside the brain based on the insertion of a bioinspired deformable needle into the brain tissue as a substitution for the surgeries [19]. Radiation therapy uses ionizing radiation for the destruction of malignant cells while eliminating the need for access to the problematic site[20].

In focal ultrasound surgery, the energy for damaging the malignant cells is concentrated at a focal point through using its specific transducer allowing to perform a focal surgery at a deep location within the body without harming surrounding healthy tissues[21].

Catheter-based treatments are investigated for the development of less-invasive alternatives to traditional treatments in cardiology[22], interventional oncology[23], and treatment of the vascular diseases[3]. Manual or robotic catheters can enter the within the heart from the path that blood gets inside of it. Then, operation inside the heart chambers without affecting the functioning of this vital organ by passing through its valves and the septum wall to provide access to interior surface and tissue of the heart becomes possible. It has had a significant impact on developing novel minimally invasive methods of diagnosis and treatment in the cardiology[24]. Diagnosing the vascular diseases in coronary arteries, cerebrovascular arteries, and peripheral arteries by the injection of a contrast media (CM) into the vessels and use radioscopy to detect occlusion or abnormality that impairs the circulation had been used for decades, and currently, catheters are developed for intravascular imaging based on Optical Coherence Tomography and Ultrasound technologies[25]. Use of the catheters to access the diseased site in the peripheral arteries is now a clinical alternative to vascular bypass surgery in different branches of Aorta in the abdomen [2], coronary arteries[26], carotid[27], etc. Angioplasty is a term used to describe the procedure of widening an obstructed blood vessel and it is done by insertion of a balloon catheter with an inflatable part at its distal to widen the occlusion in the vessels. For a more long term – and effective – treatment, placement of a stent – which is a tubular wired structure – at the problematic site in the vascular system is utilized to treat the cause of occlusion by eluting the drugs attached on the stent which is in direct contact to the cause of occlusion [26, 28, 29]. The need for the removal of stents from the body has led to the development of biodegradable stents[30, 31]. Arrhythmia in the functioning of the heart can be diagnosed by Cardiac Electrophysiology (EP)[32, 33] and treated by focal ablation [34]. The device for collecting the electrophysiology signal from the internal surface of the heart tissue or performing the ablation of the tissue of the heart to regulate the heartbeat rhythm is integrable into a catheter that operates within the heart [35].

Interventional oncology is another vast place for using the catheter.s The first practice of chemotherapy was done by administration of a drug based on the mustard gas agent to the body of the terminally ill patients to treat cancer[36]. As an alternative to chemotherapy which relies on

systemic circulation of toxic drugs across the body, one approach is Transarterial Chemoembolization (TACE) that is based on blocking the blood vessels that supply blood to the solid tumors by local administration of embolic agents through a catheter priory placed in a desired blood vessel [9, 15, 23]. Currently, TACE is counted as one of the options for the treatment of Hepatocellular carcinoma cancer, which is the most common type of liver cancer. Unique vascular anatomy of the liver allows performing full embolization of the hepatic artery or its major branches to perform TACE. However, Super-selective catheterization of the arteries that feed the tumors is required to achieve better treatment result[37] as TACE is applicable to any type of cancer with a solid tumor. This need also has led to the development of drugs and methods for non-systemic delivery of the therapeutic agents to the tumors [38-42]. So, if it is difficult to place the tip of the catheter as close as possible to the tumor, these new technologies enable to navigate drugs along the path between the point of injection – or the tip of the catheter – to the tumor to enhance the efficiency of the therapy. All of the catheter-based procedures discussed here are the clinical options for the treatment of the major causes of mortality and illness across the world including cardiac arrest[43, 44], stroke[45], and cancer[46, 47].

Developing new devices that can operate inside bodily environments to perform a local diagnosis or treatment have been actively investigated for applications in medicine [48]. Development of new materials and robotic medical agents is a growing field in biomedical engineering domain [38-41, 48-59]. Currently, nano/micro/mili scale synthesis or biohybrid robotic systems with different modes of locomotion[50, 51] are developed for operation inside the body and various methods of actuation including the magnetic field [39, 55, 57, 60], light[61], ultrasound[62], biological motors[63, 64], and chemical propulsion [65] have been exploited for the mobility of the devices. Drug delivery to the hypoxic zone of the solid tumors has been realized by dispatching a swarm of bacteria with Aero-Magneto taxis capability that propels with its flagella and is sensitive to the gradient of the oxygen concentration and can rotate by the magnetic field [66, 67]. Helical micro swimmers have been investigated to operate in various bodily fluid for imaging and treatment purpose [55, 57, 58]. Soft-bodied small-scale robots are emerging to answer the problems regarding the mobility of the robots to pass obstacles to enable moving in different environments in the body[50]. Shapeshifting soft-bodied micro-robots with the high motility in complex channels can swim in the viscous flow are developed to reach remote locations [51]. All of these advances

promise to enhance life quality by introducing novel medical treatments. Mainly, these advances require vascular catheterization to deliver the agent or device to the desired target inside the body [68].

No wonder that vascular catheterization is reshaping the therapies, and the scope of the catheter-based operation is expanding. However, endovascular catheterization is a growing field and acquiring the skills required to perform a procedure is a dynamic process which highly depends on the experience of the practitioner [2, 3, 69]. Tackling this issue has been confronted by developing robotic systems for catheterization [70-75]. Application of robotic system in the catheterization had been successful for applications in cardiology, and many clinics across the world have adopted robotic systems for the cardiac interventions [4, 7, 74-77]. However, developing robots for selective and super-selective navigation of the catheters in the complex vascular systems is still in its infancy as the most prominent robotic systems for vascular catheterization with FDA approval – e.g. Amigo robotic catheter and Magellan (Hansen Medical) – are capable of targeting major peripheral arteries while the caliber of the catheter does not allow further advancement in the vascular system.

With applications in the interventional oncology or the treatment of the vascular diseases, roboticization of vascular catheterization can facilitate reaching to a desired – and even remote – site in the vascular system. By passing multiple branches to access a location deeper inside the vascular system, the tortuous blood vessels become narrower[1]. It requires miniaturization of the guidewire instrument and the systems for actuation in order to target narrower vessels[69, 73]. Miniaturization of the instrument results in the decrease of its stiffness until steerability becomes unpractical while pushing the instrument at the insertion site to counteract the opposing friction forces being amplified by the added surface in contact against the vessel walls and caused by the bending of the instrument [73]. Applying magnetic torque on the tip of the catheter has been used in different applications for steering catheters [71, 74, 75, 77]. However, miniaturization of the catheter and reducing the stiffness to target smaller vessels, adds new complexity for insertion of the device[69, 73]. Therefore, applying a pulling force on the tip of the guidewire is considered as a way to resolve this problem and the magnetic gradient force was introduced to overcome this challenge. In [69], the gradient of up to 0.5 T/m was used for steering of a microguidewire in the peripheral arteries of a rabbit model. Fringe Field Navigation (FFN) was introduced to exploit the

gradient (up to 4T/m) of the magnetic fringe field of the clinical MRI scanners for the navigation of the guidewires[73]. The strong pulling force provided by the fringe field was the mean to enable insertion of the guidewires with a soft and floppy distal in the narrow vessels.

The initial experiment of FFN demonstrated the possibility of steering microguidewires in multibifurcation models. However, the initial experiments had limitations. The MRI Fringe Field is a static field and so providing directional actuation requires relative 6 DOF positioning of the patient and the magnetic field. While the MRI scanner is way heavier than the patient, positioning of the patient by a robotic system is proposed as the solution to provide the required directional actuation. The first limitation of the initial FFN experiment was the lack of the essential 6 DOF patient positioning [73, 77]. Second, the experiments were limited to using the center axis of the MRI fringe field which the direction of the magnetic field lines and its gradient. FFN is proposed to navigate microguidewires with a magnetic body attached at its tip in the 3D vascular systems. Another problem along the way of FFN project is the retrieval of the guidewire through a small catheter – a microcatheter [69]. This problem arises from the fact that retrieving a microguidewire which has a magnetic tip with a size larger than the diameter of the shaft of the guidewire requires a larger caliber of the catheter. It may lead to the impossibility of using a microcatheter for a procedure.

1.1 Contribution of this project

The Main goal of this project was to investigate if a pulling force applied on the tip of a guidewire enables to navigate a microguidewire to a location beyond the limits of traditional approaches or the methods that solely rely on the bending the tip of the instrument. In other words, this project aimed to demonstrate that a pulling force applied on the tip of a floppy and soft microguidewire allow advancing the instrument in narrow vasculatures. In FFN, providing this force at a remote location within the vascular system is provided by exploiting the gradient of the magnetic fringe field around the MRI scanners. In fact, this work tries to investigate if FFN can push the boundaries of robotic catheterization in targeting smaller vessels. In parallel, developing a robotic method to enhance the level of autonomy and reduce the need for the experience from the practitioner had high importance in this project.

This work reports on the developments to implement the FFN by six DOF robotic positioning around an MRI scanner and the results of the navigation of microguidewires. Chapter 3 presents developments, either materials or methodologies, to perform FFN experiments. The developments aim to increase the level of the autonomy of the procedure. In Chapter 4, results of *in vitro* experiments of FFN are presented for the (1) navigation of a guidewire through multibifurcation and narrow vascular paths, (2) demonstrate the impact of the magnetic gradient force to insert a guidewire beyond the limits of manual insertion, (3) the possibility of the miniaturization of the instrument in FFN, (4) and robustness in FFN against error in the 6 DOF patient positioning. In Chapter 5, the results of *in vivo* experiments of FFN on a swine animal model to navigate a microguidewire in cerebral arteries. Also, the impact of the pulling force provided by the fringe field to insert microguidewires in narrow blood vessels is demonstrated *in vivo* as well. Chapter 6 presents the concept of a new magnetic body for the tip of the guidewire as the basis of developing a deformable magnetic tip which is not a permanent magnet and can saturate in the fringe field, to facilitate the retrieval of the guidewire through the smaller catheters. General discussion, conclusions, and recommendations for the future work on FFN are presented in chapters 7 and 8.

CHAPTER 2 LITERATURE REVIEW

Endovascular interventions are reshaping the methods and approaches of treatments and the scope of the catheter-based procedures are broadening by introducing novel minimally invasive methods of treatment and diagnosis. The main categories for the application of the catheter-based interventions are in the cardiac intervention [4, 78], diagnosis and treatment of the peripheral vascular diseases[2, 3, 6, 11, 78-80] and interventional oncology[9, 15, 23]. Conducting a successful intervention requires different knowledge, skills, and experience. Adapting eye and hand to the fluoroscopic image (fluoroscopy-eye-hand coordination), prediction of the interactions between the guidewire and the vessels (particularly at the site of the lesions), choosing the right combination of the catheter and the guidewire, and knowing the limits of an intervention to determine the end of a procedure, are some of the necessary endovascular skills. To prepare the interventionist to perform an intervention, development of the catheter-guidewire skills has high importance. Acquiring the skills relies on the experience of the practitioner and the number of interventions they have participated is considered as a criterion to evaluate their qualification to perform a specific procedure. To emphasize the importance of experience in performing an intervention, Table 2.1 provides examples on the recommendation of different endovascular societies on the number of the cases it takes for a new physician to qualify to perform an endovascular intervention[2].

Table 2.1 number of the interventions when an interventionist qualifies

	SIR	SCAI	ACC	AHA	SVS
Angiogram	200	100/50[a]	100	100	100/50[a]
Intervention	25	50/25[a]	50/25[a]	50/25[a]	50/25[a]

[a] As primary interventionist.

Abbreviations: SIR, Society of Interventional Radiology; SCAI, Society for Cardiac Angiography and Interventions; ACC, American College of Cardiology; AHA, American Heart Association; SVS, Society for Vascular Surgery.

2.1 Brief about the catheterization procedure

In this section, a concise introduction of the steps of catheterization is presented. These explanations are supported with the examples from *in vivo* experiment that was performed for this

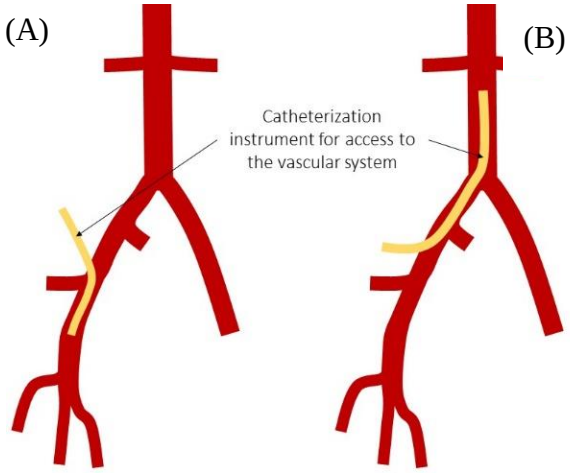

Figure 2.1 Schematic example of (A) retrograde and (B) antegrade access to the femoral artery

project. A catheterization procedure begins with the preparation of the patient. It includes putting the patient under anesthesia (local or general) and intubation of the respiratory tract. After preparation of the patient, the initial step in a catheterization procedure is accessing the vascular system. This step begins by making a puncture on the skin to open a way to insert the catheter device in a major blood vessel. There are different vessels considered for accessing the vascular system including femoral artery, brachial artery, subclavian artery, and carotid artery. The femoral artery which passes at the groin is the most common artery for vascular access. The access can be performed retrogradely or antegrade depending on the location of the target. For instance, antegrade access to the femoral artery is required for intervention in the popliteal artery which is in the lower limbs while retrograde access is needed for entering the device in the Aorta. A wrong decision for the access can make a simple intervention difficult, or make a difficult intervention impossible. Figure 2.1 represents a schematic example of the concept and the direction of the vascular access for an intervention. Finding the right site of the puncture on the skin is important to reduce the damage to the tissue of the patient and related complications. Some of the complications regarding the vascular access are bleeding either minor or major, perforation of the vessel, or infection[81-83]. Different external landmarks such as features on the skin or bony landmarks or landmarks that are visible under radioscopy like the location of the head of the femur bone are considered as the ways to find the site of the puncture. Radioscopy is the common approach to find the optimal location of the site of puncture. This approach was also used to find the site of the puncture in *in vivo* experiments in this work. Figure 2.2 shows an example of an X-

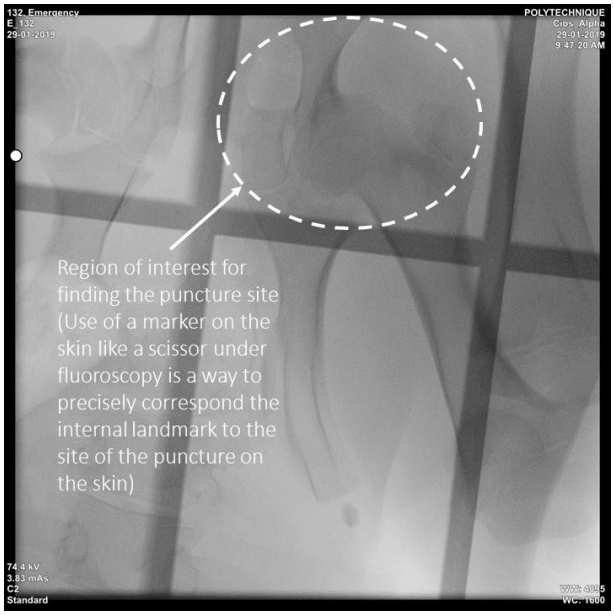

Figure 2.2 Example of an X-ray image taken for localization of the site of the puncture for access to the femoral artery of a swine animal model

ray image taken for finding the location of the puncture for access to the femoral artery in a swine model by finding the head of the femur. Use of ultrasound imaging (Doppler ultrasound) to guide the procedure is another approach for image-guided vascular access[84].

After finding the artery, insertion of a needle inside it opens the way into the vascular system. Backflow of the blood out of the needle is the way to validate that the needle is inside the artery. Then, a guidewire passes through the needle into the artery. This step is followed by withdrawing the needle and insertion of the sheath over the guidewire into the accessed vessel. The sheath is used to provide secure access for the insertion of the other devices (catheters and guidewires). Inserting a dilator into the sheath is also a common practice to stabilize the vascular access [2].

After access to the vascular system by placing a sheath, it is the time for the guidewire-catheter operation to reach the desired target. The catheter and the guidewire are complementary to each other. The whole procedure to navigate a catheter into the location of the target in the vascular system is done by the use and exchange of different guidewire and catheters during a procedure. There are different criteria in choosing the right combination of the instruments. Length, diameter, coating, stiffness and the shape of the tip are the basic features to choose the right device for an intervention. Some other features that distinguish guidewires from each other are variation in the

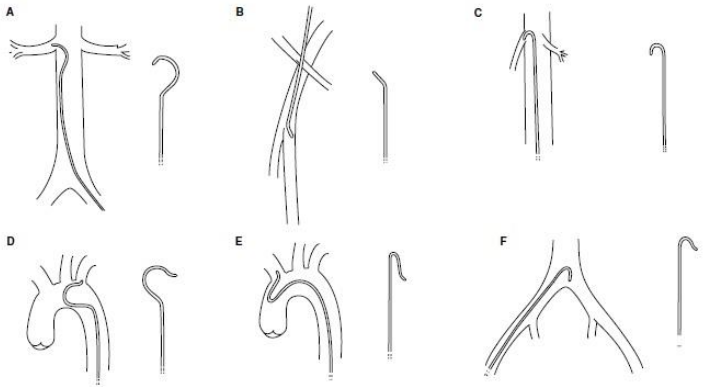

Figure 2.3 Example of catheters with a custom tip in action [2]

stiffness of the shaft along its length, high torque transfer between the shaft and the tip, or length of the floppy distal of the guidewire. The material of the guidewire is another important criterion especially for its visibility under X-ray or in a more advanced application, its compatibility with magnetic resonance imaging in MR-guided interventions[85, 86].

The shape of the tip of the guidewire is an important feature that enables steering into bifurcations. Certain shapes or hooks at the tip are considered to facilitate specific interventions and to facilitate insertion into a vascular branch. When a guidewire has reached near the location of a bifurcation, specific shapes of the tip would be prone to advance easier into the desired vascular branch. Same as the guidewires, catheters are developed with the different shape at their tips for the navigation into different vascular branches. Figure 2.3 shows some different selective catheters in action. Also, various types of catheters exist which their characteristics differ from each other based on their application. Catheters for the navigation, catheters for angiography and catheters that are used for exchanging devices during an intervention have specific features depending on their application. This variation in the type of the devices and the will of the physicians in choosing a combination of the catheter and guidewire based on their experience is a reason for considering the endovascular skills to be a dynamic process.

Size of the diameter of the catheters is defined in French Scale (Fr) and each 3 Fr is equal to 1mm. Guidewires and catheters are produced with different diameter, and currently, micro-catheter/guidewire devices are widely in use. The devices with a smaller size, e.g., the guidewire with a diameter of 0.014-in, are used for navigation inside narrower arteries like coronary arteries

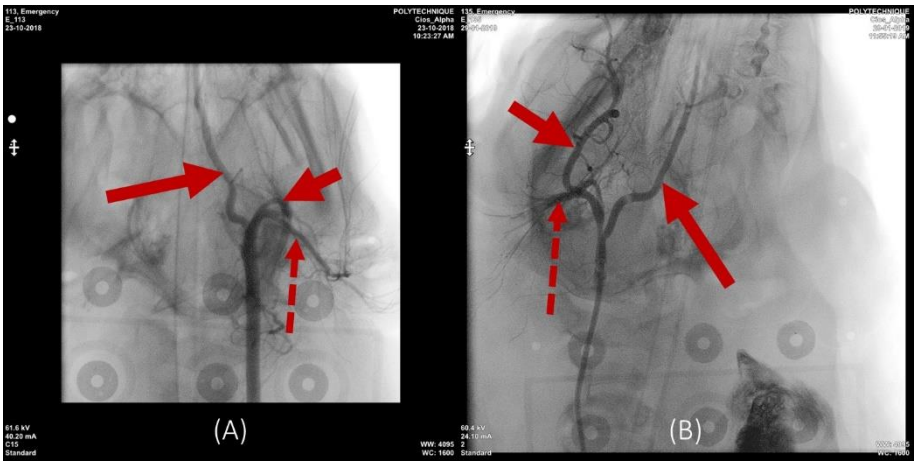

Figure 2.4 Example of the orientation of the cerebral arteries in a swine animal model. The long arrow points lingual artery, the short arrow points to the external carotid artery

which its diameter is between 1 to 4 mm[2]. It is because using a larger caliber of the guidewire or catheter can limit the blood circulation in narrow arteries, or larger devices can induce higher mechanical forces on the vessel walls. To improve the blood circulation, administration of heparin (systemic) to reduce the blood viscosity with more impact on the plasma's viscosity and to reduce the chance of thrombosis is also considered[2, 87].

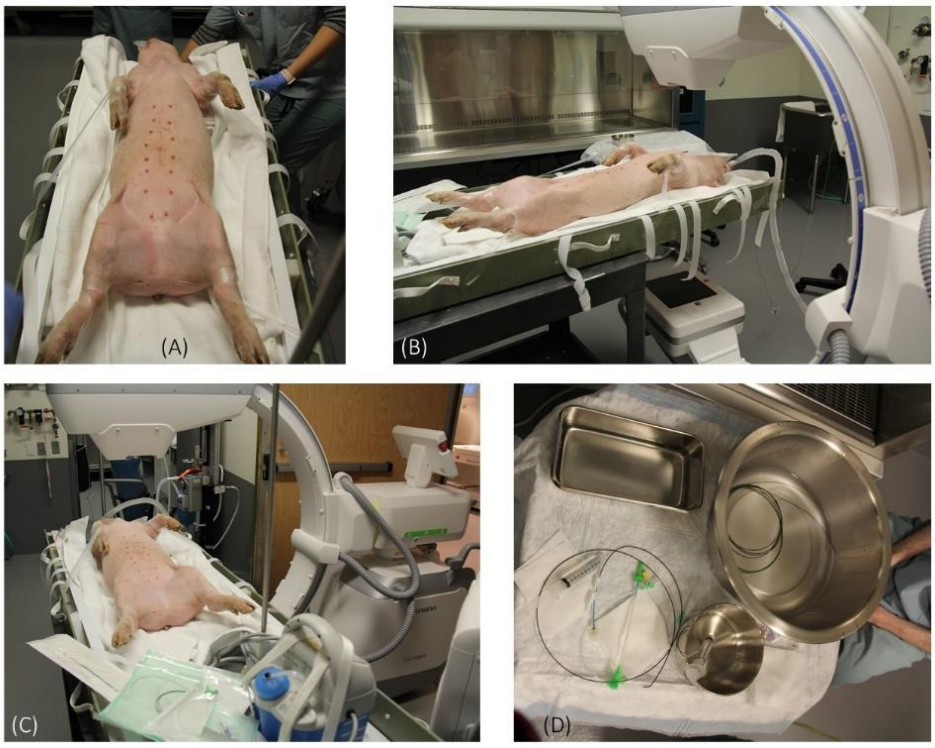

Figure 2.5 Steps for the preparation of the animal prior to the surgery for the catheterization

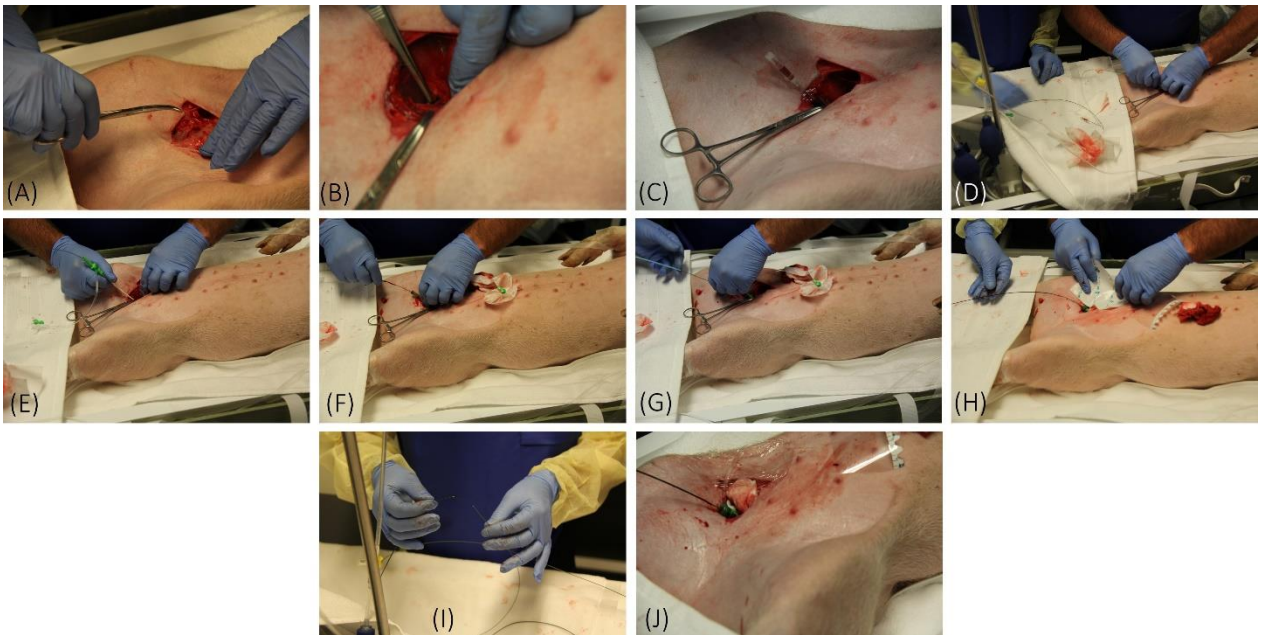

Figure 2.6 Illustration of the steps of access to the femoral artery of a swine model

A consideration regarding fluoroscopy-guided intervention is that the 3D vascular structure is projected on a 2D image. Understanding the spatial direction of the vessels on a 2D image requires a knowledge of the vascular anatomy. Figure 2.4 is an example of two different views of the X-ray imaging of the cerebral arteries of a swine animal model performed during *in vivo* experiments of this work.

Figures 2.5 and 2.6 show images to illustrate some of the concepts and steps for a catheterization procedure. The images are related to the procedure of catheterization of the common carotid artery of a swine animal model. Figure 2.5.A shows the animal prepared for the surgeries and the catheterization after putting under general anesthesia. Figures 2.5.B and 2.5.C show the animal on the patient table under the X-ray, and Figure 2.5.D shows the catheter and guidewires that are sterilized and prepared for the intervention. In Figure 2.6, (A) is the step of puncturing the skin to find the femoral artery shown in (B). Insertion of a needle into the femoral artery and introducing a guidewire to keep the vascular access is shown in (C) and (D). Then, the needle is withdrawn, and the sheath is introduced (E), the initial guidewire (F) and the dilator (F) are removed to insert the guiding guidewire (H) inside the body. Then the guiding catheter is inserted over the guidewire (I), and the location of the access is secured (H).

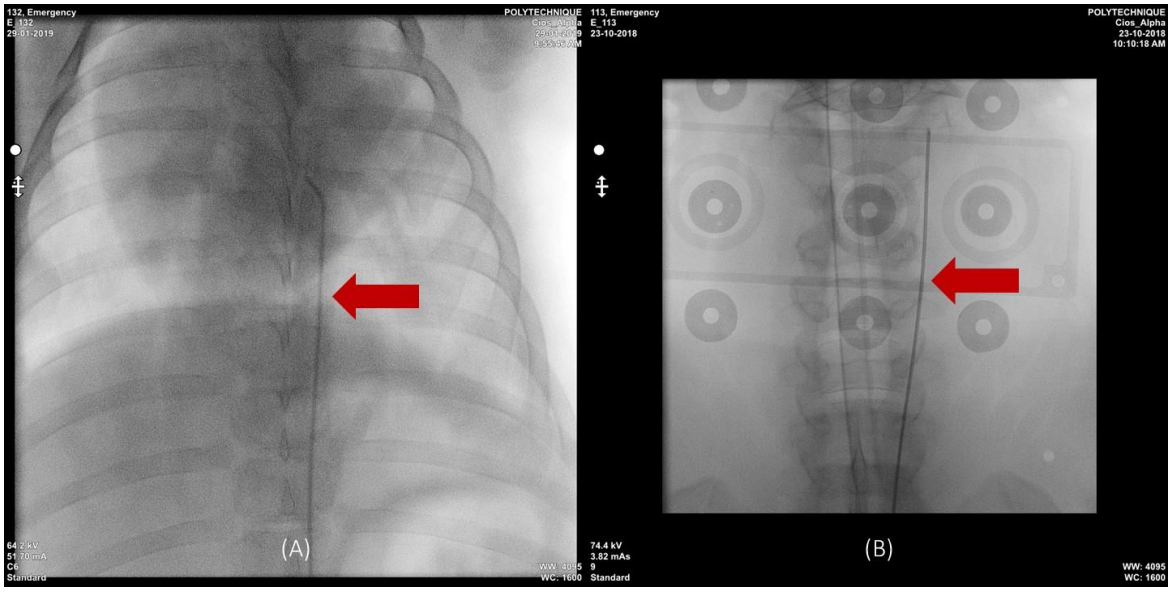

Figure 2.7 Examples of showing the catheters under X-ray in (A) Aorta and (B) carotid artery of a swine model. Arrows point to the catheters.

2.1.1 Hazards and complications

As mentioned before, fluoroscopy-eye-hand coordination is an essential and important skill that an interventionist has to develop during the training. It is because the visualization of the devices and the blood vessels inside the body is most often done under fluoroscopy and navigation is done by manually turning and insertion of the guidewire. Blood vessels are invisible under X-ray as shown in Figure 2.7. To make the visible in radioscopy, interventionists administer contrast media (CM) into the blood vessels through the catheter, and this material visualizes the blood vessels under the x-ray. The common types of CMs are iodine and barium based. Both of the exposure of the body to ionizing X-ray radiation and intravenous administration of CM[88] could leave adverse effects on the patient. The CM may induce the nephrotoxic effect on the kidney and the renal function[2, 3]. Limiting the time and intensity of the x-ray exposure to the patient and dosage of the administered CM is beneficial for the health of the patient.

Exposure to x-ray is also an issue for the team of the intervention as they are periodically exposed the hazardous radiation. A study on the interventional physicians with a brain tumor found that in 85% of the patients, the tumor has been developed on the side of the brain which typically faces

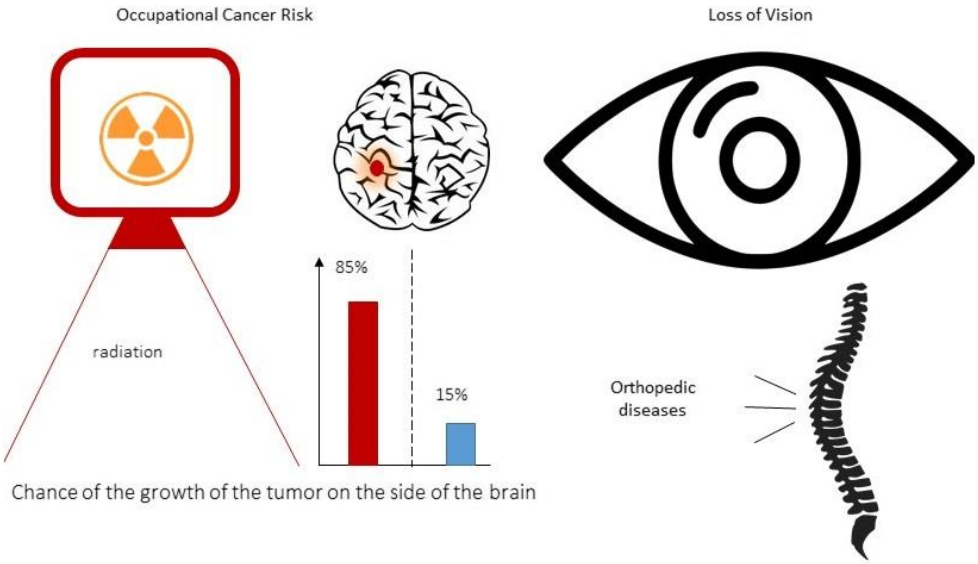

Figure 2.8 summary of the occupational hazards of exposure to x-ray for the Cath Lab crew

the x-ray source[89]. Loss of vision is another side effect of the x-ray on the crew of the intervention. It is found that 50% of the interventional cardiologists and 41% of the nurses and technicians of the Cardiac Cath Labs has significant posterior subcapsular lens changes[90]. To limit the side effects of x-ray exposure, the crew protect themselves by wearing a lead apron that blocks the x-ray. However, the heavy protective apron is a cause of ergonomic issues for the personnel[91]. Regarding this issue, a study found that 49% of the cardiac interventionists have suffered orthopedic injuries as a direct result of their work[78]. Figure 2.8 summarizes the major occupational hazards for the crew of the Cath Labs due to being exposed to X-ray radiation.

While endovascular intervention is counted as a less invasive alternative to the surgeries, different complications with various prevalence and mortality rates are associated with them. These complications cause discomfort and health problems for the patient and can prolong the period of healing or even lead to death. The most common cause of the complications is stated to be the mechanical interactions between the catheter and the interior wall of the blood vessels. Arterial spasm, hemorrhage, and occlusion followed by the vascular trauma are some of the complications related to the mechanical interactions and forces applied to the vessel walls. Nephropathy and renal failure are complications related to the usage of contrast media. Improvement in the design of the catheter devices to passively protect against these complications is a common way of reducing the likelihood of the occurrence of these complications[2, 3, 81].

2.1.2 Selective Catheterization

Vascular catheterization is coded (catheter placement code – CPT) as selective and non-selective procedures[92]. Non-selective catheterization is the placement of the catheter in the accessed vessel, for example for the case of aortic aneurysm repair [2]. Selective catheterization is the placement of the catheter into a branch of the accessed artery, e.g., one of the main branches of Aorta. Selective catheterization permits focused arteriography and delivery of the therapeutic devices. Improving the technologies in endovascular intervention allows placement of the catheter in all the branches of the Aorta. The meaning behind this technological advancement is the development and availability of a wide array of catheters and guidewires with various specifications as well as technics for the catheterization of different vascular branches. Major peripheral arteries of the Aorta are iliac, femoral, renal, superior mesenteric, celiac trunk to the hepatic artery, subclavian, and carotid artery. The main reasons for performing a selective catheterization are either for diagnosing or treatment of the arterial diseases such as the diagnosing of vascular occlusion with an angiogram[82] or stent placement in the carotid artery[27]. An essential consideration in selective catheterization is to insert the guidewire far enough into the vascular branch (bury the guidewire) to minimize the risk of dislodging the guidewire during the step of the insertion of the catheter[2]. Different factors are considered in choosing the right catheter or guidewire to navigate into the vascular branches. For example, a lesion at the bifurcation or the branch of the vessel influence this decision. In the end, the interventionist chooses the type of guidewire-catheter and the strategy of the intervention.

2.1.3 Super selective catheterization

Placement of a catheter in the branches of the accessed vessels is called selective catheterization. Advancing the procedure by further insertion of the catheter and passing more bifurcations is called superselective catheterization. Vascular diseases are not limited to happen in the accessed vessel or its main branches. For instance, the occurrence of an aneurysm or occlusion of the cerebral arteries which is a cause of the stroke can take place in any cerebral artery. By the increase of the number of the bifurcations between the Aorta and the problematic site in the vascular system, the blood vessel becomes narrower, and access would become more challenging to perform. However, providing an efficient and long-lasting therapy for the patient with less-invasiveness makes

endovascular treatment approach an effective treatment option with less-complications for the patients.

Superselective catheterization is also used in interventional oncology and repair of vascular anomalies. Superselective catheterization of the branches of the superior mesenteric artery and the hepatic artery is performed for super selective angiogram[93] or transarterial chemoembolization (TACE) of blood vessels that supply blood to a problematic site[94]. In TACE, embolization of the blood vessel that supplies the cancerous tumor while avoiding blockage of the other arteries is essential and ideal. Some examples of using the super selective catheterization in the abdominal region are the treatment of polycystic liver disease[95], Hepatocellular Carcinoma[23], aneurysms[96], pancreatic angiogram and embolization[97], and Colonic embolization[98]. Catheterization of the ophthalmic artery which is a branch of the internal carotid artery is performed for the treatment of retinoblastoma[99]. Superselective catheterization of the branches of the renal artery[100], and iliac artery[101, 102] are also other examples of super-selective catheterization. In the end, the importance of superselective targeting in the vascular system is to increase the efficiency by local access to the site of the disease.

2.2 Advancements in drugs and delivery

Introducing the cytotoxic concept to the oncology dates back to the period after world war II which mustard gas agent was used for the treatment of lymphoma[36]. Since then, the development of new drugs and methods continued in order to develop an effective method with fewer side-effects for the patients. TACE is a treatment option in oncology which aims to deprive the cancerous cells of the nutrition for their longevity by blocking the blood vessels that feeds them while degradation of the embolic agents releases the chemo drugs into the tumor to enhance the efficiency of the therapy [103]. Currently, different types of embolic agents are developed in the forms of microspheres[42], and injectable coils [104]. Administration of these drugs requires catheterization of the arteries that feed the cancerous cells to avoid blocking the vessels that feed the healthy cells. Catheters provide a direct exclusive route from the syringe that contains the drug to the desired location. This local drug delivery is highly advantageous over the chemotherapy which relies on the systemic drug delivery[39, 40]. TAE or TACE is currently a treatment option for cancer in the liver because of its unique vascular anatomy as the liver has two blood supply.

Local delivery of the drug is important to increase the quality of therapy and reduce the side effects. In TACE, the embolic agents flew with the systemic blood circulation after releasing from the tip of the catheter. Navigation of the drugs at the bifurcations to selectively deliver them to the target has become a novel field in biomedical engineering that comprises the development of the navigable drugs and the method for the navigation. Using magnetic actuation is a promising method for the navigation, and the development of the magnetically navigable drugs and the methods of navigation have been investigated as well. Regarding the drug, the development of the micro magnetic particles (MMP) as an embolic agent is already achieved and material with different size and magnetic characteristics are developed[42, 105]. Methods for the navigation have been developed based on using the gradient of the MRI scanner dubbed as magnetic resonance navigation (MRN) to apply a directional force on the particles[105, 106]. The magnetic gradient of the MRI scanners is limited to 40mT/m, so Dipole Field Navigation which is based on distorting the uniform magnetic field inside the MRI scanners by the insertion of a magnetic body inside the MRI bore was introduced to produce a higher gradient of up to 0.4T/m and beyond for the purpose of navigation [107]. These methods aim to deliver the magnetic therapeutic agents to the desired target through a vascular route from the point of release of the drug which is the tip of the catheter. Placing the tip of the catheter closer to the target helps to increase the efficiency of these methods therapy.

The methods based on embolization aim to kill the cancerous cells by starving them by closing the passages to the tumor. A big challenge in oncology is the delivery of the drugs to the hypoxic regions within the tumor. A recent breakthrough reported the possibility of targeting the hypoxic region in the solid tumors by use of aero-magneto taxis feature of a certain bacteria that can also carry a drug loaded on its surface. Catheterization of the blood vessels that go to the tumor is a way to increase the delivered amount of the dose of the injected drug to the tumor[66, 108].

Another research has introduced the possibility of passing the blood-brain-barrier to deliver magnetic particles to the tissue inside the brain by use of high frequency reversing magnetic field and use of the hyperthermia effect to kill the cancerous cells inside the brain. This work is extended to the case of passing the blood-retinal-barrier. Application of this method is also in the local drug delivery inside the brain. Catheterization of the blood vessels that reach the desired target for the delivery of the drugs is essential for this application to increase the amount of the drug delivered

to the site of the tumor while minimizing the chance of damaging brain cells due to hyperthermia effect[109, 110].

2.3 MRI-guided catheterization

MRI offers different advantages in comparison with other medical imaging modalities. First, no ionizing radiation is used in MRI. It is advantageous for the patient as well as the interventionists. MRI image allows to orient the slices in 3d volume to see the vascular anatomy from different angles. The dosage of Gadolinium CM used in MR angiography is less than the Iodine CM used in fluoroscopy which may cause nephrotoxicity. More importantly, MRI provides soft-tissue contrast to distinguish between different tissues and blood vessel and no harmful effect from 1.5T and 3T MR imaging on the patient has been reported. These advantages have made endovascular interventionist interested in developing MRI-guided methods for catheterization. In the past decades, research on developing methods and devices to perform an MR-guided endovascular intervention have been actively pursued [85, 86].

Safety of a new type of intervention has to be at first validated with experiments on the animal models. In the development of MRI-guided endovascular interventions, a vast body of the work is reported in the MRI-guided catheterization in an animal model. Different cases of fully MRI-guided catheterization of hepatic artery in swine[111], stenting of aorta and filter placement in vena cava vein in swine[112], real-time MRI-guided intervention of renal artery for angioplasty and stent placement[113] and in-vivo visualization and tracking of an active catheter in carotid[111] and renal artery[114] in the swine animal model have been reported are some of the examples of MRI-guided interventions.

Results of successful cases of MRI-guided endovascular interventions on human have also been reported in the last two decades. In 1997, the first case of MRI guided endovascular intervention in a human was reported[85, 115]. In this work which aimed to navigate a catheter in the basilica vein of a human, passive tracking of the catheter with MR imaging was performed for guiding the intervention. In [116], results of MRI-guided cardiac catheterization in children and adults are reported. Also, MRI-guided cases of endovascular intervention in human for angioplasty of femoral artery stenosis[117], and some other examples [85] are reported as other cases of using MR imaging to guide an endovascular intervention.

2.3.1 Devices

The high strength of the magnetic field, the high gradient of the MRI fringe field and the RF waves used in magnetic resonance imaging makes it challenging to develop systems and devices to work in an MRI facility. These factors, especially the compatibility of the device with MR imaging, have impacted the progress in the field of MR-guided endovascular interventions. In fact, the progress of MR-guided interventions has not yet reached to a level appropriate for clinical translation due to the complexity of the development of MRI safe and compatible devices with appropriate mechanical characteristics for endovascular interventions [118-120]. Use of metals for the cores and/or braiding in the catheter and guidewire instruments are common in endovascular devices to provide adequate torque/push/pull-ability as well as radioscopy visibility. The metallic alloys like nitinol that use of them in the fluoroscopy-guided intervention is safe are conductive of electricity or magnetic permeable. The Problem with the use of conducting materials in MR-guided intervention is the heat induction in the instrument from the radiofrequency pulses of MR imaging. Besides, deterioration of the MR image from the susceptibility artifact is another obstacle in use of the metallic alloys, even in a limited quantity, in the devices for MRI-guided intervention. Limiting the use of metallic material to develop MRI-compatible devices leads to lower torsional and bending stiffness and so steerability of the device which leads to the difficulty of the navigation [116]. Based on the literature, and the survey performed by the author of this thesis on the website of the major producers of the interventional devices, no catheter or guidewire instrument is available that has received FDA approval for MR-guided intervention[118].

Many groups and companies have developed MRI-compatible products each designed for specific intervention like cardiac electrophysiology, renal and cardiac catheters, catheters for biopsy and catheters for tracking but only a few of these productions are suitable for translation to the clinical use. The first guidewire that featured conditional MRI-compatibility received CE mark in 2012. Use of PEEK in developing MRI-compatible guidewires as an alternative to the nitinol is common, and fiber-reinforcement of the guidewire is considered as a solution to improve the mechanical properties of the guidewires. However, guidewires that are reinforced with fiberglass are prone to disrupter during an intervention. The use of nylon and peek have been suggested for braiding of the catheters to make MRI-compatible catheters with improved mechanical characteristics. In

general, the state of the MRI-compatible endovascular devices is still behind the state of translation to the clinical use, and research on developing appropriate devices has to continue[118].

2.3.2 Passive and active imaging

The method of imaging and tracking the device inside the body is an essential part of an MR-guided intervention. Real-time MRI for tracking of the devices inside the moving anatomy with proper resolution without any danger for the patient is the ideal condition. One approach which has been widely investigated in different work is incorporating MRI-visible markers along the shaft of catheter or guidewire[85]. These markers either reduce or amplify the MR signal to make a difference in the contrast of the image. It has been done by the use of paramagnetic rings attached to the device[115] or administration of paramagnetic contrast agent in the lumen of the catheter[121]. These approaches do not require additional hardware or post-processing of the image and are called **passive tracking**. Another approach, called **active tracking**, is done by inducing an electrical current in a circuit integrated to the catheter to generate a local distortion in the magnetic field that results in voiding MR signal at the location of the distortion. In these methods, induction of current can be synchronized with the imaging sequence to differentiate between the images created in two switching states of ON/OFF to track the device. Methods based on integrating the device that incorporates a small RF coil with the MRI for tracking and profiling the RF signal has been proposed[85].

Also, XMR intervention suites which integrate the MRI and X-ray modalities is another solution to fuse MR image with its soft tissue contrast feature with X-ray imaging to guide and intervention[122]. These intervention rooms allow co-registration between the two imaging modalities and 3D/2D image registration for image-guided interventions by use of a robotic table for transferring the patient between the two imaging modalities[123].

2.3.3 Occupational considerations for MRI-guided intervention

The isocenter of the MRI scanners that contains the field of view of the imaging is at the center of the bore. MRI scanners are can be categorized regarding the length of the tunnel in the two groups of long and short bore scanners. The first group has a bore length of about 1.7m (e.g. Magnetom Skyra, Siemens) and this length for the second group is about 1.25m (e.g. Magnetom Espree,

Siemens). The common size of the diameter of the closed bore MRI scanners is 0.6m or 0.7m. These conditions physically limit the interventionist to access the patient and it may lead to ergonomic injuries. Open Bore MRI scanner improve this drawback by providing more working space and freedom for the interventionist, but this type of scanner suffer from the lower SNR for imaging due to lower strength of the homogenous magnetic field for the imaging[124].

2.4 Robotic catheterization

The role of vascular catheterization in medicine is expanding. Clinicians use the vascular catheterization for the different purposes of diagnosis and treatment of cardiac, and vascular diseases or in oncology. Cardiac diseases, coronary diseases and aneurysm in cerebral arteries which is a cause of the strokes are among the top causes of death due to a health issue. TACE is an efficient method of treatment of cancer with a solid tumor it is in use for the treatment of a specific type of liver cancer. There is a high potential of using TACE for treatment of cancer types with a solid tumor, and one obstacle is performing superselective catheterization of the blood vessels. All being said to clarify the role and impact of vascular catheterization in medicine. However, limitations including the high dependency on the experience of the practitioner and the adverse impact of the x-ray exposure are the obstacles of widespread use of less-invasive endovascular treatments for different cases. Introducing the robotic methods to the field of vascular catheterization have been considered as a way for the improvement first by developing mechanisms of steering and second letting the interventionist to control the device in a safe workstation away from the X-ray imaging. Domains covered in the field of robotic catheterization includes the development of steerable catheters and the mechanisms of actuation [70, 71, 73, 74, 125], systems for navigation and imaging[71], development of the tactile sensors to provide feedback from the mechanical forces[126-129], and development of platforms for simulation of the procedures for training to allow new physicians to develop endovascular skills[71, 130-132]. Decades of research and development in this field have resulted in the development of platforms for robotic catheterization.

Selective catheterization is possible by the use of catheters or guidewires with a specific curve or shape at its distal. Developing mechanisms for steering catheters to enable making the specific shape and bending at the tip is vastly investigated in the field of robotic catheterization. A common

approach is master/slave systems operated by a human, and common actuation mechanisms are tendon-driven catheters[133-135], magnetically navigable catheters[69, 73, 75, 125], smart-material actuated (SMA) catheters[136, 137] and hydraulically driven catheters[74]. Two latter ones have not received much acceptance. Smart-material actuated catheters use memory alloys that change their shapes based on different physical phenomena. For instance, these systems allow bending the tip by induction of heating or cooling of the integrated actuator. Electroactive polymers are another type of SMA used in developing steerable catheters. A reason that SMA catheters have not been accepted for commercial use is the mechanical complexity of the developed catheters. Hydraulically stiffening catheters provide bending in a plane by injection of liquid into the implanted segments along the distal part of the catheters.

Tendon-driven catheters operate by the aid of pull-wires. This type of continuum robots consists of a core (usually a nitinol wire) which deforms by putting wires (tendons) arrayed around it under tension to bend segments at distal of the catheter. These catheters usually integrate a handle that allows an operator to control the bending of the tip. Magnetically steerable catheters have magnetic implants to the distal section of the catheter. These implants interact with the external magnetic field, and this interaction bends or deflects the tip of the catheter. Magnetic navigation system requires a source of generation of the magnetic field and the common ways for generation of the magnetic field are the use of permanent magnets and electromagnets[138].

The theory of the Cosserat Rods is a theory in the nonlinear mechanics for the modeling of the large deformations of the elastic rods[139]. Modeling the deflection, twisting and the inflation of the rods that undergo large deformation have been developed based on this theory to model the catheters [138, 140-142]. Also, this theory has been used to model the shape of the catheters and the guidewire inside the vascular structures for simulation of the intervention [140, 143, 144]. Dynamic modeling of the device for the control of the position of the tip of the catheters actuated with the tendon-driven mechanisms and magnetic torque by use of this approach has been investigated as well for different applications including catheterization [134, 138, 141, 142].

2.4.1 Prominent robotic catheterization platforms

Regulatory organizations like the FDA have already given approval to some of the robotic platforms for the catheterization and clinicians have adopted these technologies. Two of the major

systems are Sensei and Magellan (Hansen Medical)[71, 74, 133]. These systems use catheters that actuated with a tendon-driven mechanism and controlled from a workstation. The Sensei robotic catheter system has been designed for EP. It has also been used for the treatment of endovascular diseases or cardiac mapping and ablation. Magellan system is designed for selective catheterization of the peripheral arteries and performance of this system is proven to be efficient for accessing peripheral arteries in comparison with manual catheterization. This system is being used in the clinic for endovascular interventions including aneurysm repair or grafting of occluded vessels. Sensei is equipped with a force sensor (Intellisense), while Magellan system currently lacks this feature.

Two other robotic catheterization systems that operate by the tendon driven mechanisms are Amigo (Catheter Precision), and CorPath (Corindus). Former allows steering of commercially available catheters with three degrees of freedom for cardiac mapping. These degrees of freedom are insertion/withdrawal, rotation, and deflection of the tip controlled by an operator from the workstation. Latter is designed for the navigation of the guidewire and balloon catheters for percutaneous coronary interventions[145, 146].

Magnetic actuation of an instrument has also been investigated for different medical applications including catheterization. The magnetic navigation systems require the specific facility to generate the required magnetic field. This approach is popular as it allows simplifying the instrument that operates within the body while the main source of the actuation that generates the external magnetic field is placed around the patient. These systems usually work by directional modulation of the magnetic field to manipulate the magnetic body/ies attached to the distal of the instrument. The most renowned magnetic navigation system for catheterization is Niobe (Stereotaxis) with +300 publications on its design and application including tens of clinical study and this system has been installed in more than 100 hospitals (shown in Figure 2.9) around the world (shown in Figure 2.9), per their website. This system incorporates two large permanent magnets positioned on the sides of the patient. An operator controls the orientation of the magnets to modulate the direction of a uniform magnetic field within the working zone of the system to manipulate the catheter tip. This system has been used in cardiac intervention for EP, cardiac mapping and ablation. The magnetic field that this system generates has the strength of 0.08T in a $20cm^3$ spherical working space. The operation with Niobe Stereotaxis is fluoroscopy guided. This system incorporates

OdysseyVision^{TM} system for the visualization of different signals and images for the operator and the medical team including the Electrocardiogram (ECG) signal, fluoroscopy image, ultrasound imaging and cardiac mapping (http://www.roboticep.com/clinical-data/).

Electromagnets (EM) have also been used in developing the magnetic navigation systems for the human-scale application. Aeon Phocus and CGCI (Magnetecs) are two of the prominent systems that have received CE approval. Both of the systems incorporate EMs spatially located around the patient to generate a mouldable magnetic field. The strength and gradient of the magnetic field that Aeon Phocus generates is 50mT and 250mT/m simultaneously. For CGCI, these values are 140 mT and 700mT/m. The primary application for these systems is cardiac ablation[73, 77].

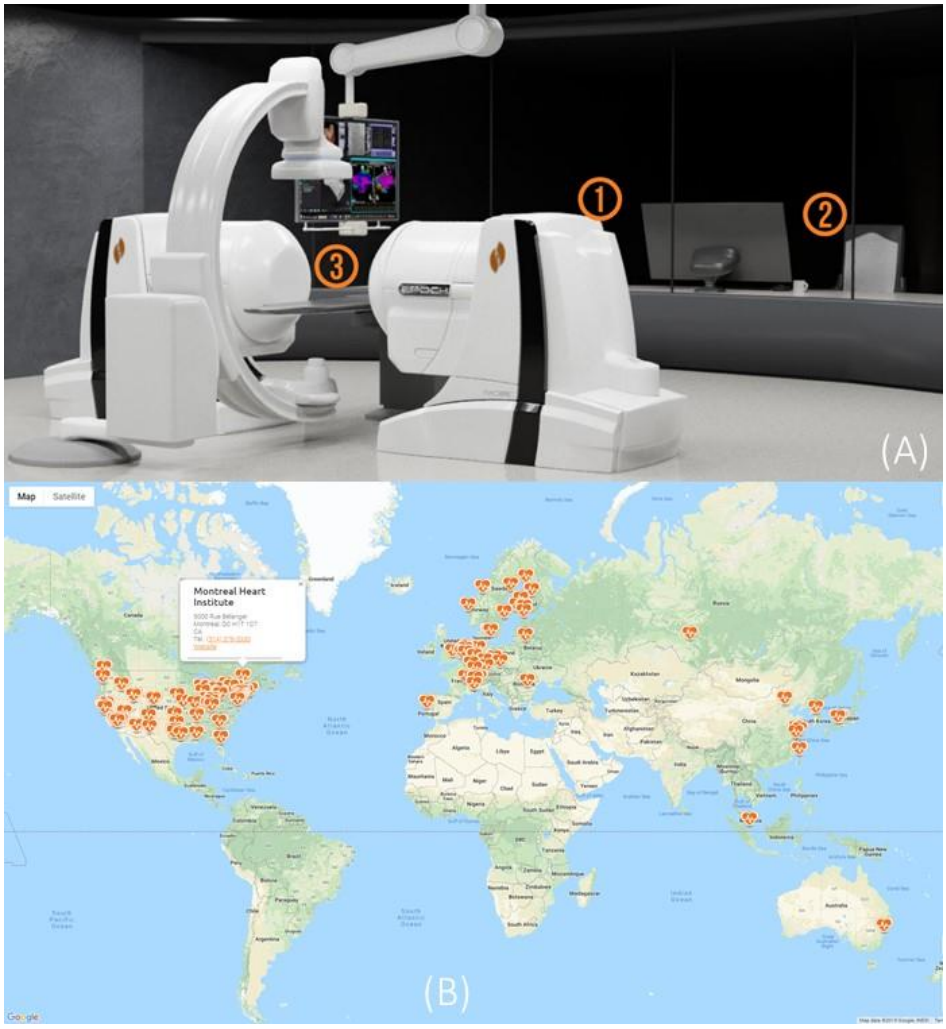

Figure 2.9 (A) Niobe Stereotaxis 1- remote magnetic navigation system 2- the workstation 3- the working zone of the catheterization (B) the location of the hospitals that have installed this system (source: http://www.roboticep.com/)

Reviewing the applications that robotic catheterization has provided shows that the concentration had been mostly on the performing cardiac interventions[4, 7, 74, 76]. Cardiac diseases are the leading cause of death and the main treatments include pharmaceuticals, implanted devices, and cardiac ablations[43]. Nearly one million cardiac ablation procedures are performed annually. While the state of the art of the robotic catheterization for cardiac intervention is at a level that can help patients in the clinic, improvement in the other domain (like interventional oncology) is still required.

2.4.2 The autonomy in medical robotic systems

Medical robotic is a fast-growing sector in the industry of medical devices. The robots in the medical domain serve us in different ways like performing minimally invasive surgery. One aspect of these systems is the level of autonomy provided in operating. Regarding this aspect, six levels are proposed to categorize the autonomy of medical robots. The first level (level 0) correspond to systems with no autonomy. Tele-operated robots, prosthetic devices, and surgical robot with motion scaling are examples of the systems in this category. The second level (level 1) is called robot assistance, and it includes the robotic systems that provide some mechanical guidance and assistance during a task while a human continuously controls the system. Next level or Level 2 is called Task Autonomy and is described as a robot can autonomously perform a specific task initiated by a human. The difference between this level of autonomy and the level one is that the operator has a discrete rather than continuous control of the system in task autonomy. Next level (Level 3) is conditional autonomy, which is when the robot can generate different task strategies, but a human has to select one for the execution. Next level (level 4) is high autonomy and is defined for the situation that the robot can make a medical decision under the supervision of a qualified doctor. Next level (level 5) is the case of full autonomy or a “robotic surgeon” which needs no human intervention to perform an entire surgery. Currently, a robotic surgeon is considered as a science fictional concept[13].

The systems developed for robotic catheterization that are currently in clinical use can be categorized as the level 0 or level 1 because in all the cases, an operator controls the execution of a procedure continuously from the dedicated workstation by use of the control consoles.

2.5 Fringe Field Navigation

A considerable specification of the magnetic navigation systems is the strength and the gradient of the magnetic field. The magnetic gradient force and the magnetic torques are depended on the magnetic moment of the magnetic body and either the strength of the magnetic field (for the torque) or the gradient of the magnetic field (for the force). Targeting the narrower vessels require minimizing the dimensions of the instrument including the volume of the tip. While the magnetic moment for a constant volume is limited to an upper bound due to the magnetic saturation phenomena, achieving a stronger magnetic actuation requires increasing the strength and the gradient of the external magnetic field. The current state of the art in magnetic navigation relies on the use of electromagnets and the permanent magnets to generate the required external magnetic field. These systems were introduced in the previous section. A limitation of these systems is the maximum strength and the gradient of the magnetic field generated by these systems. The strength of the magnetic field is not high enough to bring a soft magnetic body to its saturation state. As such, use of the neodymium permanent magnets to achieve stronger actuation is common. Another facet of miniaturization of the guidewire to target narrower vessels is the use of finer and so softer

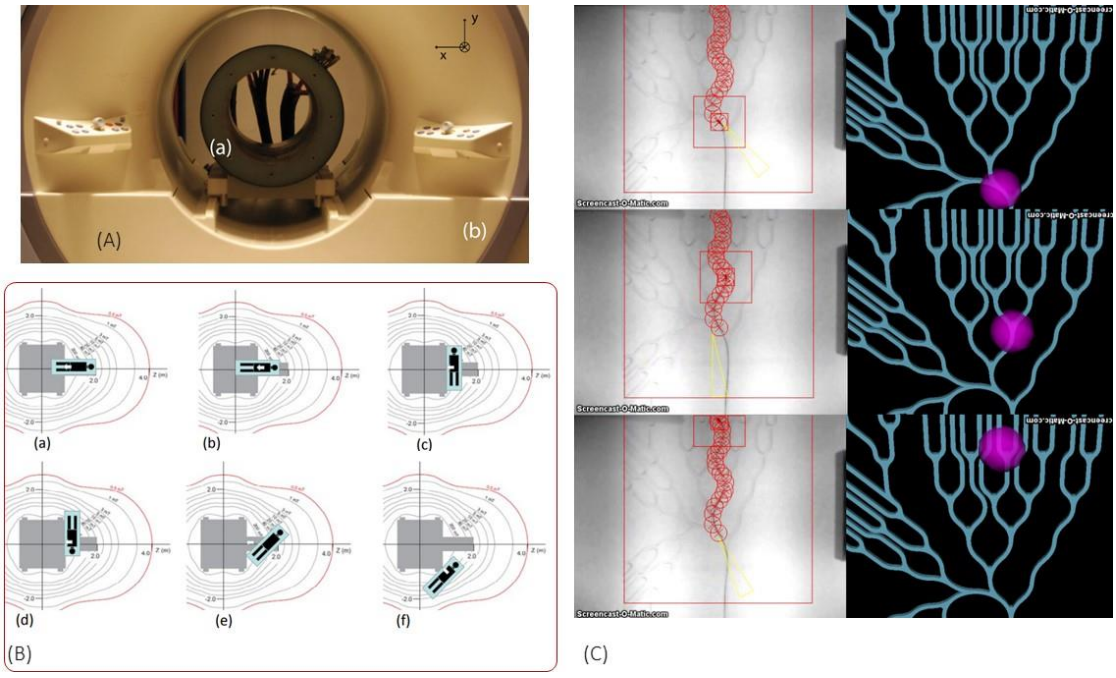

Figure 2.10 (A) the additional gradient coils in the MRI tunnel [65] (B) the introduced concept for exploiting directional steering with FFN and (C) result of initial *in vitro* FFN experiments [69]

tether which increases the difficulty of the steering and insertion of the guidewire device. When the distal of the tether is soft, crooking the guidewire during insertion can occur because of the intermittent contact forces between the vessel wall and the tether. A proposed solution is applying a pulling force on the tip of the guidewire and putting the distal under the tension, and the magnetic gradient force is proposed as the mechanism of actuation[69]. In previous research[69], this force was provided by the use of the additional gradient coils integrated inside the MRI bore. The additional coil generates up to 0.5T/m of the directional gradient, and it was used to steer a microguidewire with a spherical soft permanent magnet tip into the peripheral arteries of a rabbit model. Result of this work provided evidence that the proposed mechanism of actuation is useful for steering a microguidewire in the vascular system. One drawback of this method is that the additional gradient coil occupies space inside the MRI bore that it prevents the technology to scale up to the human size as shown in Figure 2.10. Also, the uniform magnetic field of the MRI scanners hinders exploiting the magnetic torque actuation. Also, another source of the magnetic field yet exists that features higher strength of the magnetic field as well as a much higher gradient of the magnetic field in comparison with the state of the art systems.

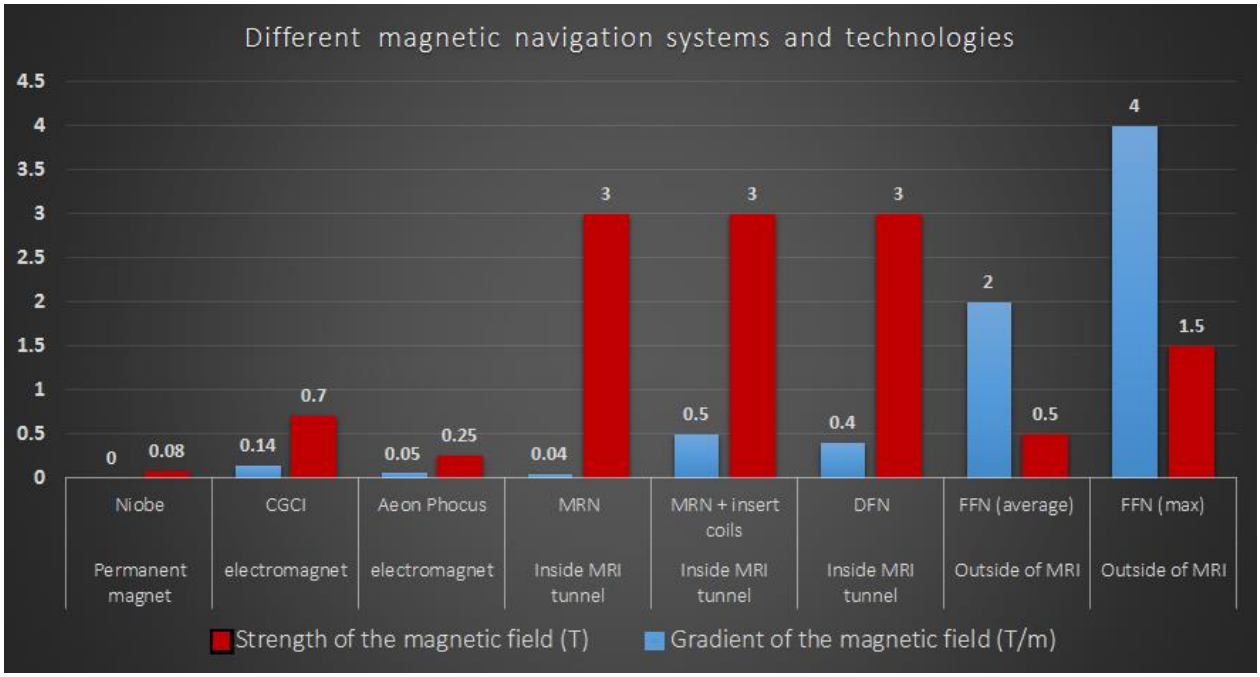

Figure 2.11 Comparison of FFN with other systems developed for magnetic navigation

As such, utilization of the fringe field of the clinical MRI scanner dubbed as Fringe Field Navigation was introduced aiming to exploit the much higher gradient of the magnetic field (up to 4 T/m) for the navigation of a tethered robot. The superconducting coils of the MRI system produce the fringe field. In comparison with the other systems developed for magnetic navigation, the strength and the gradient of the magnetic fringe field is an outstanding characteristic of FFN. Figure 2.11 illustrates a comparison of FFN with other systems regarding the strength of the magnetic field and its gradient. The fringe field being static, FFN requires six DOF robotic manipulation to provide the directional actuation within the static fringe field. Preliminary FFN experiments lacked the required facility for the navigation. Initial *in vitro* results of FFN is presented in Figure 2.10. Also, the map of the magnetic fringe field was not available, so the experiments were limited to only use the center axis of the MRI which has a known direction of the magnetic field[73].

Initial experiments showed the possibility of steering a microguidewire in 2D vascular models. However, navigation through the more sophisticated and 3D path requires the six DOF manipulation of the patient in the fringe field. Also, exploiting a large subspace of the fringe field in which the direction of the magnetic field changes by the location increases the extent of the directional actuation in FFN[73, 77].

2.6 Robotic patient positioning systems

A required facility for Fringe Field Navigation is the robotic patient positioning[77]. Robotic manipulators are introduced to the clinical application and use of robotic manipulators for patient positioning has recently emerged, and different companies are working in this field. Two of the

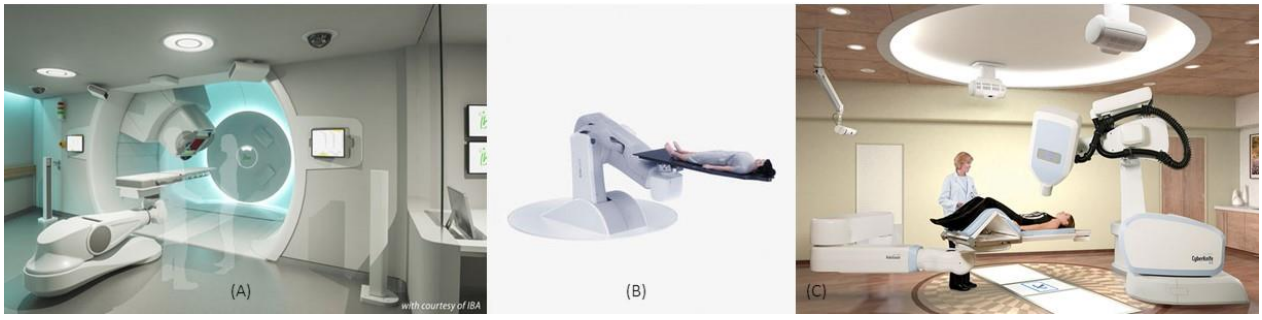

Figure 2.12 Use of robots for patient positioning (A) Leoni (www.leoni-healthcare.com) (B) Examove 6F (www.exacure.com) (C) Cyberknife (https://www.cyberknife.com)

examples of these systems are exacure (BEC Medical) and Orion (LEONI). Exacure comprises different systems of examove 6F (the robotic manipulator), Exacouch (the patient table), etc. Examove 7F is a 7 axes robot which is made based on an industrial robotic manipulator (KUKA) which features a high rated payload of 300Kg for 6 DOF positioning of the patient table. Orion is a six Axes robot and it has a higher payload capacity of 387 Kg for the positioning of the patient with the same degrees of freedom as Examove 6F. In addition, Orion system has recently received approval from the FDA and CE mark for patient positioning. Another system that has adopted the industrial robots for medical use is Cyber knife (Accuray Inc.) that uses the robotic manipulation for the positioning of the source of the radiation around the patient for the purpose of radiosurgery for the treatment of the cancerous tumors. A complementary product for operation with Cyber Knife is RoboCouch (Accuray) which is the robotic patient positioning module for this system. Figure 2.12 shows the systems introduced here for the purpose of robotic patient positioning.

CHAPTER 3 DEVELOPMENTS

3.1 General

Developments for implementing FFN (summarized in Appendix A) are presented in this chapter. The developments are categorized in the methodologies and the materials. Regarding the methodologies, the generation of the map of the magnetic field and the magnetic gradient force, planning the vascular trajectory of the blood vessels to derive the orientation and location of the vessels, a strategy for the navigation, a method for image guiding of the experiment, and the approach for the of the robot are the main parts. Main required materials for FFN are the custom guidewire for FFN, a system for controlling the advancement of the guidewire, and a robotic patient couch.

3.2 The venue for FFN

Basic facilities for the venue of FFN are the MRI scanner and the robotic manipulator for positioning a patient. The stray field of closed bore MRI scanners features higher strength and gradient of the magnetic field compared to open bore MRI scanners, and it makes them the proper choice for the source of actuation[124]. For the robot, adequate payload capacity is required to

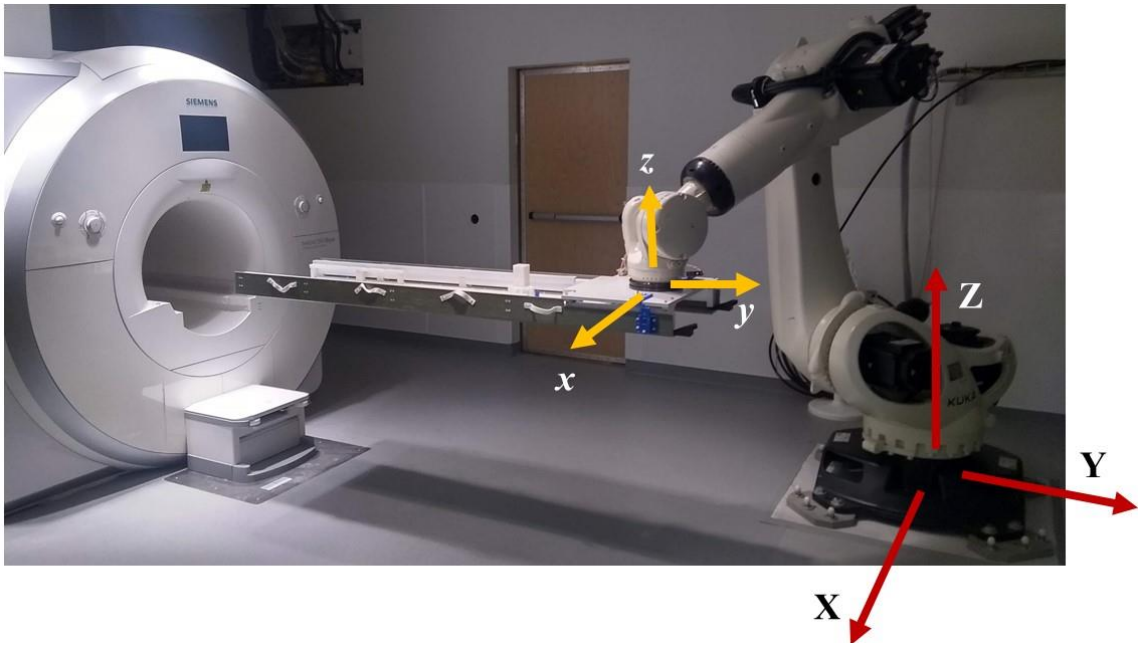

Figure 3.1 venue of FFN showing the MRI scanner, and the robotic patient positioning system

manipulate the patient. Our venue for FFN shown in Figure 3.1 includes an MRI scanner (Skyra 3T, Siemens) and a robotic manipulator (KR300R2500, KUKA) which is in the class of Quantum Ultra with the rated payload of 300Kg. The robot is driven with electromotors and includes magnetic parts, and the strength of the fringe field limits the distance that the robot can move close to the MRI scanner. The part that completes this composition is the patient table that is attached to the end effector of the robot and has to be MRI safe and MRI compatible. Therefore, while the robot operates in a safe distance from the MRI scanner, the patient table fills the distance to position the organ for FFN catheterization in the zone in the fringe field where the magnetic actuation is at the highest available for navigation. A detailed description of the table is presented later in this chapter. Integrating an imaging modality for guiding the FFN procedure is another requirement, and here a portable X-ray unit (Cios, Siemens) is used.

3.3 Methods

3.3.1 Map of the fringe field

A map of the strength and orientation of the magnetic fringe field is a basic requirement for FFN. The vector map of the magnetic field is required for generating the map of the magnetic gradient force applied on a magnetic body. A structural characteristic of the fringe field of MRI scanners is that the lines of the magnetic field are distributed axisymmetrically about the center axis of the MRI tunnel. This feature transforms the problem of mapping the fringe field from a complex 3d problem to a 2d problem that can be extended to the 3D space. The region of interest for FFN is at the front of the scanner. Inside the scanner, the magnetic field lines are uniform and directed toward the inside of the scanner and the gradient begins to decays from its highest at the entrance of the tunnel to zero at the isocenter of MRI tunnel. Fast decay of the strength of the magnetic field outside of the scanner leads to low strength and gradient of the field at a distance of 1 meter from the front face of the MRI[73]. It makes the zones after that not suitable for FFN. So, the working space of FFN in the fringe field is limited to a distance of 1 m from the front of the MRI and 1 meter radially from the center axis of the tunnel. The map of the magnetic field was produced for this sub-space.

Based on these conditions, mapping the magnetic field was done by sampling a radial plane of the fringe field. A 3-axes probe (F3A-3MH3A, Senis, Switzerland) with a measurement range of -2T

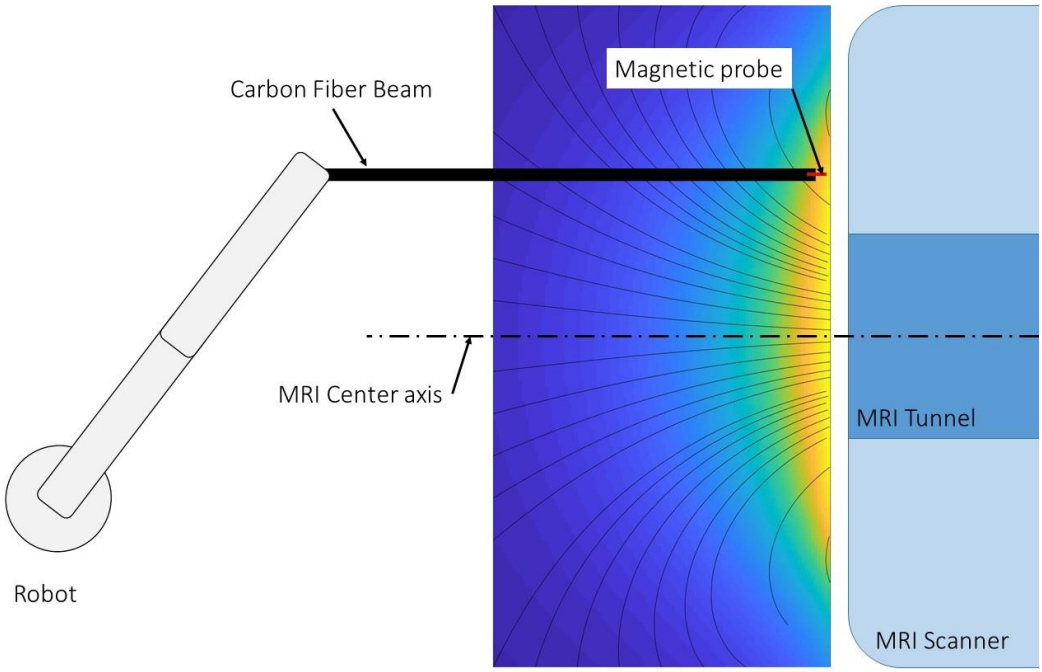

Figure 3.2 Schematic plot of the set-up for sampling the magnetic fringe field

to +2T with the accuracy of 0.1mT was used to measure the components of the magnetic field. It was mounted on a specific tool attached to the end effector of the robotic manipulator. This specific tool is a long beam of carbon fiber installed on a plate of aluminum attached to the robot end effector. The distance of the tip of the beam of carbon fiber to the robot end-effector is 1.9m. This long distance allows us to ignore any distortion induced in the magnetic field due to the magnetization of the magnetic parts of the robot as the robot was limited to operate in the zones where the strength of the magnetic field is below 0.02T.

The height of the center axis of the MRI was found by the measurement of the component of the magnetic field perpendicular to the radial plane of the fringe field parallel to the floor of the venue. Then, the axial and radial components of the fringe field were measured at different points in the radial plane. Samples were taken in the distance of up to 1.5m in the radial direction and 1.2m in the axial direction as well as inside the MRI tunnel. A total number of 800 samples was used for mapping the radial plane of the fringe field. Figure 3.2 shows the schematic set-up for mapping the fringe field.

Thin Plate Spline interpolation method[147, 148] was used to interpolate the strength of the magnetic field at any arbitrary point in the radial plan of the fringe field. Thin Plate Spline (TPS)

is a mathematical tool to approximate a radial basis function based on a finite set of scattered samples. More details of this method are presented in Appendix B. Map of a radial plane of the fringe field of 3T Magnetom Skyra is presented in Figure 3.3. Three-dimensional map of the fringe field was produced from the radial map of the magnetic field.

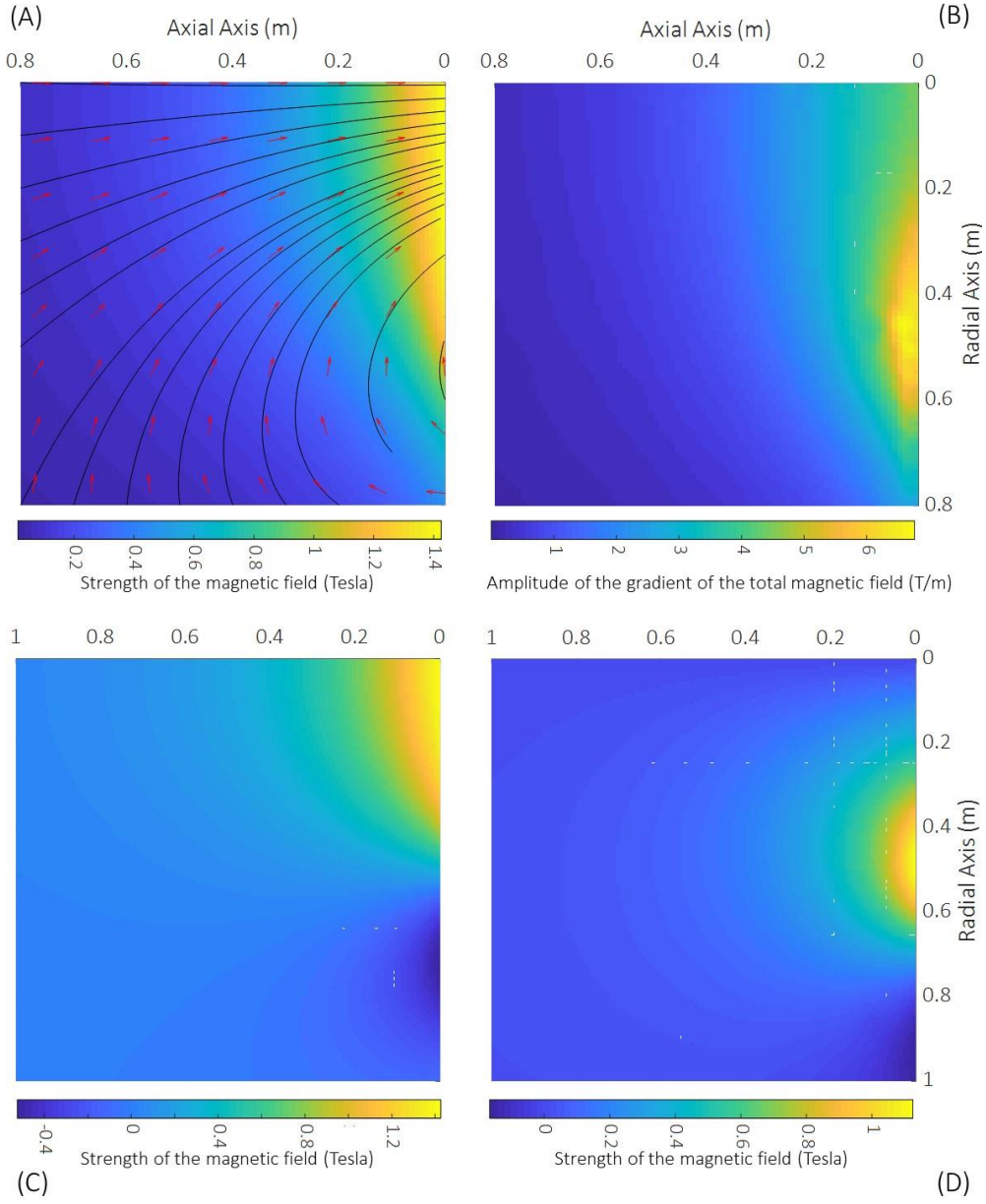

Figure 3.3 map of a radial plan of (A) total sum of the components of the fringe field of 3T Magnetom Skyra MRI scanner (B) amplitude of the gradient of the total magnetic field (C) radial component (D) axial component of the fringe field. In (A) red vectors show the vector field of the fringe field and the black lines are the lines of the magnetic field.

The basic idea of using the MRI fringe field for the navigation of microguidewire is that the magnetic field is static and constant. Therefore, any cause of distortion of the field must be avoided and distortion of the field at the working zone of the FFN has to be diminished. The patient table introduced in the beginning of this chapter is an important element in FFN that would operate inside the region of interest in the field. Fabricating this part from the non-magnetic (non-conductive) material is essential as it has been done here in this work and further details about the table and its compatibility with MR imaging is provided here.

3.3.2 Map of the magnetic gradient force

Once the map of the magnetic field is generated, it is possible to compute the magnetic force and torque applied on a magnetic dipole in an external magnetic field as a function of the orientation of the magnetic dipole[149]. For a permanent magnet, the magnetization is known and constant at any condition. Inside the external magnetic field, both magnetic actuation of the magnetic torque and magnetic gradient force apply on a dipole. The magnetic torque tries to align the magnetic dipole of the magnetic body with the external magnetic field. The formula for modeling the magnetic torque is presented in Eq 3.1.

$$\tau = \mu_0 v(M \times H) \qquad (3.1)$$

Which τ is the magnetic torque (N.m), $\mu_0 = 4\pi \times 10^{-7}\, T.m/A$ is the permeability of the free space, M (Amper/m) is the magnetization and H, (Amper/m) is the external magnetic field which can be expressed as applied magnetics flux density B (tesla) by the equation $B = \mu_0 H$.

The formula for calculation of the magnetic gradient force is expressed by Eq 3.2.

$$F = \mu_0 (M.\nabla)\mathrm{H} \qquad (3.2)$$

Which F (N) is the force and ∇ is the gradient operator. This formula can be written[150] in the form of Eq 3.3 when M is constant, and there is no electrical current within the region of space at which the magnetic dipole is placed. Details of the operations are presented in Appendix C.

$$F = \mu_0 v \begin{bmatrix} \frac{\partial}{\partial \mathrm{x}} H^T \\ \frac{\partial}{\partial \mathrm{y}} H^T \\ \frac{\partial}{\partial \mathrm{z}} H^T \end{bmatrix} M \qquad (3.3)$$

From this formula, it can be concluded that there is no limit for the magnetic gradient force. While for a constant volume of a magnetic body, M is either constant for a permanent magnet or soft magnetic material are limited to the magnetic saturation, increasing the magnetic gradient force is possible by increasing the gradient of the magnetic field. This is the place that the high gradient of the magnetic fringe field becomes useful in FFN.

As seen in Eq 3.3, the direction of the magnetic gradient force applied on a magnetic body is a function of its magnetic moment and the partial derivative of the components of the magnetic field (Jacobian). The Jacobian matrix of the fringe field is calculated by the TPS interpolation and differentiation of each component of the magnetic field along the different axes in 3D space. Then, the map of the direction of the magnetic gradient force was produced based on the assumption that the tip of the guidewire can rotate to align its magnetization direction with the external magnetic field. It requires that the resistance against bending the tip of the guidewire does not hinder this rotation. For a tethered robot that operates inside the vascular system, the stiffness of the tether, the contact forces with the vessel walls and blood flow speed can have some impacts on the orientation of the tip inside the blood vessels. In calculating the map of the magnetic gradient force, the direction of the tip of the guidewire is assumed to align with the external magnetic field. This assumption is made based on (1) guidewires with floppy distal will be used for FFN experiments to reduce resistance against bending and (2) FFN aims to use strong magnetic field (larger than 0.5T) which applies a high torque on the tip to rotate it and align its dipole direction with the direction of the external magnetic field.

The value of the magnetic moment of the tip is also required to calculate the magnetic gradient force. A permanent magnet is used at the tip of the guidewire in the FFN experiments. As the magnetization of the tip is constant in all the situations, calculations for the generation of the map of the magnetic gradient force was done for the unit of the volume and a constant magnetization value which is aligned with the external magnetic field. The direction of the force is the data that

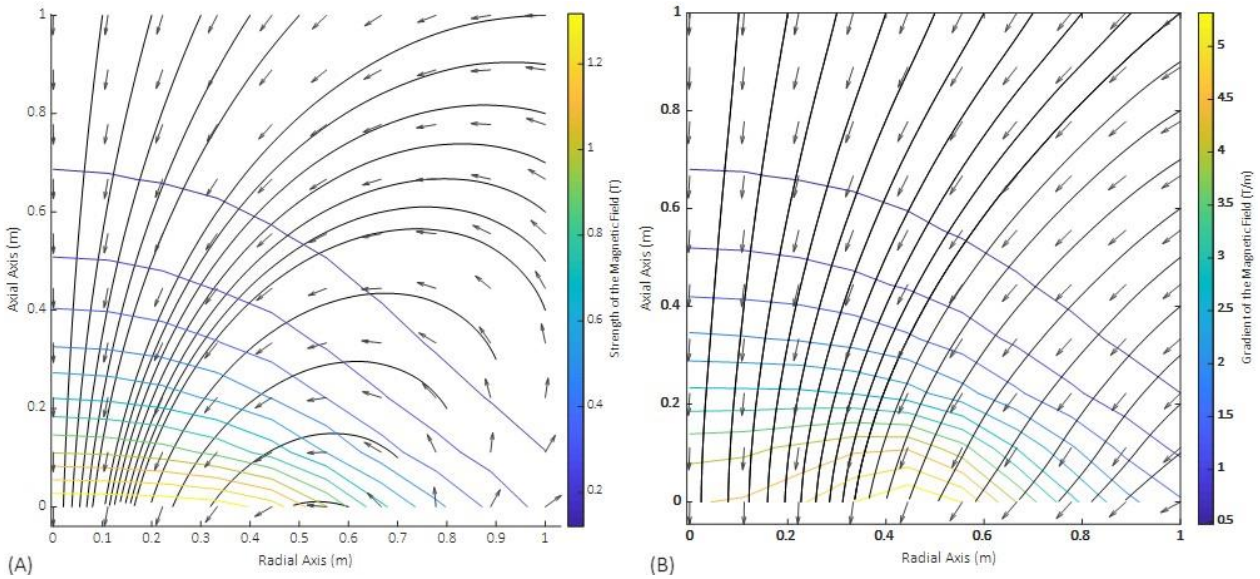

Figure 3.4 (A) vector field map of the fringe field and (B) the gradient force (vector field) and intensity of the gradient (heat map) the conditions described in 3.3.2.

is used in FFN, and the intensity of the force is qualitatively determined based on the strength of the magnetic field at different zones in the fringe field.

3.3.2.1 Field-Gradient-Deviation

The magnetic field is a vector field. The magnetic gradient force is a function of the directional gradient of the components of the magnetic field and the magnetic moment of a dipole inside an external magnetic field. The deviation between the direction of the magnetic field lines and the magnetic gradient force is inevitable, and rotation of the dipole at any point inside the external magnetic field changes the magnetic force. This deviation is called Field-Gradient-Deviation in this work, exists in the magnetic fringe field of MRI scanners. Figure 3.4 shows the direction of the two different maps of the magnetic field and the magnetic gradient calculated in the previous section, as well as the intensity of the gradient of the magnetic field[107] in (B). This deviation is smaller in front of the MRI bore and increases along the radial axis of the magnetic fringe field by moving away from the center axis of the MRI.

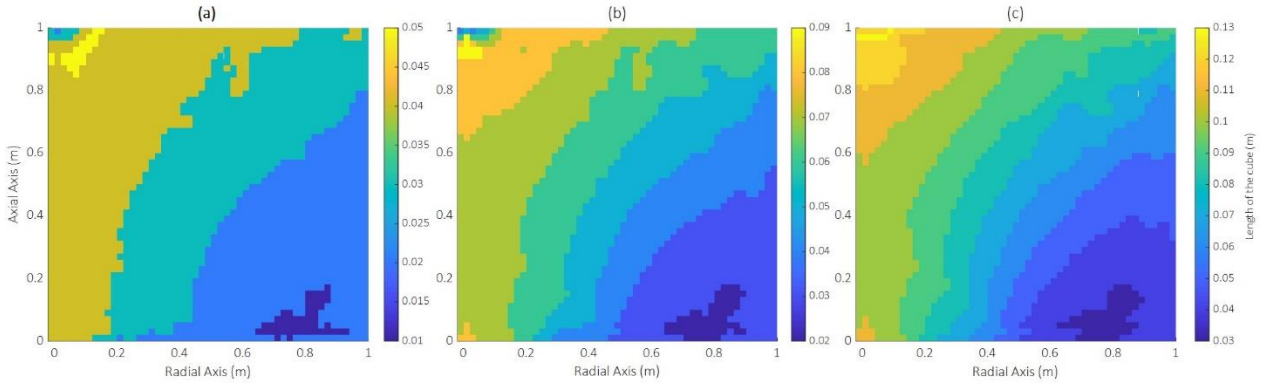

Figure 3.5 Size of a cubic sub-volume in the fringe field in which the deviation in the direction of the magnetic field between the center and the corners of the cube is less than (A) 5 (B) 10 and (C) 15 degrees.

3.3.3 Local uniformity in the fringe field

A feature of the fringe field is its local uniformity. The large size of the MRI scanner and slow variation of the direction of the magnetic field in distance cause this structural characteristic of the fringe field. This characteristic is also extendable to the direction of the magnetic gradient force in FFN. Such characteristics can be a measure to define the robustness for the FFN against the error in the positioning of the patient in the fringe field.

To investigate the local uniformity of the MRI fringe field, considered an expanding cube was considered with the center located at each discrete point of the map of the fringe field. Then the minimum size of the side of the cube for which the difference in the direction of the magnetic field at the corners of the cube from the point at the center of the cube is less than a threshold is calculated. The 3D map of the fringe field produced in the previous part was used for this purpose. A cubic sub-volume in the fringe field with its center at the points of the map was defined for each point. Size of the cube was expanding iteratively to find the length of the side of the cube for that the deviation between the points at the corner of the cube from the center is equal or larger than a threshold. TPS interpolation was used to approximate the components of the magnetic field at the points at the corners of the cubic subspace. The initial size of the side of the cube was chosen to be 1 cm, and it was iteratively expanding with steps of 1 cm to find the maximum size of the cube for a certain threshold of the deviation. Figure 3.5 shows the map of the maximum size of the cubes that determines the local uniformity of the fringe field for the thresholds of 5 degrees, 10

degrees and 15 degrees of deviation between the direction of the magnetic field at the center and the corners of the cube. It shows that local uniformity at the front of the MRI tunnel is large while by moving to the sides, the curvature of the lines of the magnetic field increases.

3.3.3.1 Comparison with Sheared Slab Model

Sheared Slab model (SS) is an approach to calculate the local curvature of the magnetic field lines[151]. This method is widely used in plasma physic. Here, this method is used to find the curvature and the radius of the lines of the magnetic fringe field of the MRI scanner. The local Cartesian coordinate system required for the SS model was defined for each point, as the MRI fringe field is axisymmetric, one axis, z, was considered parallel to field vector, second axis, x, perpendicular to field vector in the radial plane of the magnetic field and the third vector, y or azimuth, was perpendicular to the radial plane of the magnetic field as shown in the Figure 3.6. As

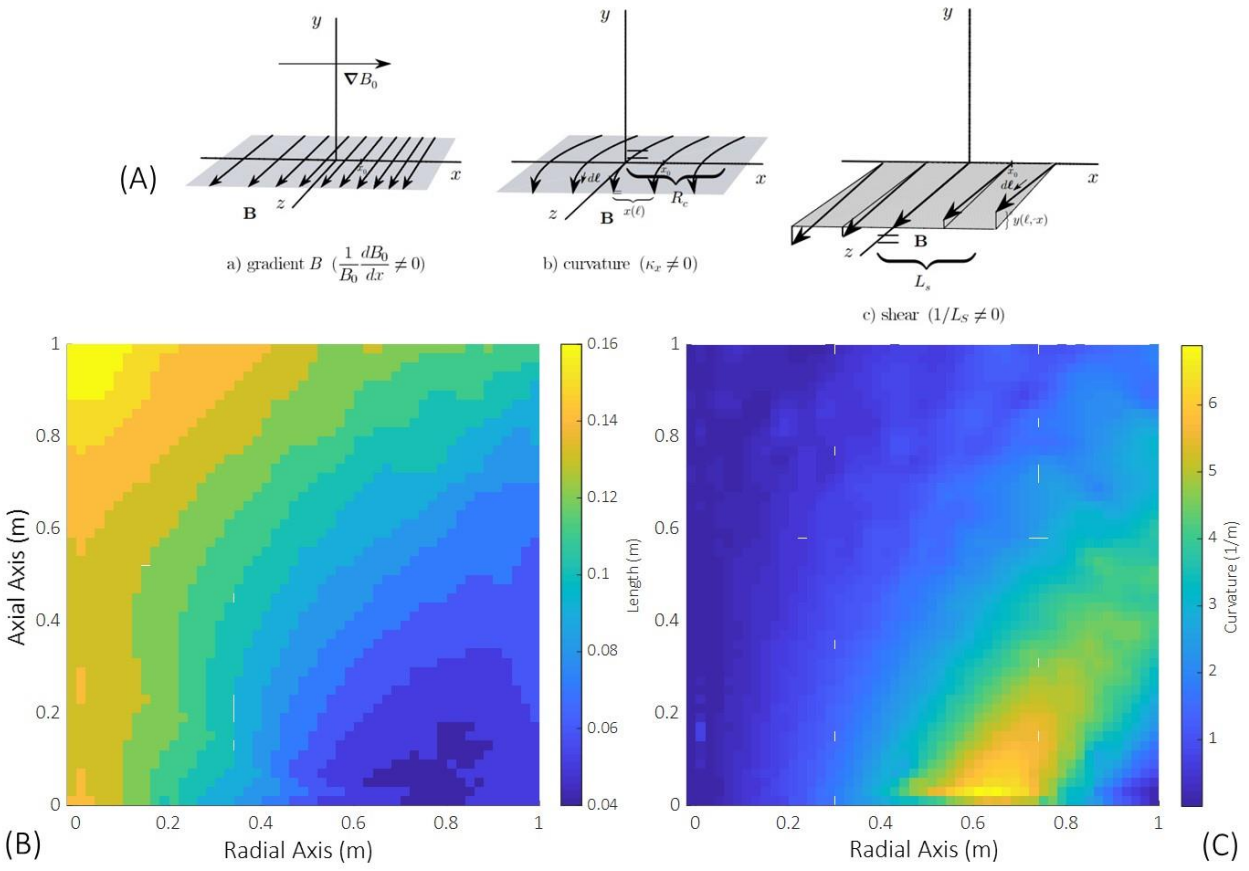

Figure 3.6 (A) local coordinate systems in sheared slab model [146] (B) size of the cube for 20 degrees deviation and (C) the curvature radius of the lines of the magnetic fringe field

the fringe field is axisymmetric, it can be expected that the least variation in the field happens in angular direction of the cylindrical coordinate system considered for the MRI fringe field. It is in accordance with the SS model where the azimuth has to be perpendicular to the field and in the direction with least change in the strength of the magnetic field. Eq 3.4 is proposed [151] to calculate the radius of the magnetic field lines:

$$R = \frac{B}{dB/dx} \qquad (3.4)$$

where R is the radius of the magnetic field, B is the strength of the magnetic field, and dB/dx is the gradient of the magnetic field in the direction x of the local coordinate system at each point of the map of the fringe field. The curvature of the magnetic field lines is inverse of the radius of the curves of the magnetic field. Figure 3.6 shows the map of the radius of the magnetic fringe field lines for a radial plan. Comparing with the results of defining a cubic subvolume of the magnetic field, it can be concluded that curvature of the field correlates to the size of the volume calculated based on the approach presented in this section as shown in Figure 3.6. Therefore, this data is useful to quantitatively determine the local uniformity of the magnetic field.

3.3.4 Vascular trajectory[152]

The vascular trajectory is required to have information on the location and the direction of the blood vessels. A method to generate vascular trajectory from the centerline data to present it in the

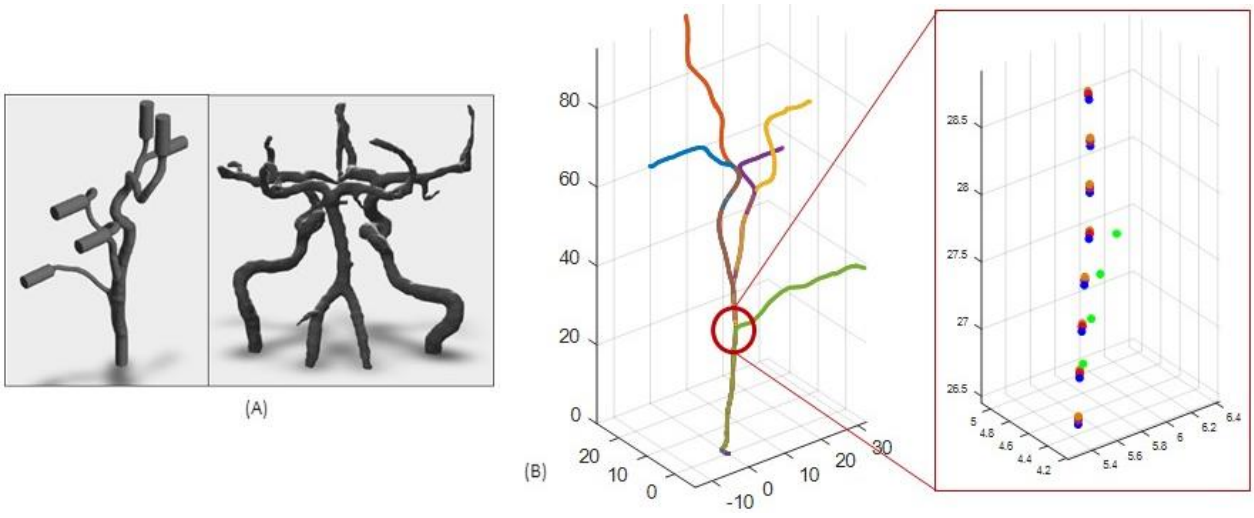

Figure 3.7 (A) models used as an example and (B) example of exceeding nodes in centerline data

form of a tree network is presented here. The method uses the vessel centerline data extracted from 3D angiography images. The software VMTK is used to extract the vessel centerline from the segmented model of the vessels. The output of this software is the three-dimensional information of the nodes that define the centerline model of the vessels. This output provides several chains of nodes. The chains start from a seed point selected by the user to different targets, again chosen by the user on the branches of the vascular models as shown in Figure 3.7. This data lacks information on the location of the bifurcation. So the goal is to unify the chains of the nodes for each of the routes and define a tree graph. Independent chains of different routes overlap on each other at the common sections of the vessels. So the first step is the elimination of the excessive nodes at the common section of the vessels. Following, an algorithm for the elimination of excessive nodes and then the trajectory planning algorithm is presented. Two different 3D vascular models of the 3D phantom used for *in vitro* experiments and the cerebral arteries presented in Figure 3.7 are used to clarify the steps of planning the trajectory. One of the examples is the model of the cerebral arteries and four different data set each consist of multiple vascular routes.

3.3.4.1 Elimination of extra nodes

At first, the consecutive distance of the nodes of the chains has to be evenly-spaced. The next step is the elimination of the nodes from the vessel centerline data that overlap on each other or are close together. Figure 3.7 shows the impact of excessive nodes. The criterion for this step is the mutual distance between each pair of the nodes. An iterative procedure is used for the elimination of the excessive nodes. For each pair of the nodes that their spatial distance is less than a threshold of THR1, one of them has to be eliminated in each iteration. As the nodes are spaced evenly, elimination of the nodes with a distance shorter than the average distance of the consecutive nodes of each chain (here called *d*) can lead to the removal of almost all the excessive nodes (exception is at the location of the bifurcations). The gradient of the number of the remained nodes calculate with Eq 3.5 at the end of each iteration is the stopping criteria of the iteration.

$$\nabla N = N_{n-1} - N_n \qquad (3.5)$$

Where *N* is the number of nodes remained after *n* iteration. The reason for using the gradient is that by increasing the size of a spatial neighborhood distance when the excessive nodes due to the overlapping of chains are eliminated, the number of the remained nodes converges to a constant

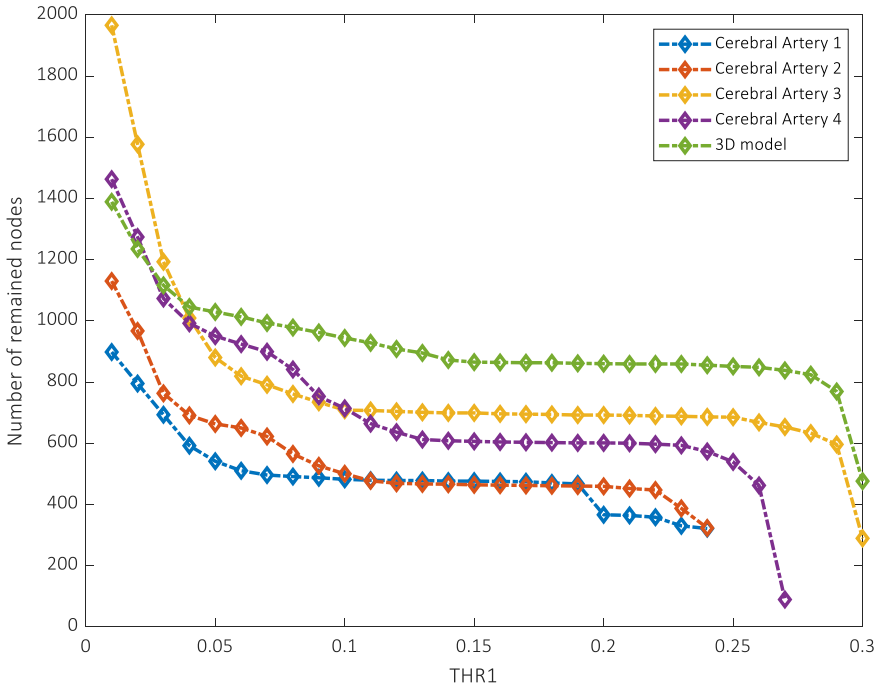

Figure 3.8 diagram of the remaining nodes from the centerline data through the progress of the step of elimination of the excessive nodes

value until the threshold reaches to the average distance of the consecutive nodes *d*. Figure 3.8 shows the number of the remained nodes by the progress of the iteration until it converges a constant value for the example models. The value of THR1 as the initial threshold of iteration was set to 0.01 mm, and the step of 0.01mm as increment step for THR1 value. Also, the nodes of the centerline data were spaced evenly with different values of *d* in the range of 0.25mm to 0.33mm. These values are randomly chosen to generalize the idea of this step. The criterion for stopping the iteration is$\nabla N = 0$. The set of the labeled nodes of S produced at the end in this step will be used in the next step as the input of finding the edges of the tree graph to define the set S in the form of a tree network.

3.3.4.2 Finding edges

The set S of the nodes generated from the centerline data in the previous section will be used in this part to generate the tree network for the vascular trajectory. From the number of the nodes, the number of the edges to define the vascular trajectory can be identified. Depending on the location of the nodes on the trajectory, the following specific conditions can be assigned to each node:

- Nodes corresponding to the beginnings and targets of the vascular path only require one edge to connect to the trajectory.
- Nodes along the vessel require two edges.
- Nodes corresponding to the bifurcations require at least three edges.

By having the spatial location of each labeled node of set S, the mutual distance of the nodes is calculable. For all the nodes, it can be expected the distance to the first closest node is approximately equal to *d* or less for the locations near the bifurcation. However, the distance of the second closest nodes for the nodes at the end of the branches is different from the rest of the nodes. It can be expected that the distance between the nodes at the end of the branches to the second closest node to them is about twice *d*. Figure 3.9 shows the first and second shortest distances of each node from the other nodes of set S for one of the vascular model examples. This condition applies to other examples as well. So, a subset E out of S consist of the nodes located at the end of the branches can be defined from the second longest distance data. By knowing the number of the

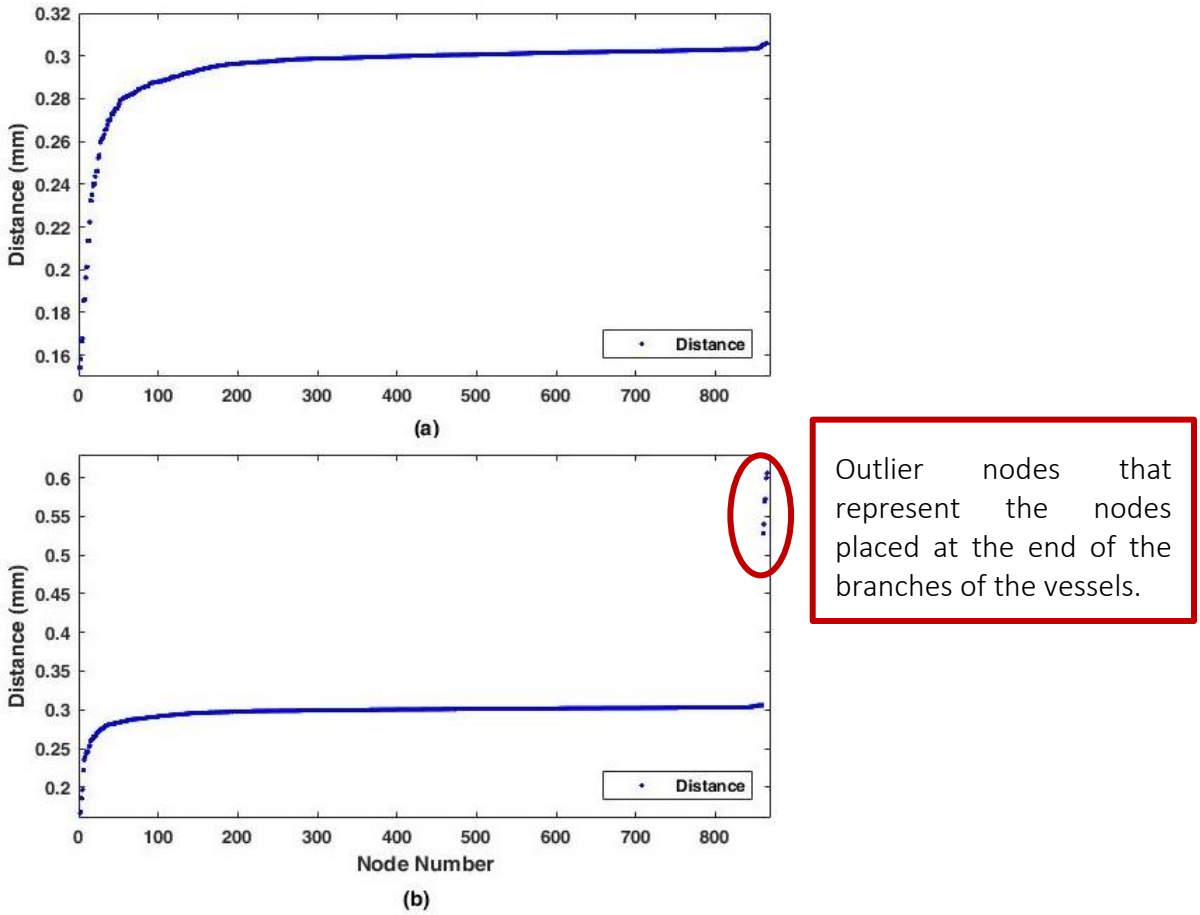

Figure 3.9 (A) first shortest distance and (B) the second shortest distance of each node from the rest of the members of set S for the 3D model of the phantom

targets, the nodes at the end of the vascular branches can be identified. The set E consist of the nodes that only require one edge to connect to the tree network and that node is the closest node to them.

Then the set C=S-E consists of all the nodes that require at least two edges. Majority of the nodes of the set C only require two edges to connect to the tree network. These nodes can be identified by the value of the third shortest distance between them to the rest of the nodes which has to be about twice d. If there are only two nodes in the neighborhood of them with a distance about *d*, the two edges of them can be identified. At the same time, the number of the remained edges for defining the tree of the network reduces as the total number of the identified edges increases. The nodes connected to the tree network at this step are those located along the trunk of the vessel and away from the bifurcations. At this step, different separate chains of the nodes are defined that the

nodes at their ends only have one edge. Among the nodes with only one edge, some belong to the set E. However, for those that are near the bifurcation and they only have got one edge, at least one more edge has to be identified. The set of the nodes that do not belong to the set E and only have one identified edge by the end of this step are called set G. For the nodes of set G, more than two nodes in S exist that their distance to the members of G is less than d.

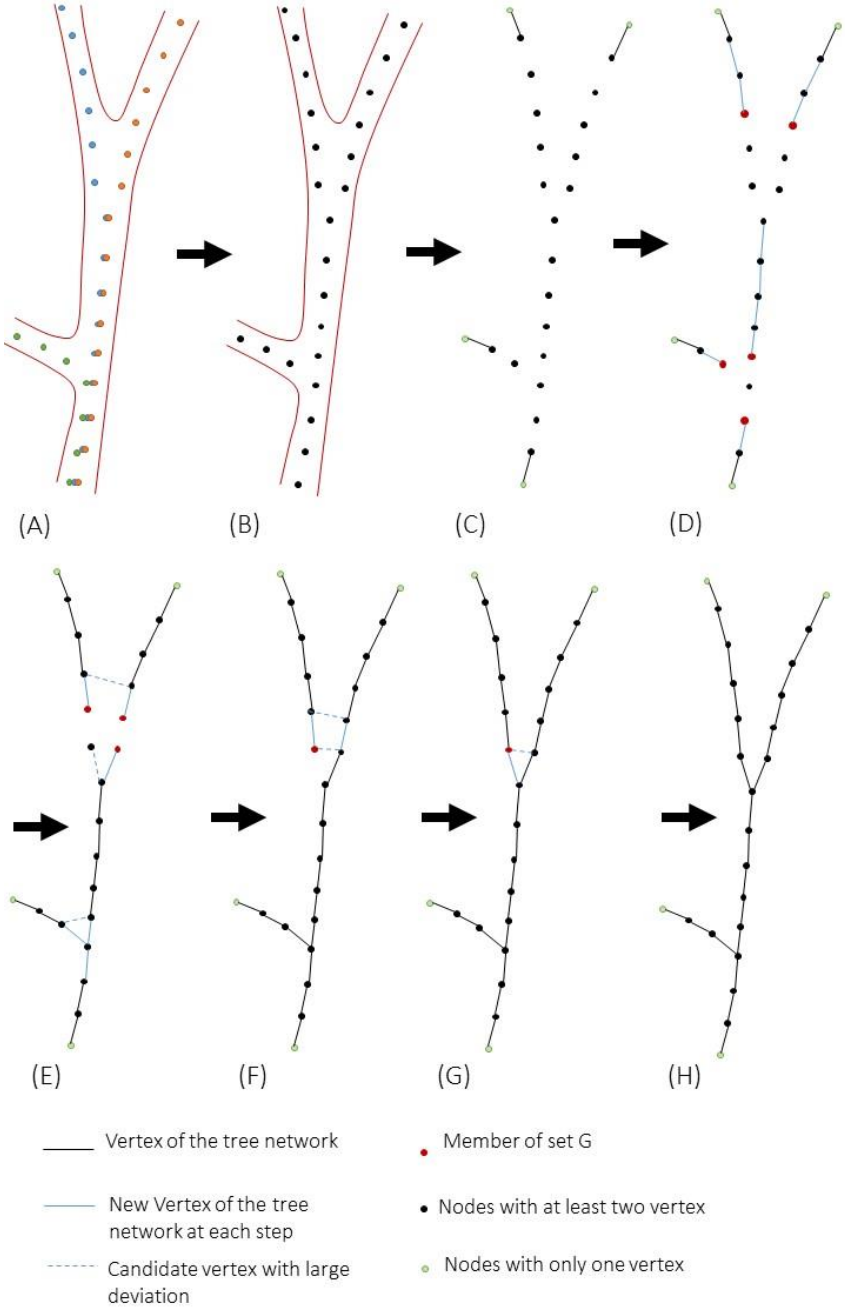

Figure 3.10 Schematic of the steps of planning the vascular trajectory from the centerline data

The next step is finding a second edge for each member of the set G. The second edge of these nodes is defined to connect the node of set G to one of the nodes that have a distance less than d. Among the candidate nodes from the set S, the second edge would be defined for the case that the deviation in the two edges of the node of set G is least to avoid having any kink in the vascular trajectory. The deviation can be identified from the spatial location of the nodes from the centerline data. After defining the second vertex of the members of the set G, a new set G can be defined among the members of C which only has one edge to connect to the graph. This step continues until the number of the vertex of the tree network reaches its expected number. Figure 3.10 shows the schematic detail of planning the vascular trajectory. In this figure, (A) is the input centerline data, and (B) is set S of the nodes after removing the excessive nodes, (C) demonstrate identification of the nodes at the end of the branches and their corresponding edge, (D) is the identification of the nodes that can connect to two other nodes based on the distance criterion. Then, (E) to (H) are the steps of defining the set G and identifying the new edges until completion of the network tree. This method and algorithm were implemented on the centerline data of different vascular models including the examples provided here and the vascular trajectory in the form of a tree network had been defined for all the cases. Result of this part is defining a tree graph of the centerline data.

3.3.5 Method of FFN

FFN uses the magnetic gradient force applied at the tip of a guidewire to steer and pull the tip in a desired direction. The basis of FFN is that by knowing the direction of the vessel at which the tip of the guidewire is placed, perform a robotic positioning to align the direction of the vessel with the direction of the magnetic gradient force in the fringe field. The answer for the navigation in the fringe field is not unique as any point in the map of the fringe field can be used for the navigation. However, factors like collision, robot reach, the strength of the magnetic actuation, the field-gradient-deviation, and pitch and roll rotation of the table limit the number of the answers.

3.3.5.1 Method of Navigation

Two different coordinate systems were considered for the FFN as shown in Figure 3.1. One fixed coordinate system for the intervention room to relate the position of the robot to the map of the

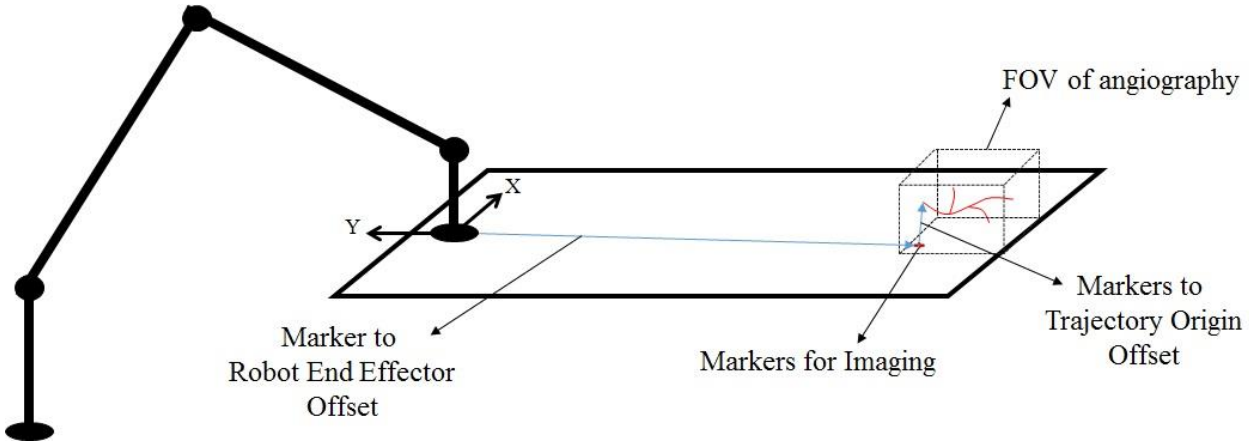

Figure 3.11 Schematic of defining the location and the orientation of the vascular trajectory in the coordinate system of the table

fringe field. The location and the geometrical shape of all the objects (e.g. MRI scanners, walls, floor) are defined in this coordinate system. The second coordinate system is attached to the patient table with its origin at the end effector of the robot. This coordinate system is considered to define the location and orientation of the blood vessels inside the body of a patient fixed to the table relative to the end effector and so in the coordinate system of the room.

Following an angiography, vascular reconstruction and the extraction of the centerline have to be performed. After evenly spacing the nodes of the centerline, the trajectory of the vessels can be defined that represents the centerlines in the form of a tree network. Then, information on the direction and the location of the blood vessels in the coordinate system of the table can be derived from the trajectory and location of fiducial markers from the angiography image as shown in Figure 3.11. By selecting the desired target and so the path on the trajectory, the method of FFN starts by discretizing the vascular routes on the trajectory to a set of consecutive segments and defining a sequence of FFN for each segment. The beginning of each segment is considered as the location that the tip of the guidewire is located at the beginning of the sequence of navigation. End of the segment which is the initial point of the next segment is defined based on the tortuosity and deviation in the direction of the vessel. Our criteria to define this deviation is the angle between

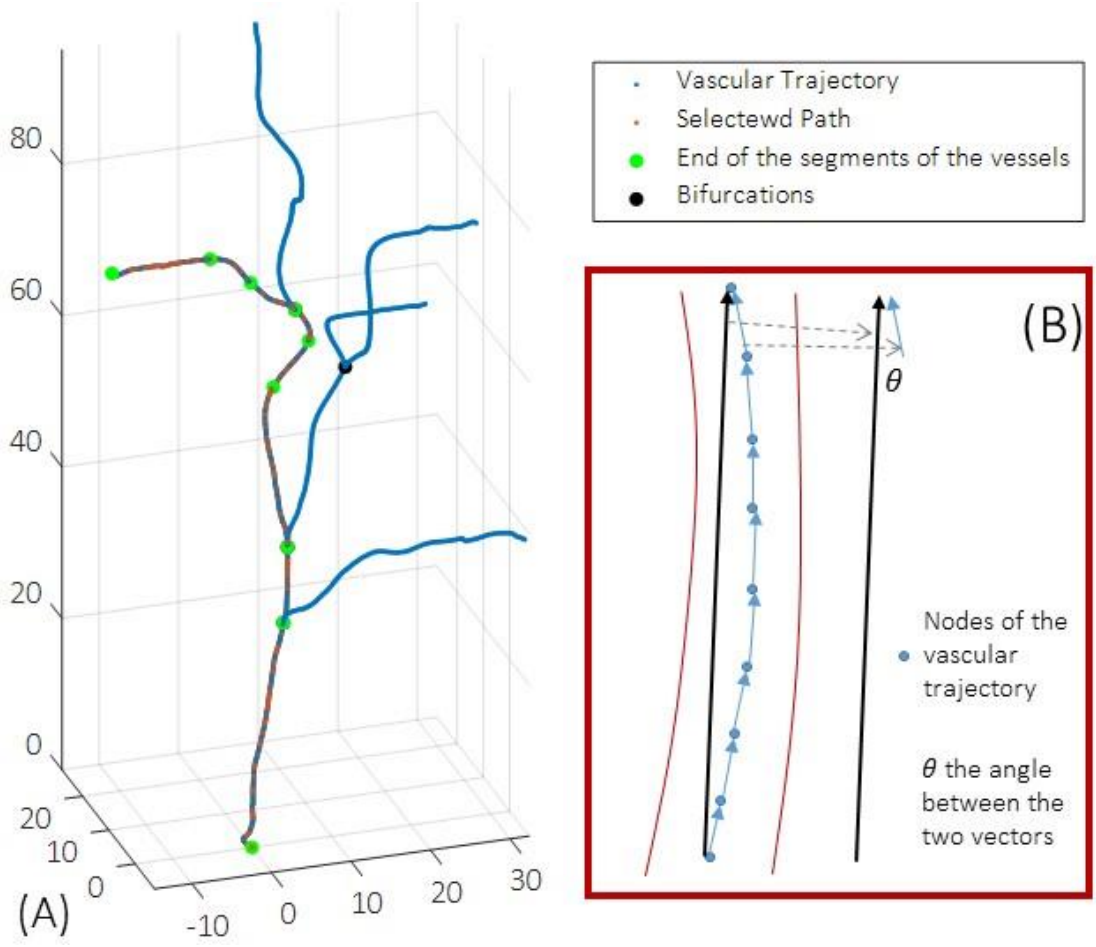

Figure 3.12 (A) Example of a segmented vascular path and (B) segmenting the trajectory

the vector connecting the initial and final node of the segment and the vector connecting the last two nodes of the segment. Also, bifurcations are considered as breakpoints to add a new segment. Figure X shows an example of the segmentation of the desired path in a vascular trajectory. Required parameters for calculating the sequences of FFN are location P_v of the beginning of the segment of the vessel and its direction D_v in the table coordinate system, and vector F_b that represents the direction of the magnetic gradient force at point P_b in the map of THE FRINGE FIELD in the room coordinate system. The sequence of navigation is defined by calculating a homogenous transformation (HT) that positions P_v at P_b while D_v is aligned with F_b. For a specific composition of P_v and D_v and considering the entire map of the magnetic gradient force, more than one HT that leads to a collision-free positioning can be calculated and one has to be selected. A procedure of FFN is the set of sequences positioning for each segment of the vascular path. For each segment of the vessel, the distance that the guidewire has to be fed can be calculated by the accumulation of the distance of the consecutive nodes of each segment.

3.3.5.2 Selection of Sequences for FFN

Many collision-free HTs can be calculated for a specific composition of P_v and D_v. The strategy to select the best sequence consist of two steps. First, the points of the map of the magnetic gradient force are ordered from the best points for FFN to the least appropriate points based on the two criteria of strength of the magnetic field and the field-gradient-deviation as shown in Figure 3.13. Step two is related to the calculation of the HTs for the FFN sequence. This step is done by iteratively calculating the HTs for the entire list of the points in the map of the magnetic gradient force to select the first collision-free HT that matches the criteria considered in each iteration. Through the progress of the iterations, the criteria to select the best answer becomes less strict. The criteria are a composition of (1) the minimum admissible value for the strength of the magnetic field, (2) the maximum admissible value for the field-gradient-deviation, and (3) maximum allowable angle for the roll and pitch rotation of the patient table. Steps of reducing the strictness

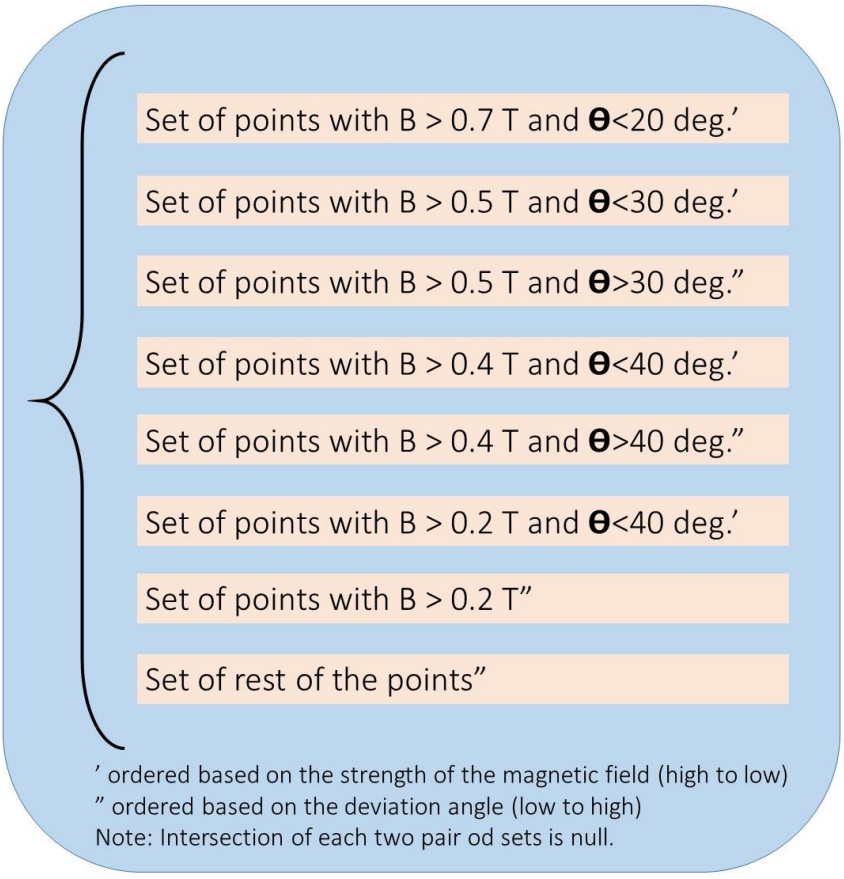

Figure 3.13 General order of the points in the maps of the fringe field

of the criteria for the strength of the magnetic field are 0.7T, 0.5T, 0.2T, the angle for field-gradient-deviation is 10 degrees, 20 degrees, 30 degrees and more, and for the angle of the spatial rotation of the table is 5 degrees, and 15 degrees.

3.3.5.3 Protocol of FFN

The protocol presented in this section are the steps followed in *in vitro* and *in vivo* experiments. Vascular access and placement of a catheter at a major blood vessel, immobilization of the patient for the entire procedure on the robotic table, and placement of the fiducial markers are considered as the steps prior to FFN procedure. Then, the patient table is transferred to the MRI for the 3D angiography imaging. After angiography, reconstruction of the vessels and extraction of the centerline to use for defining the vascular trajectory has to be done. Required variables in FFN (P_v and D_v) can be derived from the vascular trajectory and the reference markers that all are visualized by the imaging. From the trajectory, the target and so the vascular route is selected, and the route is segmented as described earlier. An FFN sequence, as well as the length for feeding the guidewire, are calculated for each segment. Every FFN experiment is performed by sequentially positioning the patient table based on the selected HT for each segment of the vascular route and feeding the guidewire for the calculated length of the segment of the vessel. The step of the localization of the tip of the guidewire with X-ray is performed to correct the location of the tip by insertion or retrieval of the guidewire with the feeder system under the fluoroscopy. Placement of the tip of the magnetic microguidewire at the initial point of the vascular trajectory is done by registration of the trajectory on the X-ray image and using fluoroscopy.

3.3.6 Avoiding Collision

Avoiding collision is crucial for performing robotic positioning in FFN. The possibility to plan a task for navigation of the guidewire including the trajectory for patient positioning is valuable for the autonomy of the procedure. Collision in FFN can occur between the robotic table and MRI, walls and floor as well as the table with the robot arms. A set of conditions is established to predict the collisions and avoid them in planning a procedure of FFN. First, a subspace inside the full working space of the robot is defined to limit the working space of the robot as shown in Figure 3.14. This subspace is limited in the height from 0.3m to 1.7m from the floor, and radially, it is

limited to 1.1m of the robot z-axis to 0.15m less than the full extension of the robot at different heights. So, only the HTs and the positions that the robot end-effector is inside this space are admissible in FFN. The table itself was modeled as a box with the actual width and length of the table. The position of the table in the room relative to the MRI and other obstacles is identifiable from the Homogenous Transformations (HT) calculate in the step of planning an FFN sequence to predict and eliminate any sequence leading to a collision. The tunnel of the MRI was modeled with details of the slabs and the rails inside the bore and the approximate radius of the curve at its entrance. Also, a safety distance of 3cm was considered between the table and the MRI tunnel to avoid moving the patient table so close to the MRI. The slab for docking the MRI table to the scanner was also modeled as an obstacle. The collision between the table and the robot arms was predicted by defining a simple model of the position of the robot arms for each location of the end effector. From the orientation and the location of the end effector for each HT, the location of the center of the spherical joint of the robot is identifiable. So, the orientation of the axis 1 of the robot and its joint to axis two can be calculated. Then the joint between the two long arms of the robot can be calculated by triangulation and the length of each arm. Required information for this modeling is available in the datasheet of the robot. So, by having the maximum radius of each arm of the robot and the region in space that the table occupies (from the HTs), it is checked if a positioning may lead to a collision between the robot and the patient table. Another consideration is that the robot end effector never enters the zones in the fringe field where the strength of the magnetic field is over 0.02T. Examples of modeling different elements in the venue of FFN is presented in Figure 3.15.

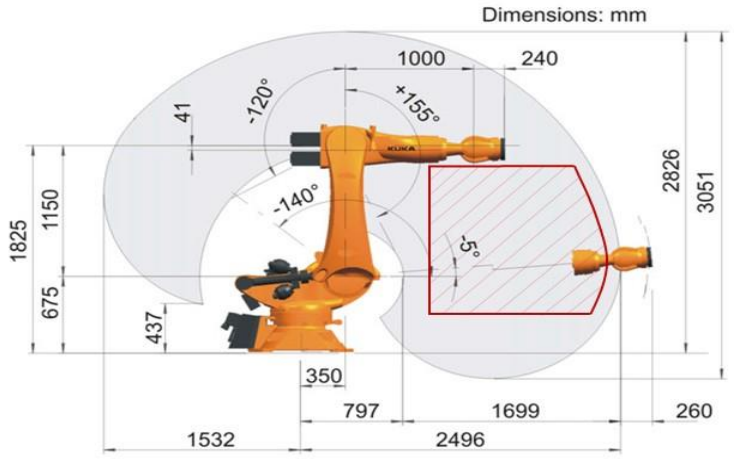

Figure 3.14 The limited working space of the robot for FFN experiments

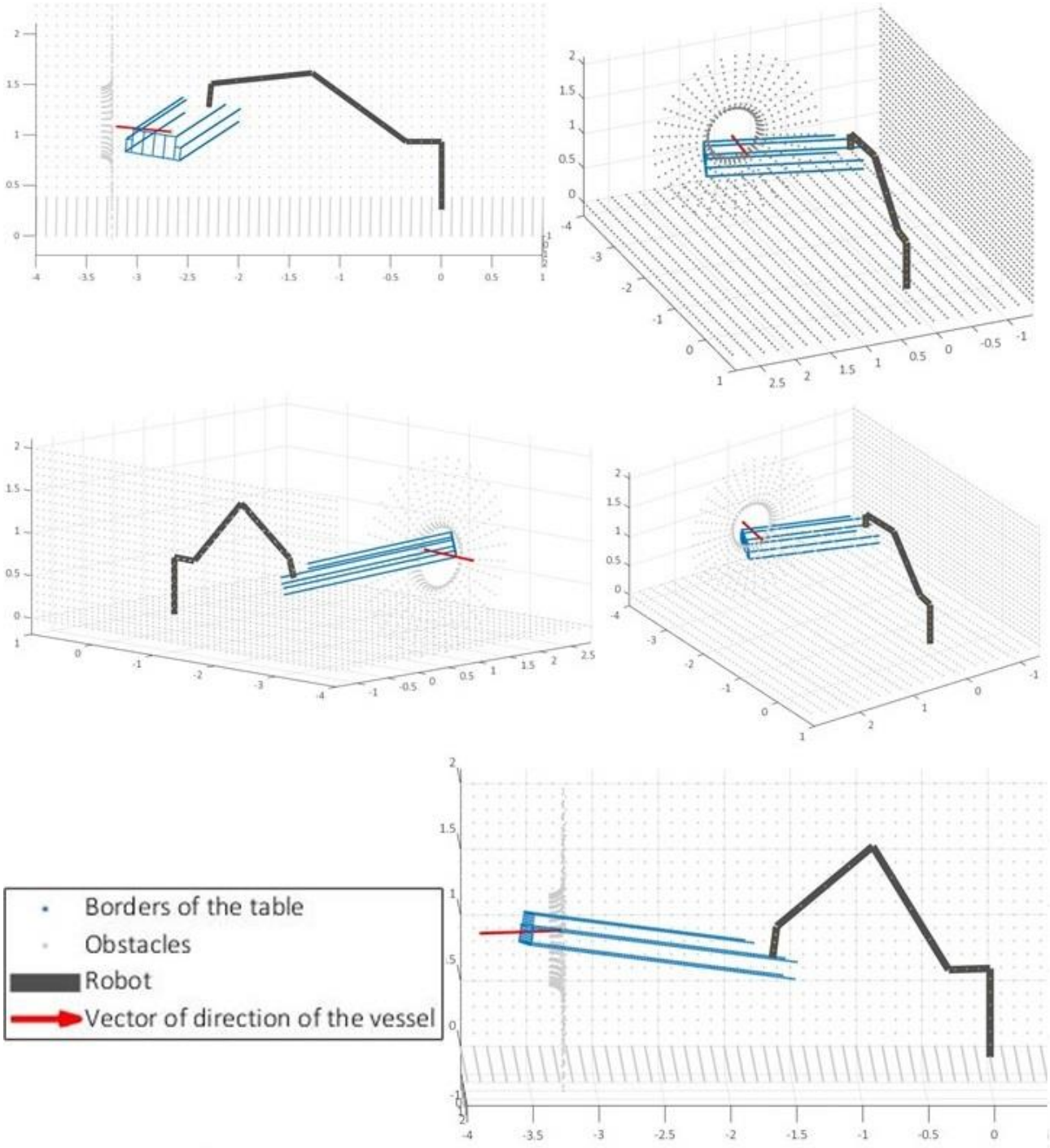

Figure 3.15 examples for the modeling of different elements inside the venue for a sequence of FFN including the wall, floor, the robotic manipulator, and the table and MRI front face for the prediction of collision

3.3.7 Motion Planning Strategy for Robotic Patient Positioning

Working zone for FFN is a limited space in front of the MRI scanner. Different cases for the manipulation of the robotic table can be defined within this limited working space depending on the layout of the room, the relative location of the MRI and the robot, and the target for robotic positioning of the table for the sequence of FFN. For the cohort of the robotic positioning, a general location for the table was defined that all the positioning for the FFN sequences begins from that location and at the end of the sequence the robot moves the table back to that location. Here this position is called Main. Then, depending on the location of the positioning of the table from the HTs, the trajectory of the motion in the form of a sequential step-wise rotation and orthogonal translation of the robotic table is defined for the trajectory of the patient positioning.

Based on the layout of the room, the working space in front of the MRI is divided into two separate zones illustrated in Figure 3.16. Also, all the movements of the patient begin from a general position here called HOME (the position shown in figure 3.1). For the zone I, the motion begins by three steps for the rotation of the table while the location of the end-effector is fixed at Main. Then the movements along X, Z, and then Y has to be performed. Considering Y as the last motion is to avoid collision with the MRI if the sequence of FFN requires to move the table inside the MRI tunnel. For the case that the robot has to move to Zone II, the steps of translation of the table are slightly different. For this case, the rotations at the beginning are planned similar to the case for Zone I. Then, the first step of the translation is a motion along Y that moves the table to a mid-location. No collision between the MRI and the table can occur at this mid-location for any orientation of the table and moving the table along the X and Z axes does not lead to colliding the robot with the table. Then motions along the X and Z are executed to move the robot to the location with x and z components of the HT for the FFN sequence. This movement is followed by another move along the Y axis to move the table to the final position for the sequence of FFN. Figure X shows the order of the steps of robotic positioning of the table for each sequence of FFN. The steps of returning the table to the Main is the reverse of the order of the steps of moving to the location of the HT of the FFN sequence. The Schematic of the steps of the robotic positioning of the table is shown in Figure 3.16. The motion for transporting the patient table to the location for X-ray imaging is a unique motion which its steps were defined manually. This motion is repeated whenever X-ray imaging is required.

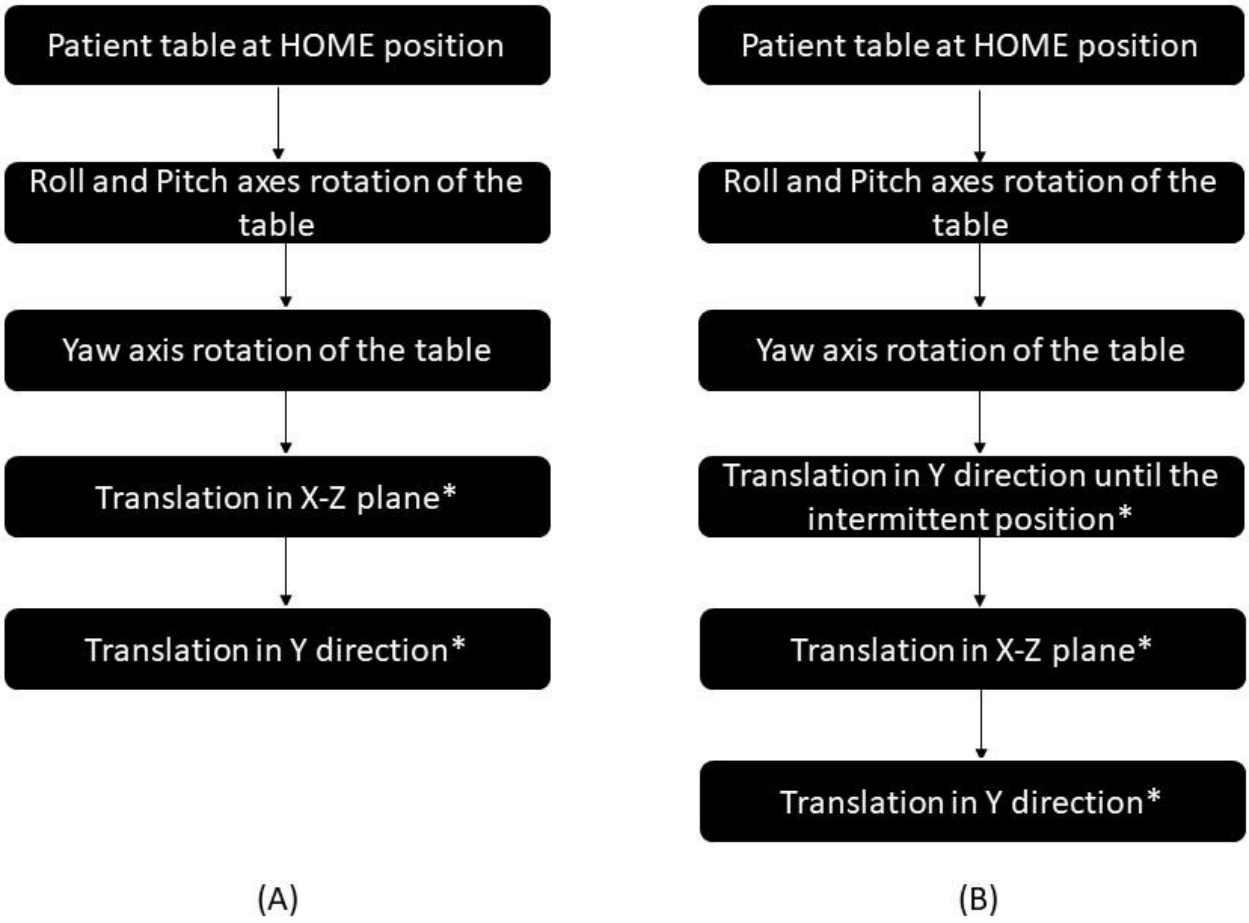

Figure 3.16 steps of the robotic positioning of the table. *X-Y-Z coordinate system is shown in this chapter (Figure 3-1). The steps of returning the patient table back to the HOME position is performed by reverse execution of the steps of moving the patient to the location of the sequence of FFN.

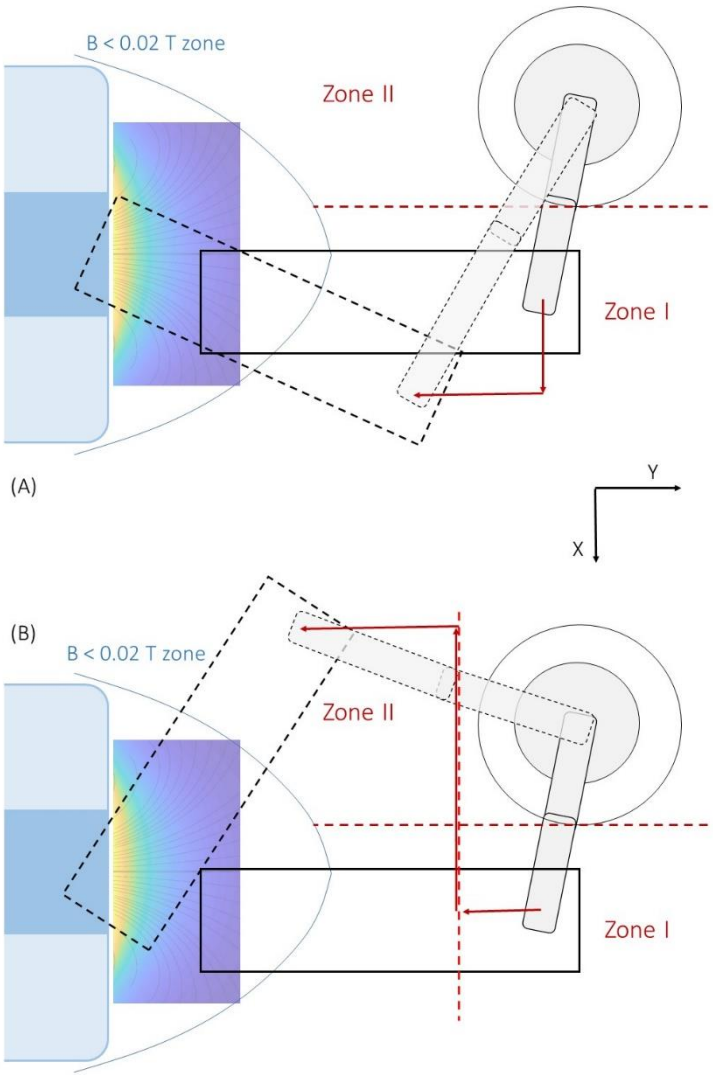

Figure 3.17 Defined zones for the motion planning for robotic patient positioning (A) zone I and (B) zone II (the dimensions and the distances are not exact)

3.3.8 Vascular registration

A geometrical approach for calibration of the x-ray image and registration of the vessel trajectory on x-ray images is developed. The x-ray console used in the experiments is a portable c-arm unite (Cios Alpha, Siemens). The distance between the source and the detector, the size of the detector, and the number of the pixels of the image were the parameters used from the c-arm. Three fiducial markers along a straight line with an uneven lateral distance between markers were used for the

calibration. Multimodal markers that are compatible with both magnetic resonance imaging and x-ray imaging are required for the registration and the calibration. Use of three markers was for adjustment of the coordinate system of the patient table with the x-ray image by rotating and flipping the x-ray image. The placement of the three markers is done in the way that the array of the markers are parallel to axis X of the table and the uneven lateral distance allows to define the direction of the axis.

One requirement of the vascular registration is the relative position of the vascular centerline from the markers. In this method, one of the three markers is considered as the reference. There is no constraint in choosing the reference marker in the method of the registration. Then the relative distance between the reference marker and the initial point of the vascular model can be measured by the voxel-wise distance of the two points in an MRI image and using the size of the voxel to determine the vector of the distance between the two points (Schematic in Appendix C).

Taking an x-ray image for the calibration has to be done by positioning the patient table in the way that the plane of the table and the detector of the x-ray are parallel. So, the circular markers attached on the surface of the table are expected to be seen as a circle in the x-ray image. Then, the location of circular markers can be identified by the use of the Hough transform[153]. By knowing the actual distance between the markers, their distance in the x-ray image, dimensional features of x-ray image and the C-arm and considering the center of the image as the center of the projection, the distance between the level of markers and detector can be calculated from the triangle proportionality theorem. By knowing the distance between the markers and the vascular trajectory, the spatial location of the nodes of the trajectory in the space of projection of x-ray from the source onto the detector can be identified. Then the pixel on the x-ray image corresponding to each node of centerline can be found. The schematic of the method of registration is shown in Figure 3.17.

Registration of the vessel trajectories on the x-ray images taken from a different view is essential for the localization of the tip of the guidewire. Blood vessels are distributed in 3D space, and the vessel may superpose on each other from certain points of view. So, looking at the vessels from a different angle is needed to distinguish between the vessels that overlap on each other in the primary registration. The method of the registration developed here is based on the relative location of the vessels in the space between the source and the detector of the c-arm – and so the space of the projection. Rotation of the patient who lays on the robotic table may lead to movement of the

body due to the gravitational force. Therefore, rotation of the c-arm is preferred for looking at the vessels from a different angle. By rotating the c-arm, the source, and the detector rotate to a new position. From the initial registration, the distance of the source and the detector of the x-ray from the patient table – all in the parallel plane – is known. After rotation of the C-arm around its center (which is known), the new position of the source and the detector and so the axis of the projection can be identified. Therefore, as the location of the vessels is supposed to be fixed, the relative Cartesian location of the vascular trajectory, and the source and the detector of the C-arm can be identified. As a result, the same method used for the registration of the vessels explained earlier can be performed for the registration of the vessels on x-ray images taken from the different views.

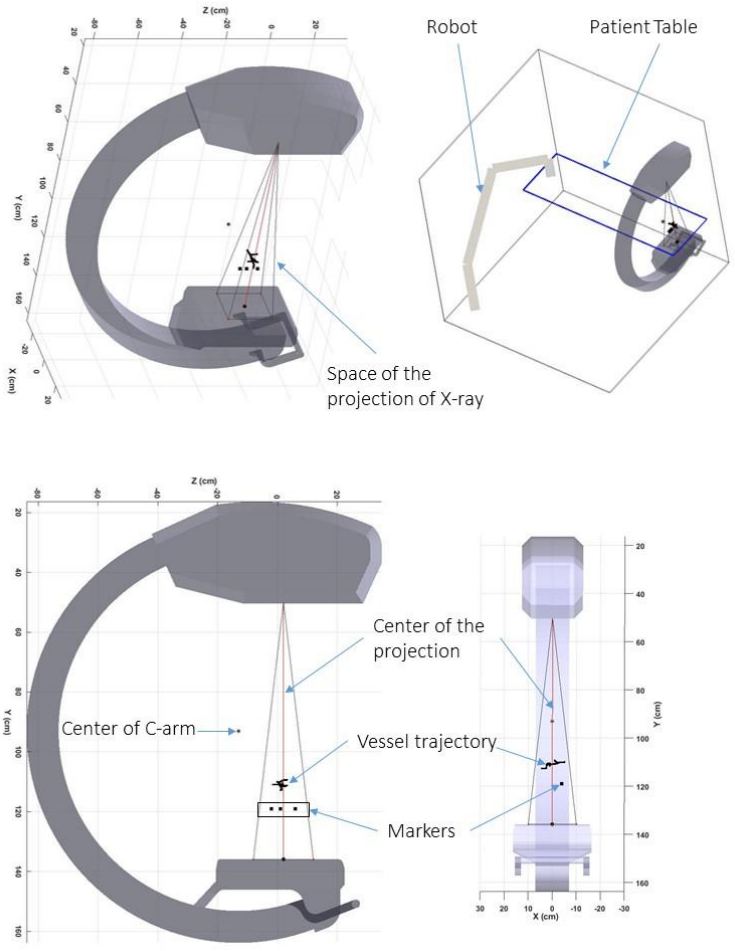

Figure 3.18 Schematic of the method of the registration by showing the relative position of different elements

However, it has to be noted that the rotation of the C-arm may lead to moving the vascular trajectory out of the field of view of the x-ray imaging.

As the method of the registration is based on the relative location of the trajectory of the vessels, and the c-arm, the relative translation of two parts can also be modeled for the registration. It is possible that the size of the detector is not large enough to encompass all the trajectory of the vessels. So, the translation of the patient table with the robotic manipulator is needed to move the region of the interest for the intervention inside the field of the view of the x-ray imaging. From the initial registration, the location of the vascular trajectory in the space between the source and the detector is known. The translation of the trajectory can be used to define the new Cartesian location of the vessels in the space of the projection of the c-arm and perform the registration for the same view from the c-arm but the new location of the vessels.

3.3.8.1 Correction of the movement

The movement of the patient on the table corrupts the accuracy of the registration, and it is inevitable during FFN. If the markers are placed on the skin of the patient, the movement changes the position of the body and so the location of the markers. If the markers are fixed to the table, the body motion – although leads to inaccurate registration – does not change the location of the

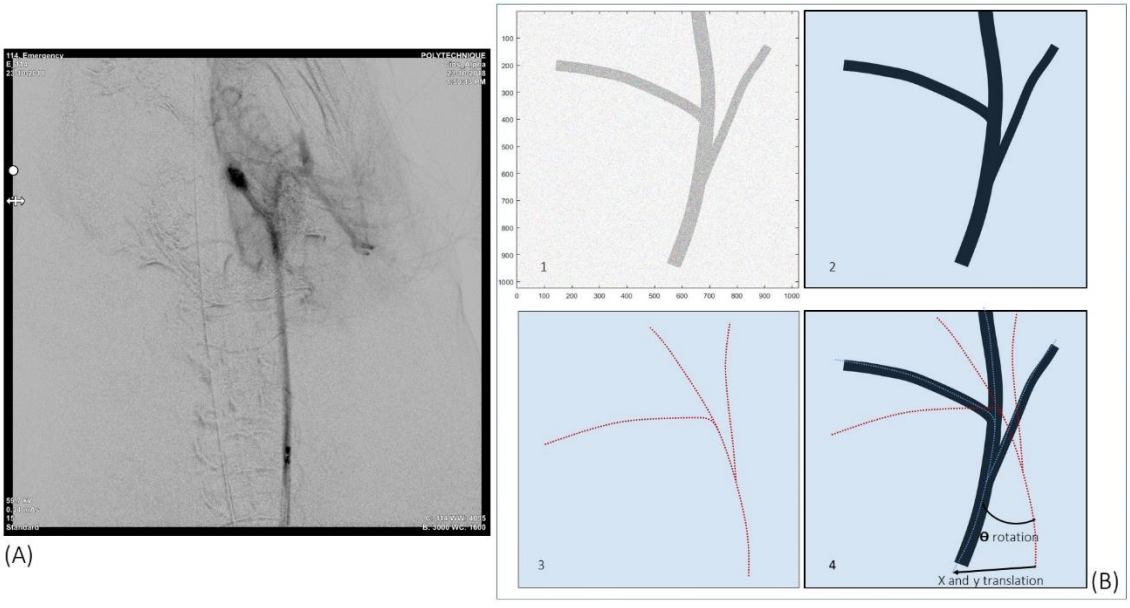

Figure 3.19 (A) a DSA image taken during *in vivo* experiments of this work and (B) schematic representation of the steps of correction for registration

markers. Under certain circumstances, the displacement of the vessel can be assumed to be a solid planar translation or rotation. For example inside the brain, if the neck does not turn and only the body translates on the table, the error in the vascular registration can be assumed to be a solid planar translation. So, in case of having a simple movement of the patient, it is possible to correct the error in the registration by finding the planar translation and rotation that has occurred. Here, a method is developed to fix for such an error.

The method of the correction of the registration requires digital subtracted angiography (DSA) images produced by the X-ray console. This image is produced by the injection of the contrast media (CM) through the blood vessels and visualize them under X-ray. Figure 3.18 shows an example of a DSA image. The first step of the correction is binarization of the DSA image to I_1 by applying a low pass Gaussian filter followed by histogram binarization. The result is a binary image with 1 for the pixels corresponding to the visualized vessels in the DSA image and 0 for the rest of the image as shown in Figure 3.18. Another binary image (I_2) with the same dimension of the x-ray image and 1 for the pixels of the trajectory and 0 for the background can be generated. This figure is similar to projecting the vascular trajectory on a plain image. Finding the composition of translation and rotation T of I_2 to get the highest overlap of non-zero pixels of I_1 and I_2 is the method to correct for the error in registration. So, the problem is finding the translation of XXXX in which x and y are translation components (in pixel) and θ is the rotation of the image (in radian) that maximizes the function in Eq 3.6.

$$F\left(I_{1\,i,j}\,, I_{2\,i,j}\,, T_{x,y,\theta}\right) = \sum_{i=1}^{n}\sum_{j=1}^{m} I_1(i,j).\, I_2^T(i,j) \qquad (3.6)$$

Where i, j are the indexes of the images I_1 and I_2 with the dimensions of m and n while I_2^T is the transformed image of I_2 with T transformation. The concept of the correction is presented in Figure 3.18, and figure 3.19 shows an example of correction of the image with this method. The DSA image in Figure 3.19 is produced by injection of CM in a tube, and then the image was used for testing the method.

In order to find the 3D planar transformation T, two approaches of Genetic algorithm (GA)[154] and Particle swarm optimization (PSO)[10] were used to solve the problem of minimizing the Eq 3.6. For both methods, the function from the library of Matlab was used for solving the problem.

PSO approach outperformed GA regarding the time and also finding the T, and it was used for the rest of the experiments and *in vivo* validation presented in chapter 5. Regarding the comparison in the performance of GA and PSO to find the answer, it was found that when the error is large, (for example 150 pixel difference on a 1024×1024 pixel image) the GA algorithm was unable to find the answer while no limit existed for PSO method. Also, PSO performed the task in a shorter time in comparison with GA. However, the better performance of PSO in comparison with GA had been demonstrated in different applications[155].

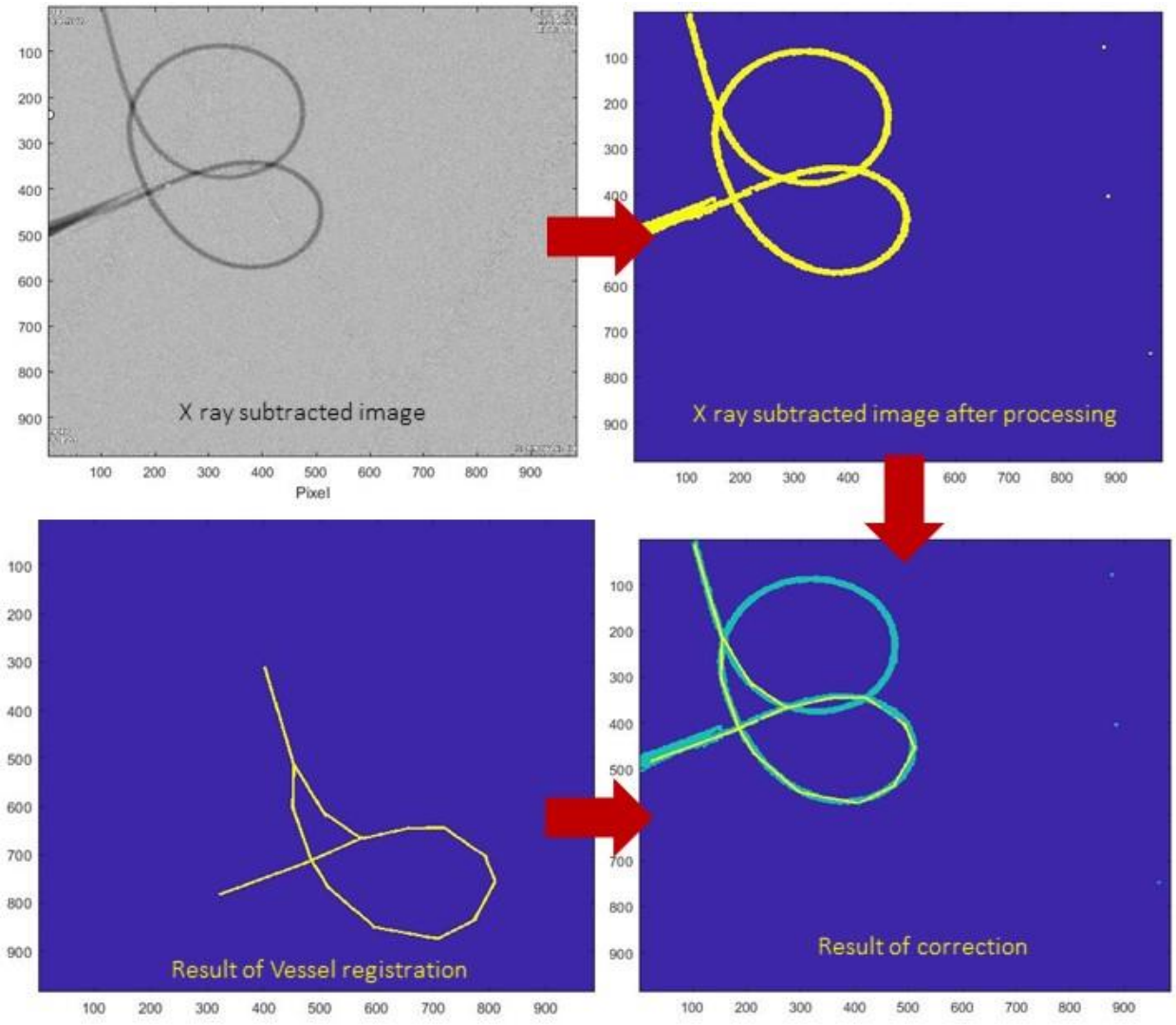

Figure 3.20 Example of the method for the correction of the error in the registration by use of DSA image

3.3.8.2 Limitations in the registration and causes of error

The method of vascular registration in this work is based on triangulation. While there are advanced methods of registration developed based on the multi-view projection, the method developed here was chosen based on the feasibility of implementation. One constraint in the registration was the occurrence of a collision between the table and either the source or detector of the table by turning the C-arm. A few constraints existed in choosing the method of registration. The C-arm used in this work is not iso centric. If the sample is not placed at the middle of the distance between the source and the detector, the ROI of registration moves out of the field of projection by turning the C-arm. Also, to visualize a larger part of the vessels under the x-ray, it is preferred to reduce the distance between the patient table and the detector. These factors lead to a limitation in the rotation of the c-arm while trying to avoid a collision. Using the method developed here enables registration of the vessels by using only one single image (top view of the table).

The accuracy of the registration can be disturbed due to multiple reasons. First, the table is a long cantilever that can bend and this bending is a cause of error which can be improved by increasing the rigidity of the table. Second, movement of the patient on the table throughout of a procedure of FFN which includes 6DOF positioning can disturb the accuracy of the registration. A way to fix it or diminish the error generated from this factor is to use appropriate immobilization of the patient on the table. Also, using the method of correcting the registration that is developed in this work can be used for evaluating the accuracy of the registration and also correcting for the error. While the immobilization fixes the exterior surface of the body, respiration can deform the internal organs especially in the abdomen and change the morphology of the vasculatures. Respiratory gating can be used for the cohort of the registration to consider either inspiration or expiration as the state of the patient for the accuracy of the registration. Gravity also can deform the internal organs as the FFN relies on 6 DOF positioning of the patient. However, as at the time of registration, it is considered to hold the patient in the same position of the angiography, it is assumed here that the deformation of the internal organs at the time of registration would not induce error.

3.4 Materials

3.4.1 Patient table

The patient table designed and fabricated for the experiments is composed of two parts. One part is an MRI safe cantilever structure that attaches to the end effector of the robot. This part is assembled by attaching two beams of carbon fiber to a plate of aluminum. The aluminum plate has a thickness of 0.5-inch and is attached to the end effector of the robot. Length of the beam from the point it is anchored to the aluminum plate is 1.6m while the distance between the end effector of the robot and the end of the table is 1.9m. Another part of the table is the patient overlay which has to be MRI compatible as it goes inside the MRI for the time of imaging. This part consists of an overlay of ABS plastic fixed on two L shaped fiberglass profiles by nylon fasteners. Length of the overlay is 1.6 m, and overall width of it is 56cm. Four blocks made of nylon was used on each side of the table, so the patient table can hang over the carbon-fiber beams by sliding the beams of carbon fiber inside the nylon blocks. The axial movement of the table relative the carbon fiber beams was constrained with latches fixed at the end of the table. The fiberglass profiles on the patient table are preloaded by placing hard rubber pieces so the payload of the patient would be distributed between both fiberglass and carbon fiber beams. Figure 3.20 shows the main elements of the table.

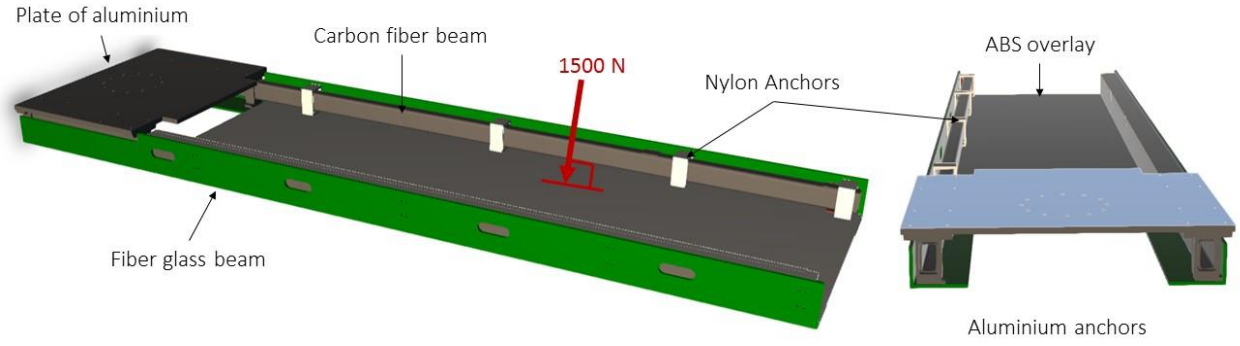

Figure 3.21 Main elements of the patient table for the robotic patient positioning

3.4.1.1 Design Consideration of the Table

The patient table designed for FFN is a cantilever structure that has to carry the load of a person lying on it. This table includes different parts that all of them experience mechanical stress when loaded. In the next paragraphs, the results of the finite element analysis (FEA) of each of the elements that are used in the table for a certain loading is presented. FEA simulation with Comsol 5.2 was performed to analyze the stress distribution and the deformation of each part under a typical load.

The loading defined for the simulation presented here can be in general described as a patient with the weight of 100Kg laying on the table, and the center of the mass of the patient is located at a distance of 1.5m from the point the table is fixed to the robot. The force analysis problem for the different elements of the table based on the loading and the fixed components is solved, and the specific load on each part is derived to use in the simulations. General description of the loading defined for the simulations is presented in figure 3.20.

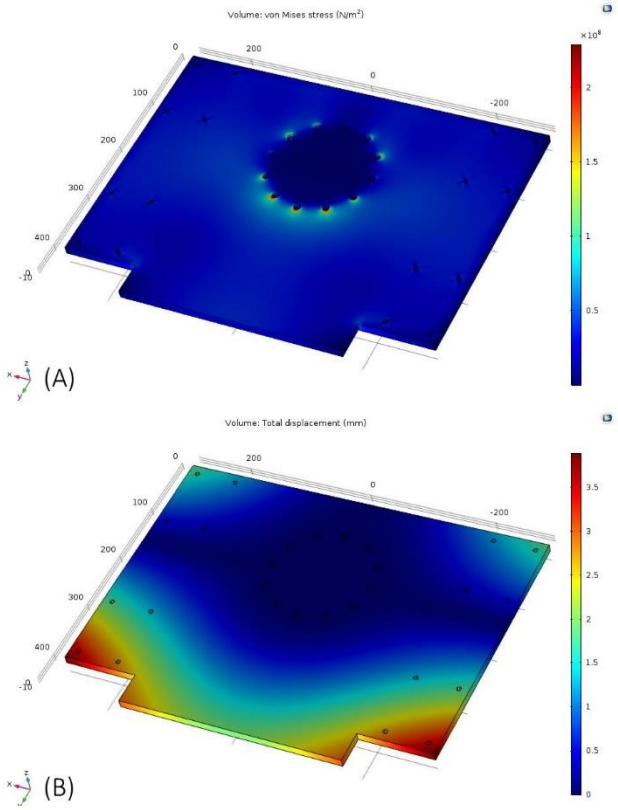

Figure 3.22 (A) the distribution of stress and (B) deformation

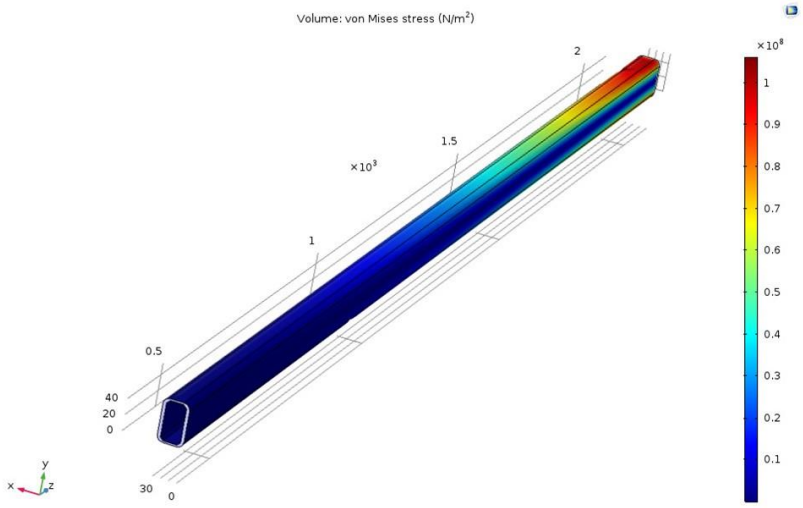

Figure 3.23 stress distribution in the carbon fiber beams under a uniform load of 750N

The first part that its FEA analysis is presented here is the aluminum plate attached to the end-effector of the robot. This part is a fixed end for the cantilever structure. The material used for this part is grade 6061 Aluminum with the tensile yield stress of 240 MPa. Results of FEA simulation of this part under the specific loading is shown in Figure 3.21. As shown, the critical zones of this part are the holes that are made to attach the plate to the end-effector of the robot. The total stress is near the yield strength of the material. While the loadings during our experiments were far less than the loading used for the simulation, this part can be restrengthened by increasing the thickness of the material at the zone which experiences higher stress. Also, the maximum displacement of the part that occurs near the corners of the plate is 3mm, a slight increase in the thickness of the plate at that location is recommended to reduce the deformations. As this part is near to the end-effector of the robot, a slight change of the mass of this part does not change the loading on the robot in order to handle its weight.

The second part discussed here is the carbon fiber beams. Two beams were used in the form of two cantilevers at the sides of the patient table. The beams are fixed to the aluminum plate, and the length of the beams is 1.7m from the point of the attachment to the plate. The cross-section of the beams is a rectangular tube. Results of the simulation for the stress distribution on the beam under a continuous load of 750N is presented in Figure 3.22. The ultimate tensile stress of the beams of

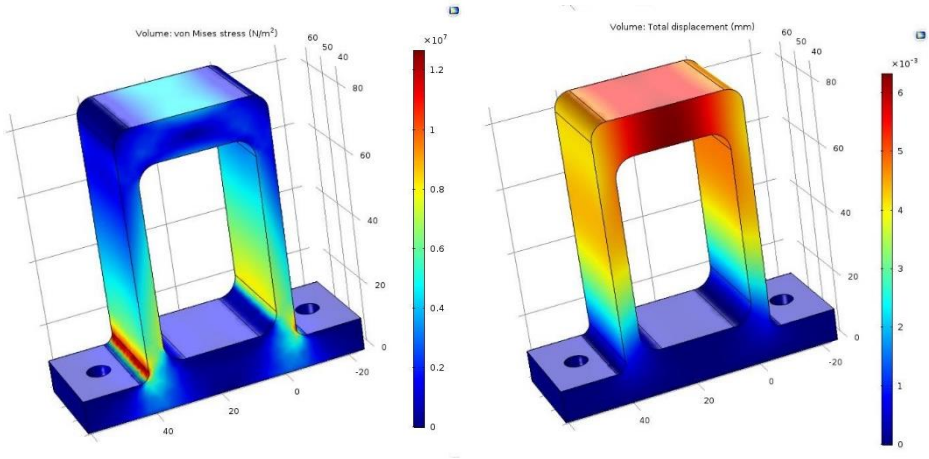

Figure 3.24 (A) the distribution of stress and (B) deformation

the carbon fiber is about 800MPa based on the website of different suppliers and it can be expected that the beams can tolerate the loading of the table. The average modulus's young of the beams based on the supplier was 142GPa, but the results of the simulation of the deflection of the beam were not validated with the actual deflection under different loading. The reason is that the carbon fiber beams are composite parts and fabricated by braiding of the fibers, the strength of the beams can vary based on the type and the direction of the loading and the method of the fabrication.

Beams of the carbon fiber were fixed to the plate of the aluminum with anchors. These anchors were also made of Al 6061 material and were fabricated with CNC machining. Figure 3.23 presents the results of FEA of this part under the loads described in the same figure. This part was fixed to the plate of the aluminum with non-magnetic stainless steel bolts of the gauge M6, and the bolts were also over-designed to carry the loads. The maximum stress for this part under the described loading was lower than the yield strength of the material, and the deformation was insignificant.

The MRI compatible part of the table which is an overlay detachable from the robot was described earlier. This part hangs on the beams of the carbon fiber with parts made of nylon plastic as shown in Figure 3.20. In total eight pieces of this part is used on the table, four on either side. These parts

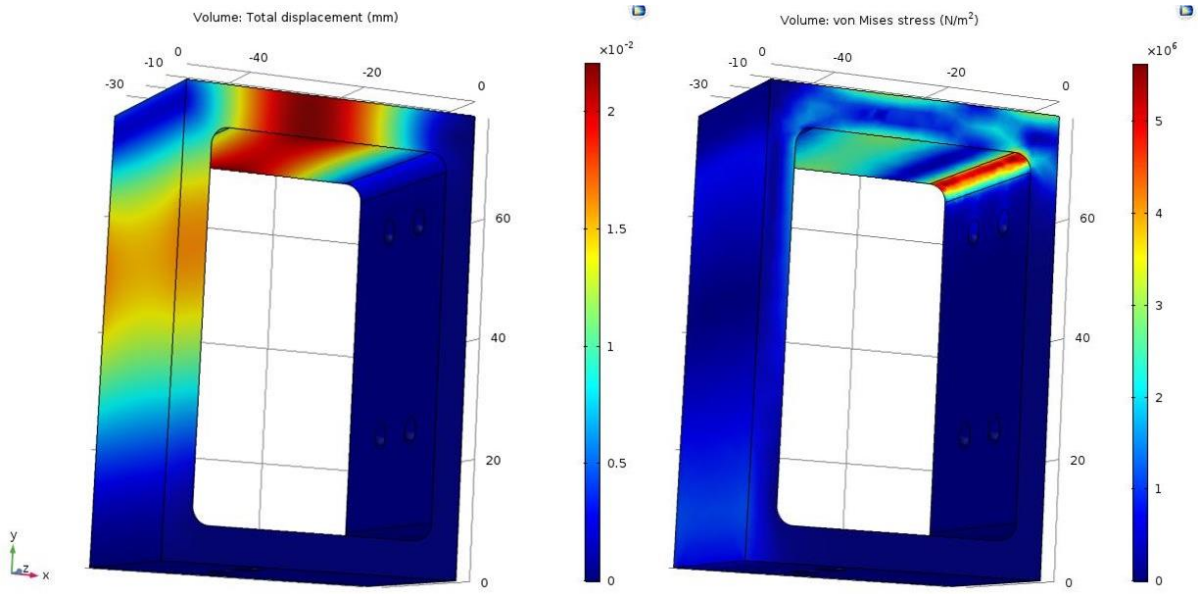

Figure 3.25 (A) the distribution of stress and (B) deformation

were fabricated with CNC machining and were fixed to the overlay with 32 nylon bolts of M4 under shear loading. Result of FEA simulation for the stress distribution and the deformation of this piece under the loading showed that this part is over-designed for carrying the related loading. Result of the simulation is presented in Figure 3.24. The tensile strength of the nylon material used for the bolts is 84MPa, and this strength for shear strength of the bolts can be estimated as half of that value[156] which is equal to 42 MPa. The M4 bolts that were used to fix the nylon anchors to the fiberglass beams can withstand a load of much higher than the expected loading on each of the bolts.

3.4.2 Guidewire

The magnetic guidewires in our experiments are fabricated by bonding a permanent magnet at the tip of a hybrid microguidewire (HYBRID007D, Balt) in the way that the magnetization of the permanent magnet and tether are coaxial and the tip be attracted to MRI. The material used for bonding the two parts is a two-agent epoxy resin with curing time of 24 hours (2.5/1 EPON resin 828 with Epicure 3274, Miller Stephenson).

3.4.3 Guidewire Feeder

The system prepared for feeding the guidewire uses a linear actuator that moves a sliding piece along a leading rode. The linear actuator is driven with a stepper motor and is controlled with a microcontroller board. The stepper motor itself incorporates magnetic parts in its structure, but the lead screw attached to the motor is non-magnetic. The sliding part incorporates a clamp to fix the guidewire in it. So, the guidewire moves with the linear actuator. At the output of the feeder system, a medical y-shaped valve is fixed into a custom 3d-printed support. The catheters can fix to the y-shaped valve, and the microguidewire can be placed inside of the microcatheter. The y-shaped valve has an input for the injection of IV fluid into the microcatheter to minimize the friction between the microcatheter and the microguidewire. This system is shown in Figure 3.25.

One aspect of the design of this system is the compatibility of the actuator with the magnetic fringe field. The functionality of the stepper motor around an MRI scanner was tested to find the limits and the possibilities. It was done by operating a certain rotation with the stepper motor at different strength of the magnetic field in front of the MRI scanner. Starting from the zones with very low strength of the magnetic field ($B<1mT$), the motor was moved closer to the MRI and the same test was repeated. The precision in the functioning of the stepper motor began to fail at the zone where $B\sim0.05T$. The corresponding zone in the fringe field has a distance of ~1.2m from the front face of the MRI along its center axis. Later, the result of this test was used for the preparation of the set-up for the experiments of FFN. Also, the magnetic torque exerted on the motor becomes relatively significant that it may cause problems regarding fixing the feeder system on the table. It is preferable to place this device as close as possible to the end effector of the robot.

At the outlet of the feeding system, a medical y-shaped valve is fixed inside a 3D fabricated support. The universal medical fastener of the valve allows connecting types of the catheter or medical valves to the outlet of the feeding system. So, the guidewire directly inserts into the catheter at the output of the feeding system. When the sliding part of the feeder system is closer to the beginning of the sliding course of the linear actuator, insertion of the long guidewire is prone to the buckling. The ratio of the length to the diameter of the microguidewire is more than 50, and friction between the guidewire and the catheter can hinder the advancement of the guidewire inside the catheter while the system operates to insert the guidewire. Administration of the IV fluid directly into the

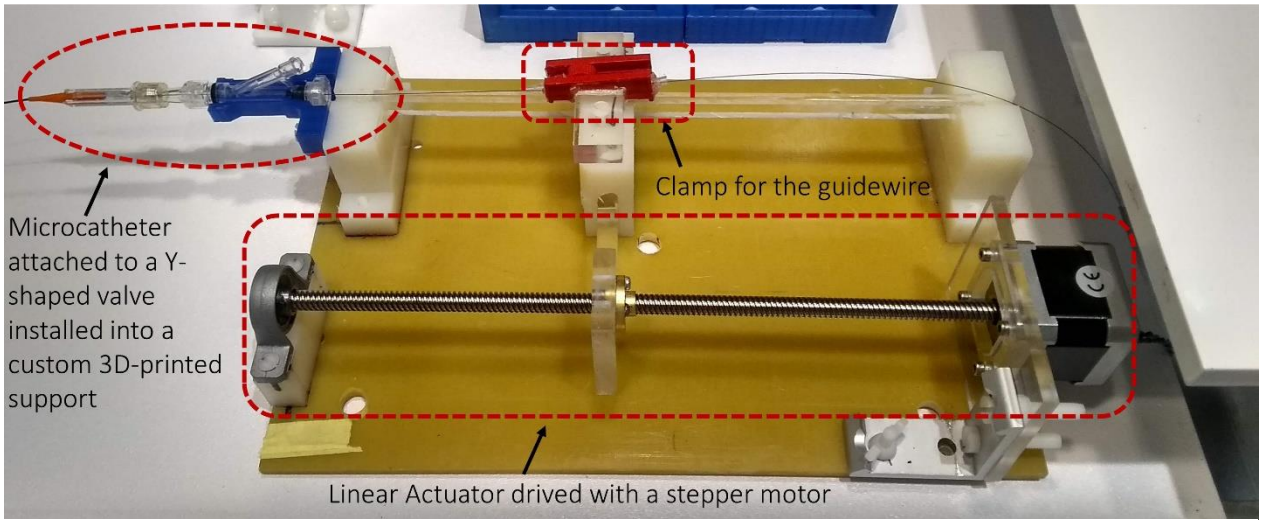

Figure 3.26 the system for feeding the guidewire

catheter and the fact that the guidewire has a hydrophobic coating prevents the problem of buckling of the guidewire during insertion. It was validated during the *in vitro* and *in vivo* experiments.

A drawback of the system of feeding the guidewire is the type of the actuator which is not MRI safe and compatible. A solution to this problem is the use of MRI-safe piezo actuators (rotary or linear motors). In this work, the common stepper motor was used. However, this part can be replaced with piezoelectric motors[157].

3.4.4 Communication with the robot

A server software was prepared to communicate with the robot based on TCP/IP protocol to send the coordinates for step-wise positioning of the table. KRL Ethernet software is used on the robot to transmit data with the server software. For each sequence of FFN, the steps of the manipulation of the table with the robot were prepared in the form of a text file. On the robot side, the motion command of type linear was used to move the table. The server software also communicates with an Arduino board that controls the system of feeding the guidewire.

The robot requires 6 data – three for the position and three for the orientation – to move to a position. These six data for positioning are generated through the process of calculating the sequences of FFN. The robot can execute different types of motion of Linear, Point-to-Point, Circular, and Spline. Among them, the two motion types of Linear and Point-to-Point execute a single motion between an initial position and a target point. Point-to-Point moves the robot along

a trajectory which optimizes the applied torque on each of the drivers of the robot. However, the trajectory that the robot follows for this type of motion is unknown. Also, the robot requires the two information which determines the required rotation of each axis of the robot once it reaches the target. One of these data is a 6bit array, and each bit determines if the angular rotation of each of the axes should be positive or negative regarding the reference of the encoder of each motor when the robot reaches the target. The other data is a three-bit array which determines ambiguous conditions in the position of the robot including the singularities. Determination of these two data is a complex problem requiring to drive equations for the inverse kinematics of the robot. Solving this problem is unnecessary as the controller of the robot is one of the state-of-the-art in the world which uses an advanced algorithm for motion planning[158].

The other type of motion which is appropriate for the FFN project is Linear. This motion only requires the final location to move the end effector (or the tooltip) along a linear trajectory to the target. Therefore, this type of motion was used for the robotic positioning of the table as it enables prediction of the path of moving the table. The movement of the robot for each sequence of FFN is performed with sequential rotation and translation as described earlier. So, the text file generated for each sequence includes one line for each step of the motion. The structure of the data of each line includes three values for X, Y, and Z location of the end-effector, three values for the A, B, and C, rotation of the table, and the number of the pulses that the stepper motor of the feeder system has to rotate at the end of each step. The server software sends the first six values to the robot, and whenever the value for rotating the stepper motor is non-zero, that value will be transmitted to the microcontroller of the feeder system. Figure 3.26 shows the logic of the server software for the transmission of data between different modules. Figure 3.27 is an example of a file containing the locations to which the patient table has to be moved throughout of a sequence of FFN.

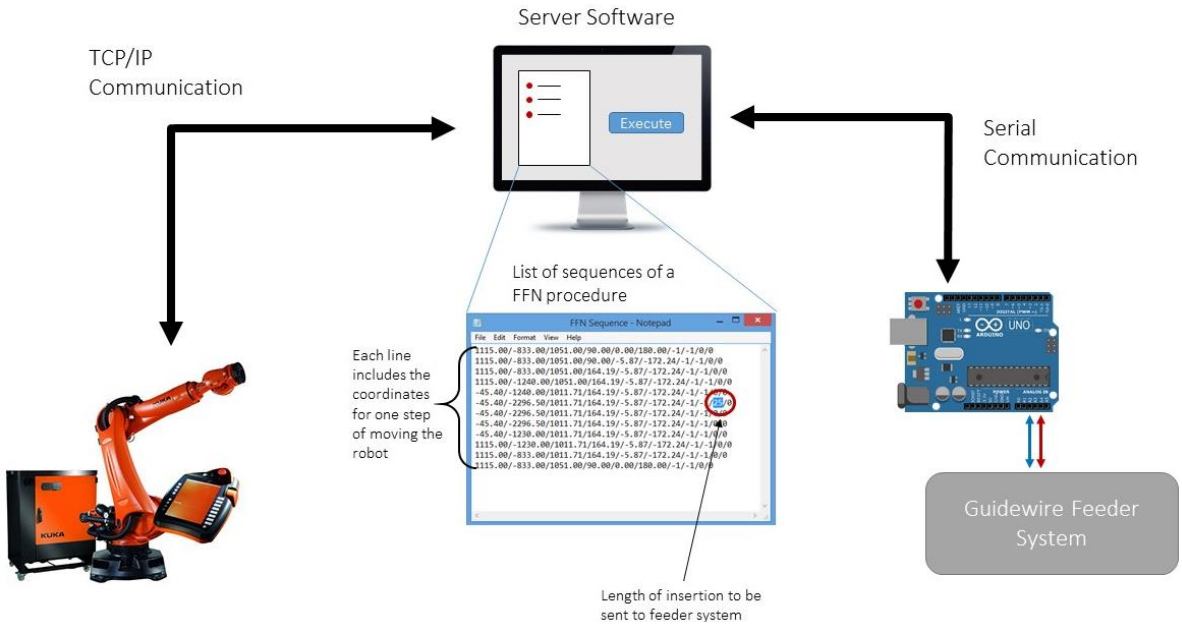

Figure 3.28 Schematic of communication between the server and different modules of the robot and the feeder system.

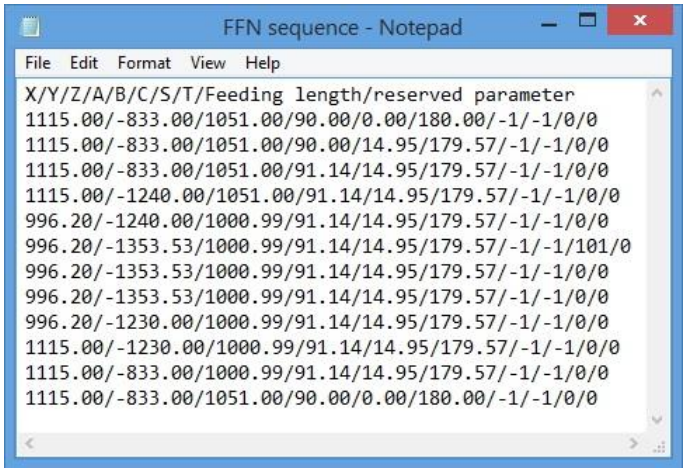

Figure 3.27 A sequence of FFN. Each line contains the coordinates to which the table has to be moved in for each step of the sequential patient positioning. The first and the last line are the HOME location. S and T are parameters related to the movement of the robot and the -1 value is set to use Linear Movement.

CHAPTER 4 *IN VITRO* EXPERIMENTS

4.1 Setup of the experiment

The setup of *in vitro* experiment was prepared by placing the vascular phantom and the feeder system on the robotic table. The feeder was placed close to the end effector of the robot, and the controller of the feeder was placed inside the MRI room. Figure 4.1 shows a setup of *in vitro* FFN experiment. For the experiments that were performed with X-ray guidance, the imaging module was placed inside the room at a location far from the MRI that all the components of the X-ray system were at the zones of the fringe field where B<1mT.

Method of FFN is based on the robotic positioning of the table to align the direction of the vessel ahead of the point at which the tip of the guidewire is placed with the direction of the magnetic gradient force applied from the fringe field. This positioning is a composition of a 3D rotation and translation of the table. Here, the pitch and roll rotation of the table is limited to 15 degrees. This value is chosen from the configurations of a robotic patient positioning system (ORION, LEONI) which has received FDA approval and CE mark.

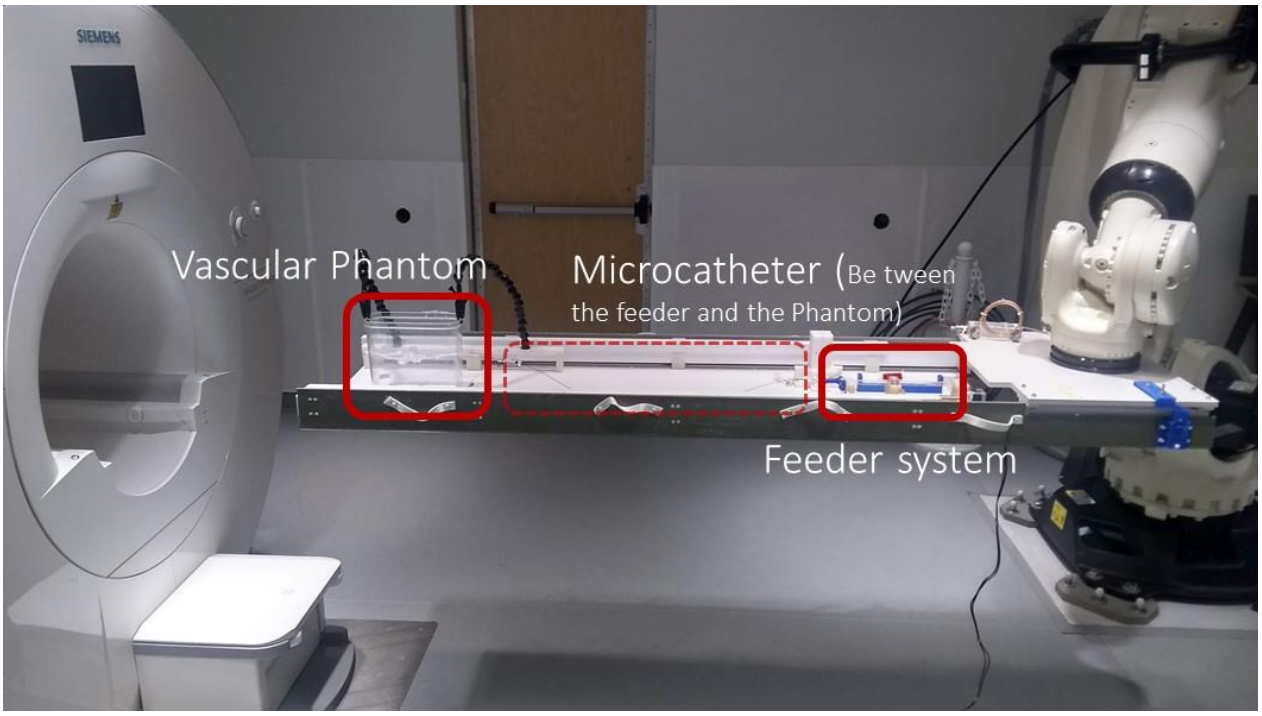

Figure 4.1 a picture of the general setup for *in vitro* FFN experiments

4.1.1 The vascular phantoms

Two vascular models were used for *in vitro* experiments. One is a 2D glass model with multiple bifurcations, and primary experiments of steering the guidewire were performed on it. The internal diameter of the tubes of the model is uniform, and it is 3mm. Then, the rest of the experiments were performed on a 3D and tortuous vascular model with different bifurcations and variation in the diameter of the vessels. The 3D phantom is a realistic vascular model, and further details of it are presented later in this chapter.

4.2 A general picture of the FFN experiments

An FFN intervention to navigate a microguidewire through a path selected on the trajectory is a set of FFN sequences of each to navigate the guidewire through a segment of the path. These sequences are calculated before performing an intervention (experiment) based on the method of FFN navigation. Briefly, each sequence aims to position the patient in a way to align the direction of the vessel with the direction of the magnetic gradient force applied on the tip of the guidewire. Following the steps of performing an FFN intervention is provided and the explanations are supported with pictures from the in vitro experiments.

Preliminary steps to perform an FFN procedure are presented in the Figure below:

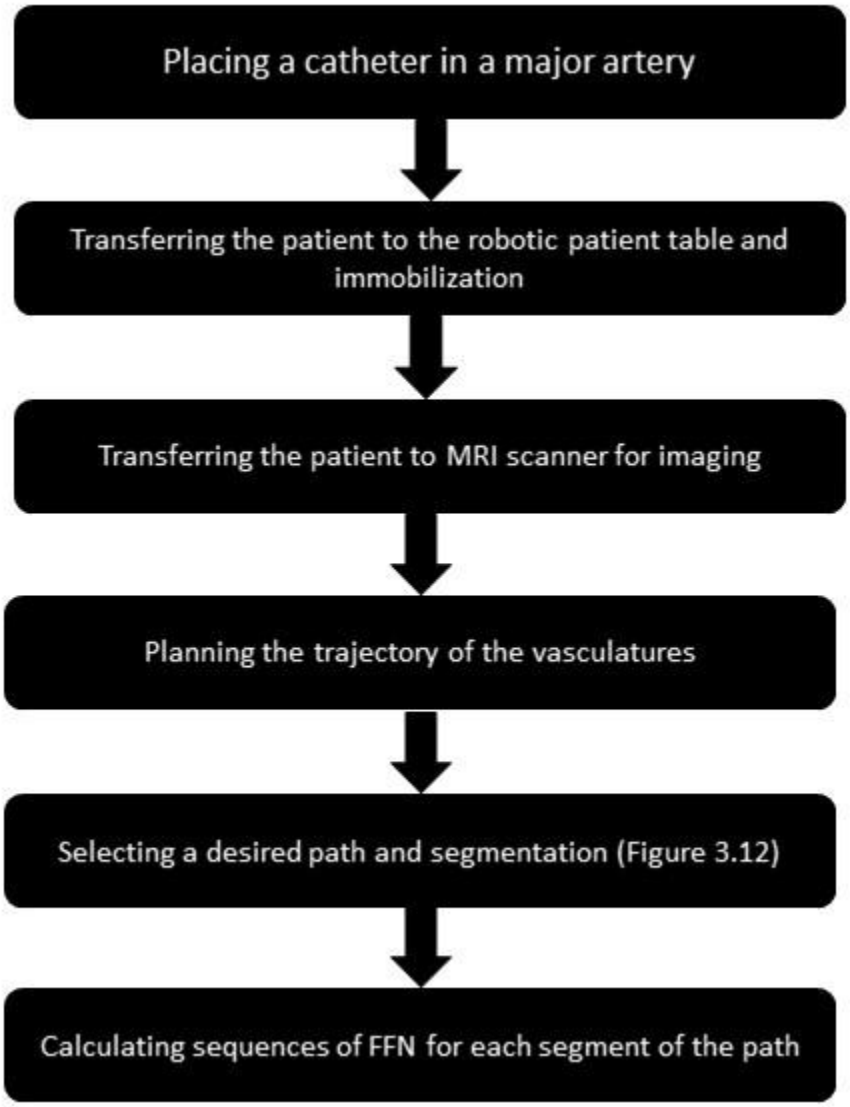

Figure 4.2 Priory steps of performing an FFN experiment

After calculation of the set of the sequence of FFN (each sequence covers a segment of the path as shown in Figure 3.12), and inserting the guidewire inside the body of the patient under fluoroscopy (beginning of the path or the first bifurcation) the sequence of the FFN that is loaded on the server program (see section 3.4.4) can be executed to navigated the guidewire through the segment of the vessel that the sequence corresponding to it has been executed. For all the sequences of FFN, the positioning of the patient begins from a HOME position inside the room (see figure A) to position the patient at the predetermined location for the executed sequence of FFN, stopping the table at

that location and then the server software activate the system for feeding the guidewire by sending the length of insertion to the device. When insertion of the device is completed, the feeder systems sends an acknowledgment signal to the server and the server moves the patient table back to the HOME position. The trajectory that the robot takes to move the patient table to the predetermined location of FFN is described in section 3.7.7 and the returning motion to HOME is the reverse of the path of moving from HOME. In brief, this trajectory is a composition of consecutive rotations of the table at HOME and then orthogonal translations of the table along the coordinate systems of the robot (see Figure 3.1) in the order described in section 3.3.7. Figure X shows some examples of the position of the robot and the patient table at the final location for some sequences of FFN. After completion of a sequence of FFN and moving the table back to HOME, the operator of the software program executes the command to move the table to the location of the x-ray imaging system (for image-guiding of the procedure). Then, images with x-ray are taken to validate the success of the navigation for the executed sequence of FFN and to check whether or not the tip of the guidewire has been advanced to the end of the segment of the path. Upon validation of the success of the executed sequence of FFN through imaging, the next sequence of FFN that navigates the guidewire along the next segment of the path can be executed.

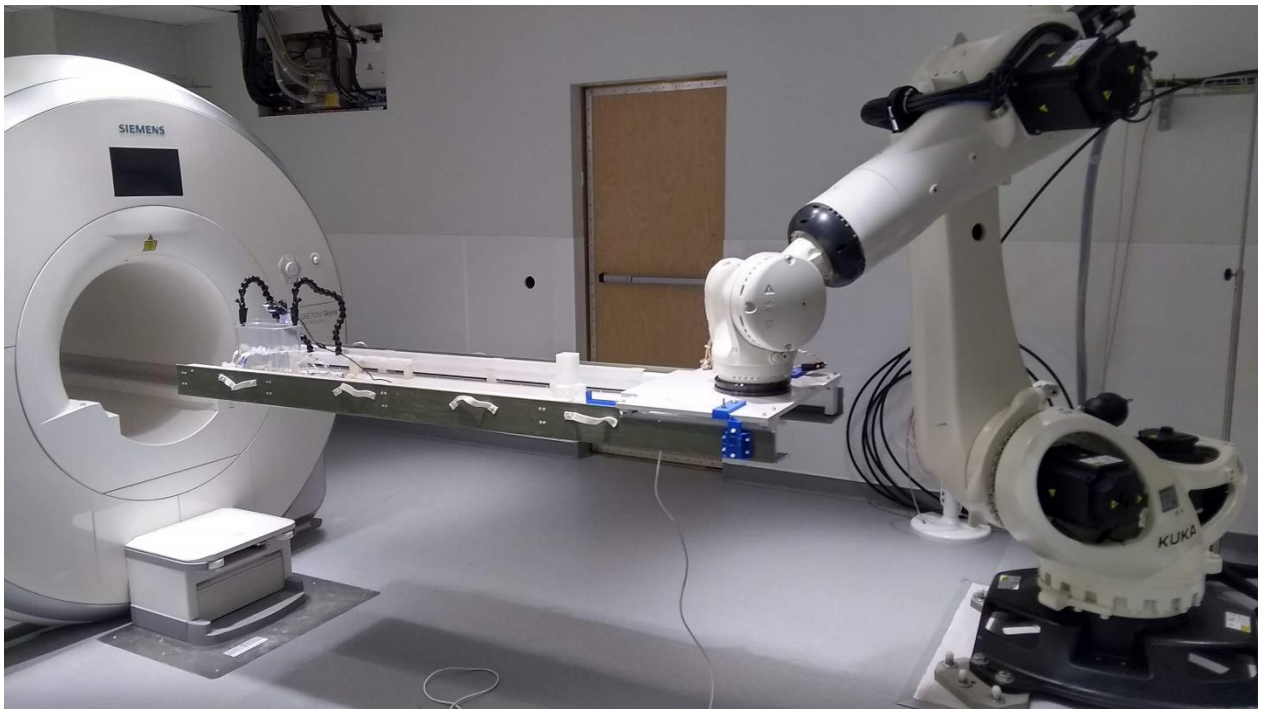

Figure 4.3 The HOME position in an FFN experiment (procedure)

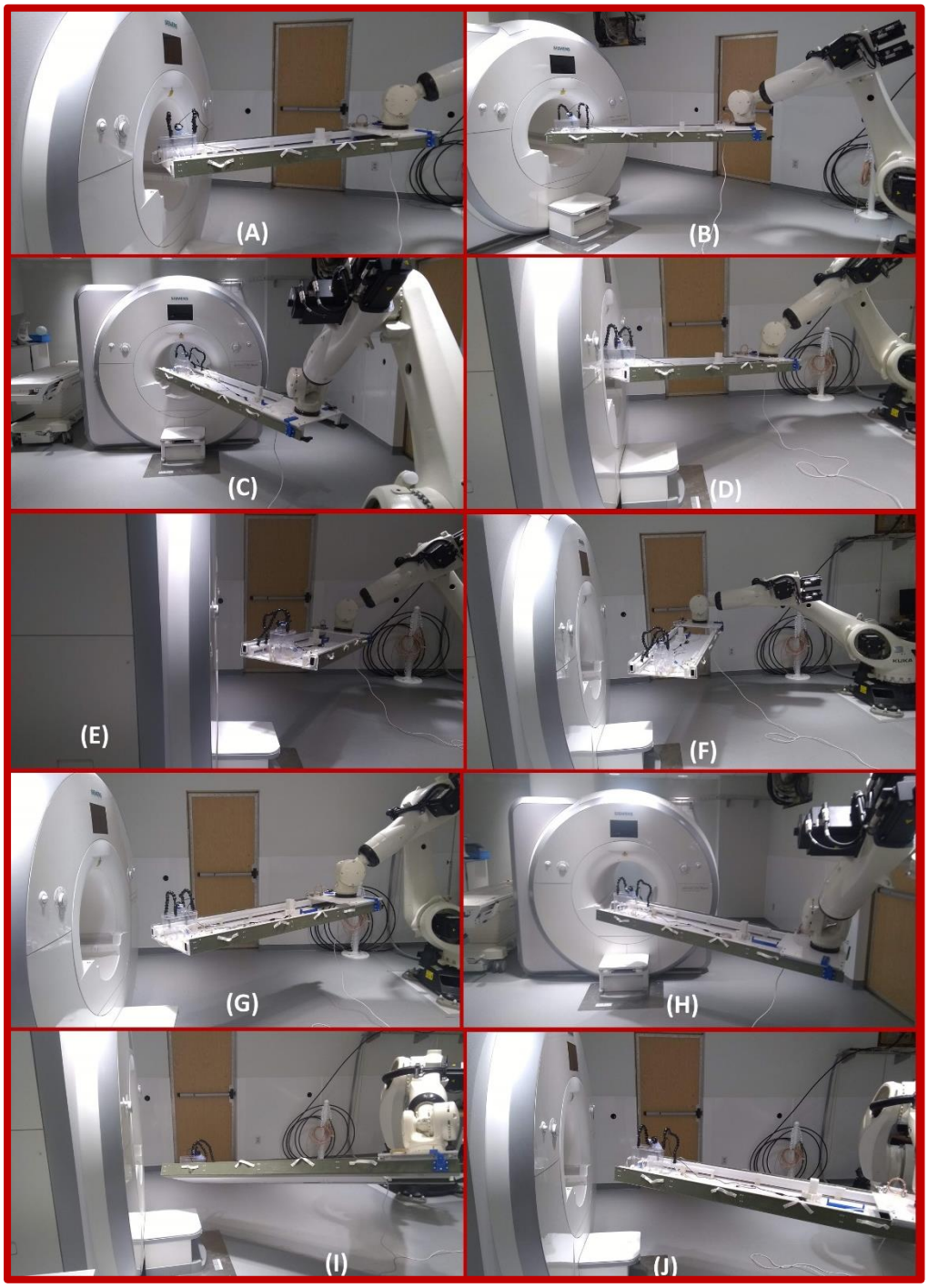

Figure 4.4 Robotic Positioning of the table for some examples of the sequences of FFN. In (A-D) moving the table partially inside the MRI bore and in (E-J) the table is entirely outside of the MRI scanner

4.3 Navigation in the 2D model

In FFN, both of the actuation mechanisms of the magnetic torque and the magnetic gradient force simultaneously apply on the tip. The role of the magnetic gradient force is to overcome the problem in the insertion of the guidewire once the friction and softness of the distal of the guidewire limit the advancement of the guidewire. It is considered to be advantageous for targeting narrow and tortuous vessels. However, the simpler vascular structure may not need the pulling force on the tip and insertion of the device from the other end may suffice. Navigation of the guidewire to peripheral abdominal arteries may be possible with steering the tip of the guidewire and insertion of the device. Steering the guidewire is possible with applying the torque at the tip of the guidewire. Here, the results of *in vitro* experiments of FFN to steer the guidewire in the multibifurcation 2D vascular structure is presented.

Two other goals were pursued in this set of experiments. First, to validate the accuracy of the map of the fringe field and second, investigating that the magnetic tip of the guidewire can align with the direction of the external magnetic field and to investigate on the impact of the stiffness of the tether. The method of steering in this experiment is to align the direction of the vessel with the direction of the magnetic field in the map of the fringe field. So, alignment of the permanent magnet tip of the guidewire with the direction of the vessel is considered as the way to investigate the goals. The validity of the alignment of the vessels with the external magnetic field is also investigated by probing the direction of the magnetic fringe field around the vessel using a 3D magnetic probe.

The guidewire used for this experiment was fabricated by the bonding of a tubular neodymium permanent magnet with ID and OD of 0.5mm, and 1mm, and the length of 1mm. Trajectory of the phantom shown in Figure 4.5 was prepared by use of the location of different bifurcations of the phantom. The sequences of navigation were calculated to align the direction of the vessel with the direction of the external magnetic field. The guidewire was manually inserted along the length of the vessel until the next bifurcation and the locations at which the direction of the vessel changes. The location and direction of all the bifurcations of the phantom were defined in the coordinate system of the table. Different experiments were conducted by changing the location of the phantom on the table. For each bifurcation, the strength of the magnetic field used for the experiment was in the range of 0.05T to the highest available, and for each bifurcation, different sequences were

defined. Also, different regions around the MRI with different Field-Gradient-Deviation was utilized.

Figure 4.1 shows the placement of the tip of the guidewire after passing over seven bifurcations. For all the sequences of steering the guidewire at different locations on the phantom, once the strength of the magnetic field was above 0.07T, the tip of the guidewire aligned with the external magnetic field (direction of the vessel). From this result, it can be concluded that for the configuration of the guidewire used here, it can be expected that the tip of the guidewire can align with the external field at any location where B>0.1T. This result supports the assumption used to generate the map of the magnetic gradient force which is discussed in the previous chapter. Also, the accuracy of the map of the fringe field was validated through this experiment. As, the direction of the vessels on the phantom is supposed to be aligned with the external magnetic field, and for each sequence of the experiment, the alignment of the permanent magnet tip with the direction of the vessel was investigated by probing the direction of the magnetic field lines. Although this experiment does not validate the accuracy of the strength of the magnetic field at a different point,

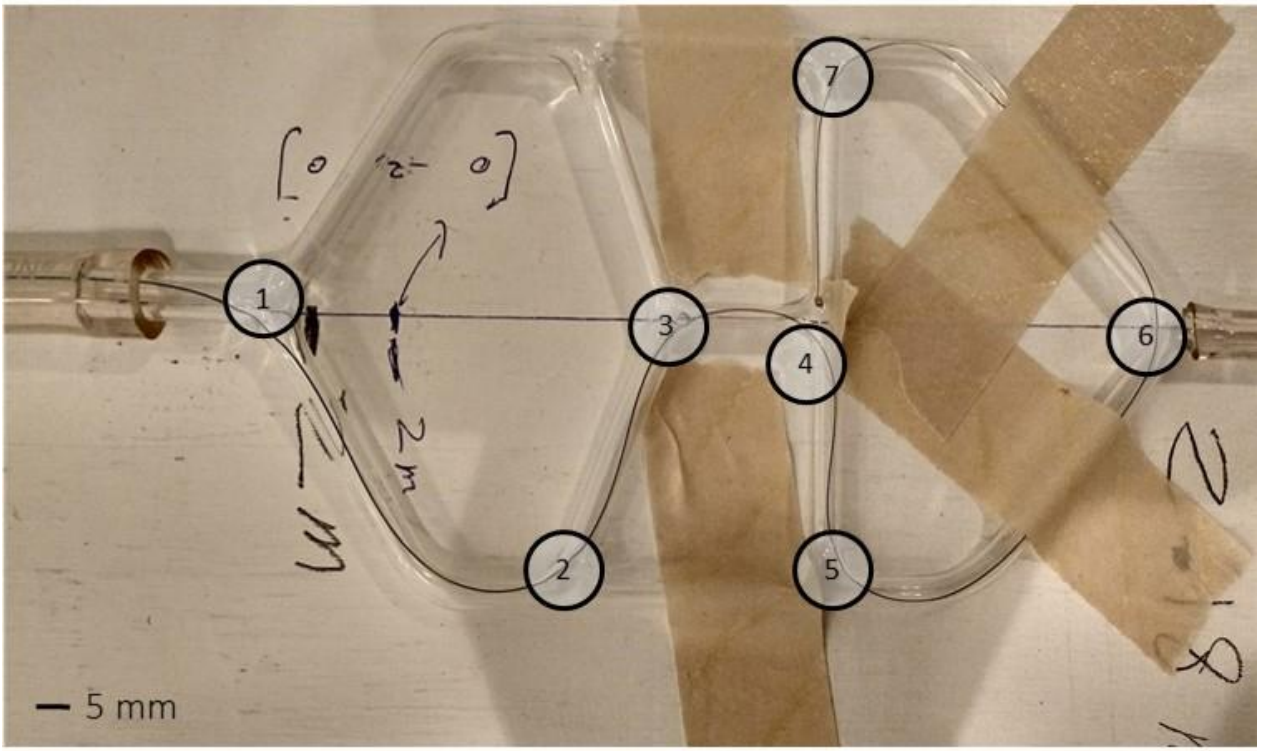

Figure 4.5 result of FFN experiment with a 2D phantom

however, the direction of the lines of the magnetic field is modeled with a reliable accuracy for the purpose of the navigation.

4.4 Navigation in 3D vascular structure

Result of the experiments with FFN presented in the previous section showed the possibility of steering the guidewire at the bifurcation by exploiting the magnetic torque mechanism. The inside diameter of the vascular model was relatively large, and it lacked tortuosity. Also, the model was 2D. In this section, results of *in vitro* experiment of FFN in a 3D model is presented. This model is shown in Figure 4.6. The vascular model used for this *in vitro* experiment is a 3D model that includes different targets with multiple bifurcations. The internal diameter of the vessels varies in the range of ~7mm at its main trunk to about 1mm at the narrowest part for the vessel that reaches to Target 2 as shown in Figure 4.6. This phantom model includes certain physiological features of the navigation through multi bifurcations paths (maximum 3), tortuous path, narrow blood vessels

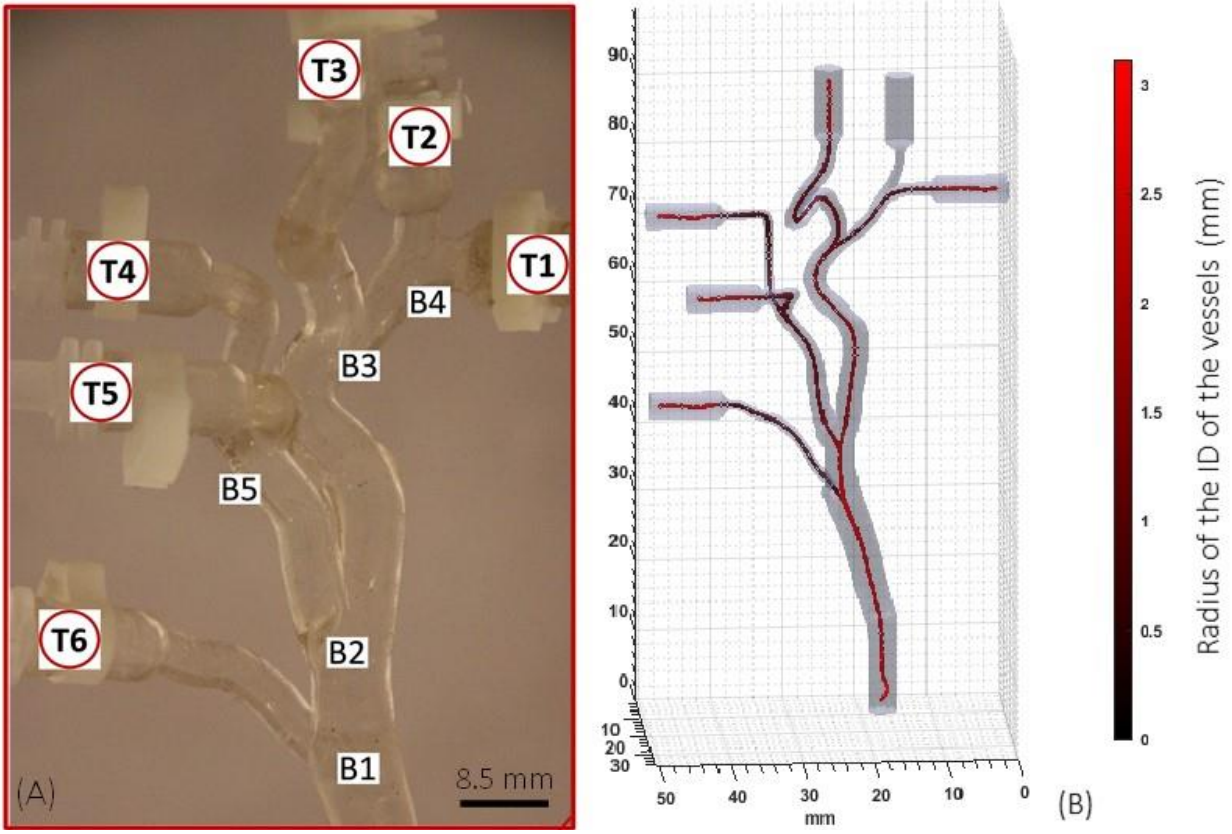

Figure 4.6 (A) the 3D phantom used for *in vitro* experiments and (B) the internal radius of different parts of the phantom

(in range of 1mm to 2mm in diameter) and navigation from a large vessel into a narrow vessel for target 6 (from ~7mm into ~1.5mm in diameter).

In vitro FFN experiments of navigating a microguidewire to all the targets on the vascular model are performed by defining sequences that exploited the highest available magnetic actuation. The smallest magnetic body we used for the tip of the microguidewire is a tube-shaped neodymium permanent magnet of grade N50 with OD and ID of 1 mm and 0.5 mm and the length of 0.5 mm with an equivalent spherical radius of 0.416mm, as shown in Figure 4.7. Map of the magnetic gradient force from the fringe field was calculated by assuming that the external magnetic field

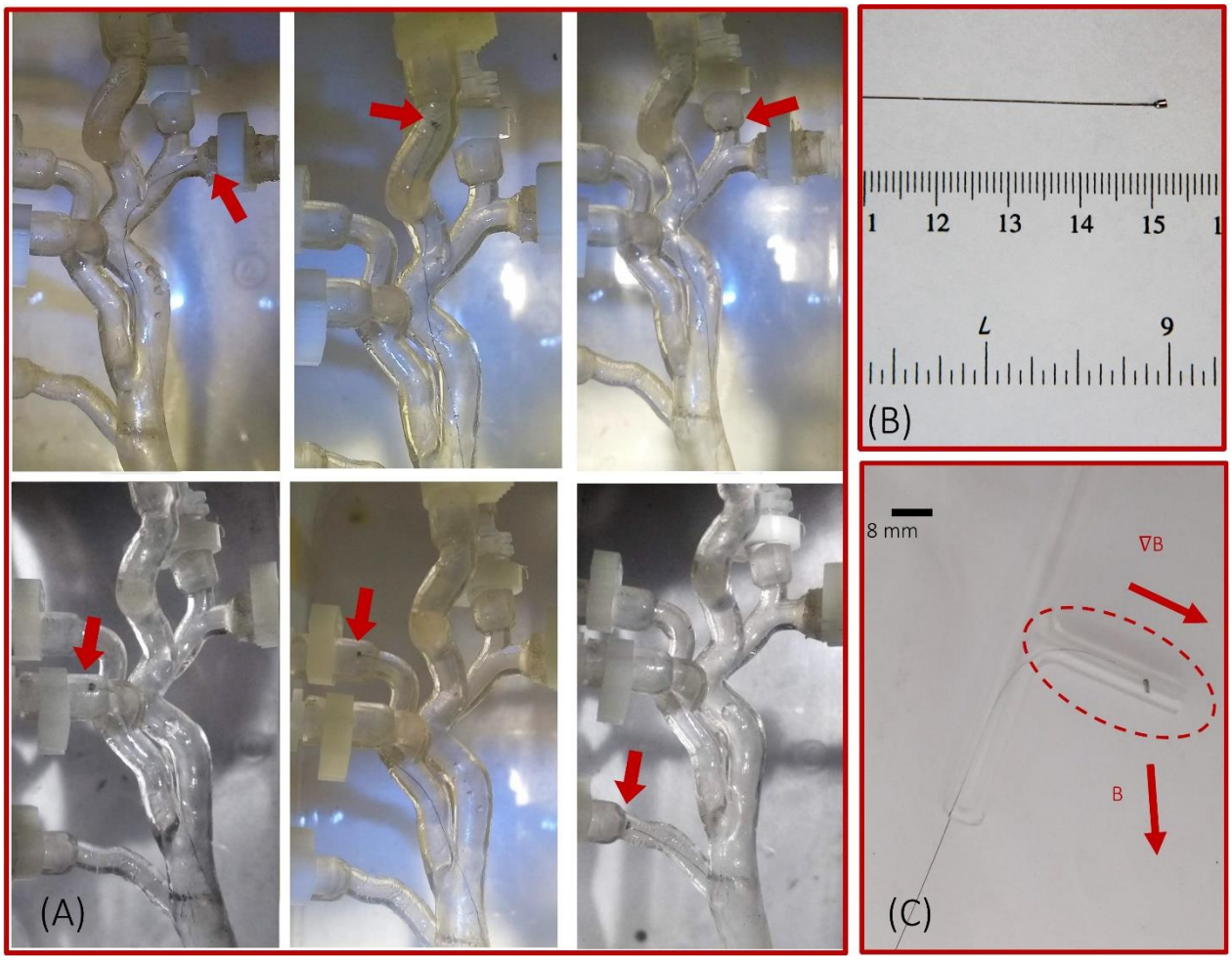

Figure 4.7 (A) result of navigation of the custom microguidewire shown in (B) to different targets of the 3D phantom and the red arrows point to the magnetic tip of the guidewire. (C) shows an example of the impact of large field-gradient-deviation on the tip of the guidewire (the crook)

from the fringe field can rotate the magnetic tip of the guidewire to align its magnetization direction with the external magnetic field. Different experiments were designed for navigation to all the targets by placing the phantom at the different locations on the patient table. Experiments for targets 1, 2, 4, 5, and 6 were possible to be performed by sequences that exploited zones in the fringe field were B> 0.5 T and ∇B >2 T/m and the field-gradient-deviation is less than 20 degrees. In the experiments, it was observed that when the field-gradient-deviation is more than 30 degrees, a noticeable kink occur at the tip of the guidewire. Example of this kink is shown in Figure 4.7. This kink affects the maneuverability of the tip. It is because the magnetic field rotates the tip to align its magnetization with the external magnetic field while the tether is under tension by the magnetic gradient force exerted on the tip. For target 5, the experiment performed by using a longer (larger) permanent magnet for the tip (length of 1mm) failed due to the lack of space for maneuverability of the tip of the guidewire after bifurcation 5. Navigation along this route was successful when the shorter (smaller) permanent magnet was used for the tip. It has to be mentioned that the material used for bonding the guidewire to the magnet added to the total length of the solid tip. The failure happened at the section where the inside diameter of the vessel is less than 1.5mm. From this result, it can be concluded that using a smaller tip is important to improve the maneuverability of the tip of the tether to enable navigation into narrow, tortuous vessels. However, still providing adequate actuation is necessary. The direction of the vessel after bifurcation three toward target 3 was perpendicular to the overlay of the patient table for the way that we initially prepared the phantom and fixed it inside a box. For that section of the vessel, zones in THE FRINGE FIELD was used for the navigation that has a large field-gradient-deviation (>45 degrees). Also, the range of the strength of the magnetic field for sequences of navigation was between 0.1T to 0.5T. Those sequences are considered as not to be optimal situations for FFN. The success of the experiment for navigation to target 3 was low and giving shocks to the guidewire by turning the tether along its central axis or giving slack by extra feeding was helping to insert the guidewire. However, this section was navigated successfully by rotating the phantom and changing the direction of the vessel and so defining new sequences of FFN that exploited stronger magnetic actuation (B>0.5T and ∇B>2T/m). Such a change in the position of the phantom can be viewed as changing the recumbent position of the patient on the table. Figure 4.7 shows the final results of the experiments to place the tip of the guidewire at each target.

The importance of collision-free robotic positioning of the patient in FFN is undeniable for the safety, the required time to plan a procedure and automating FFN. Conditions that were established for robotic positioning and predicting collision was validated to be safe throughout all *in vitro* FFN experiments. Collisions between the table and different objects inside the room and the robot structure were considered to be avoided. The safety of the collision-free robotic patient positioning later enabled to do *in vivo* experiment without worrying about the collision.

4.4.1 x-ray Guidance of navigation

Guiding the experiments was done by x-ray imaging. Required markers for the experiment was fixed on the box of the phantom at a known location relative to the vascular model. Examples of the cases of using the x-ray imaging for validation of the location of the tip of the guidewire throughout an FFN experiment are presented in Figure 4.8. The way this data was used is approximating the expected position of the tip at the end of each sequence by registration of the vascular trajectory (which is an indexed data) on the x-ray image using a geometrical approach (method described as supplementary material). Then the actual position of the tip of the guidewire inside the vessels was adjusted by either pulling the guidewire back (in case of passing the expected location) or repeating the previous FFN sequence and insertion of the guidewire. Another use for the x-ray image and registration of vascular model was placing the tip of the guidewire at the initial point of the vascular trajectory at the beginning of the experiment.

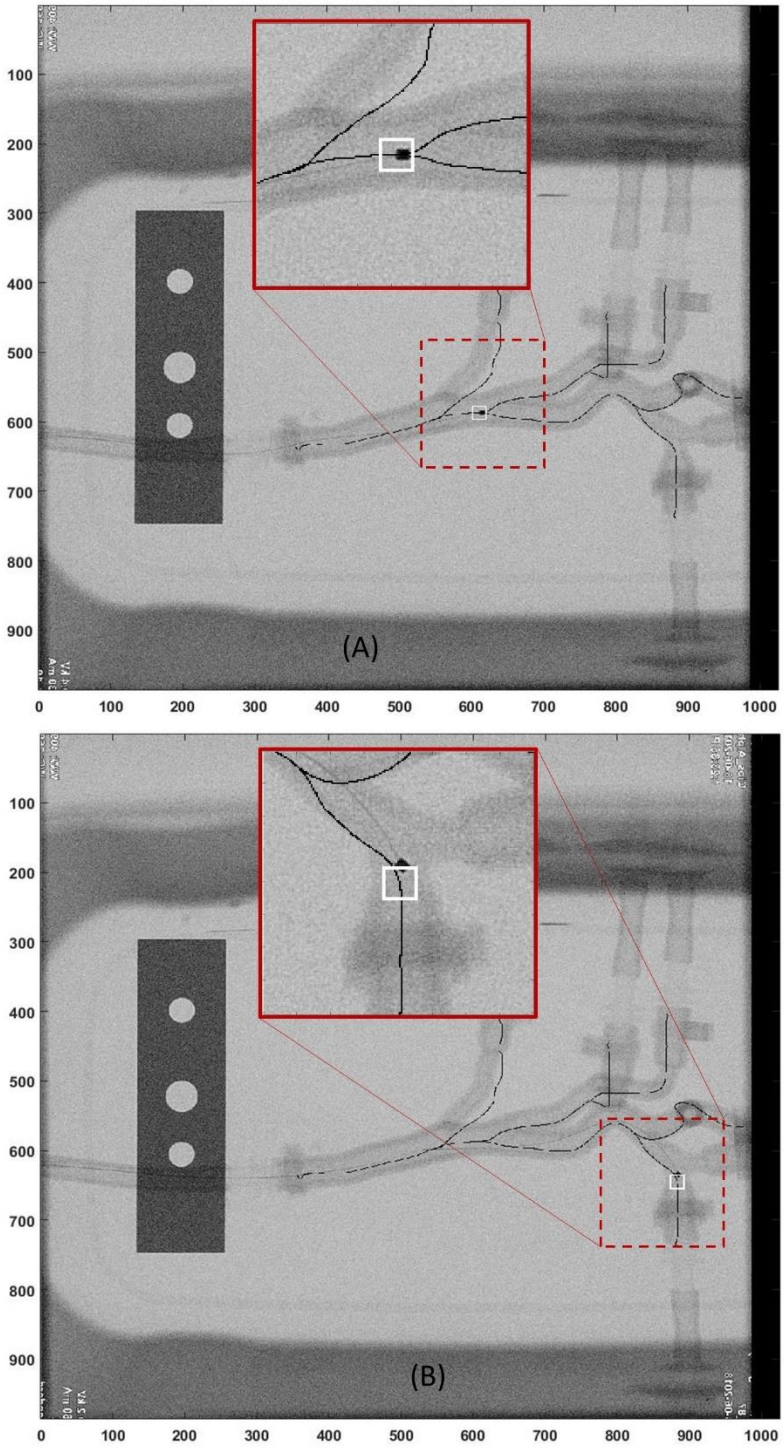

Figure 4.8 (A) and (B) are two examples of using the vascular registration (black lines) on an x-ray image and locating the expected location of the tip of the guidewire (white squares). The markers were made by making holes on a plate of aluminum.

4.5 Miniaturization of the tip

An objective of FFN is to successfully navigate the guidewire in narrow blood vessels in a trade-off of miniaturizing the magnet attached to the tip of the microguidewire and using stronger gradient and strength from the fringe field. Decreasing the volume of the magnetic tip corresponds to a weaker magnetic actuation. Here, instead of using a smaller magnetic tip, FFN experiments were designed that exploited weaker magnetic actuation by selecting thresholds for the highest acceptable strength of the magnetic field and so the gradient of the magnetic field. In general, the strength of the magnetic field and the magnitude of the gradient of the magnetic field decrease by distance from the scanner in the fringe field and it can be concluded that the lower the strength of the magnetic field corresponds to the lower the magnetic of the gradient of the magnetic field.

Experiments to navigate the guidewire were planned by defining sequences of FFN for all the targets on the 3D phantom except target three by choosing upper thresholds for the highest admissible strength of the magnetic field. The goal was to find the lowest magnetic actuation that hinders successful navigation to the targets. The guidewire was the same guidewire as used in the previous experiments, and the permanent magnet tip had an equivalent spherical diameter of 0.816mm.

For the targets 1 and 2, the most challenging part was the navigation at bifurcation 3 and the distance after that toward the bifurcation 4. The Experiments to steer the guidewire in the desired branch were unsuccessful for the sequences that exploited a magnetic field in the range of 0.15T to 0.25T where the gradient is about 0.3T/m to 0.6T/m. Adding extra bending at the tip by the magnetic field did not enable to steer the guidewire into bifurcation 3 when B~0.2T. Insertion of the guidewire along the distance between bifurcation 3 and bifurcation 4 was also unsuccessful by use of the magnetic gradient of less than 0.5T/m at the zones where the strength of the magnetic field was less than 0.2T. To describe the failure, while the other end of the guidewire was being inserted, the tip of the guidewire was not advancing in the vessel, and the guidewire was crooking at its distal. For target 5, navigation of the guidewire into the bifurcation 5 and after that failed for sequences that exploited the strength of the magnetic field of less than 0.35T where the gradient is about 0.7T/m. This threshold for T6 was about 0.15T.

A conclusion of this experiment is the possibility of miniaturization of the magnetic tip with FFN to enable targeting smaller vessels and retrieval of the guidewire through a microcatheter. Here, a permanent magnet with an equivalent spherical diameter that can move through the lumen of a catheter with an ID of 3Fr. However, the smaller tip can be used, and while the reduction of the volume leads to weaker magnetic actuation, the higher gradient and the strength of the magnetic field available in the fringe field can compensate for that.

4.6 Impact of the magnetic gradient force

Intermittent contacts between the guidewire and the vessel walls in the tortuous vascular structure induce resistive forces on the guidewire that affects the insertion of the device. As a result, while the guidewire can be inserted from its other end outside of the body, the tip of the guidewire does not advance inside the vessel and the distal section of the guidewire crooks. FFN is considered to provide a solution for this issue by applying a pulling force at the tip to enable further insertion of the tip of the guidewire.

In *in vitro* experiments, it was observed that it is not possible to do further insertion of the guidewire at each of the targets of the phantom without FFN. The observation was done when the tip of the guidewire was at different targets, and the phantom was away from the MRI ($B<0.5$mT). So, experiments were designed to investigate the impact of a pulling force applied on the tip to further insert the guidewire. The experiment was done by using the strong pulling force ($\nabla B> 2$ T/m), and a weak pulling force ($\nabla B \in \{0.5 \text{ to } 1\text{T/m}\}$). The phantom was filled with water, and the guidewire used for the experiment had a hydrophobic coating. The tip of the guidewire was placed at each of the targets of the phantom, and the patient table was positioned in a way to align the magnetic gradient force with the direction of the vessel. This experiment was done for targets 1, 2, 3, and five which for all of them, long, tortuous sections has to be passed to reach the targets.

In all the cases, using a stronger pulling force helped to insert the guidewire further while it was impossible in case of not using a pulling force. Figure 4.9 shows the difference in distance the guidewire was inserted by the help of the magnetic gradient force in comparison with the failure in insertion without FFN that led to crooking the distal of the guidewire. Also, in one experiment, because the magnetic tip broke from the guidewire while the guidewire tip was at target 3, it was observed that further insertion of the guidewire that has no magnetic tip is not possible. As the

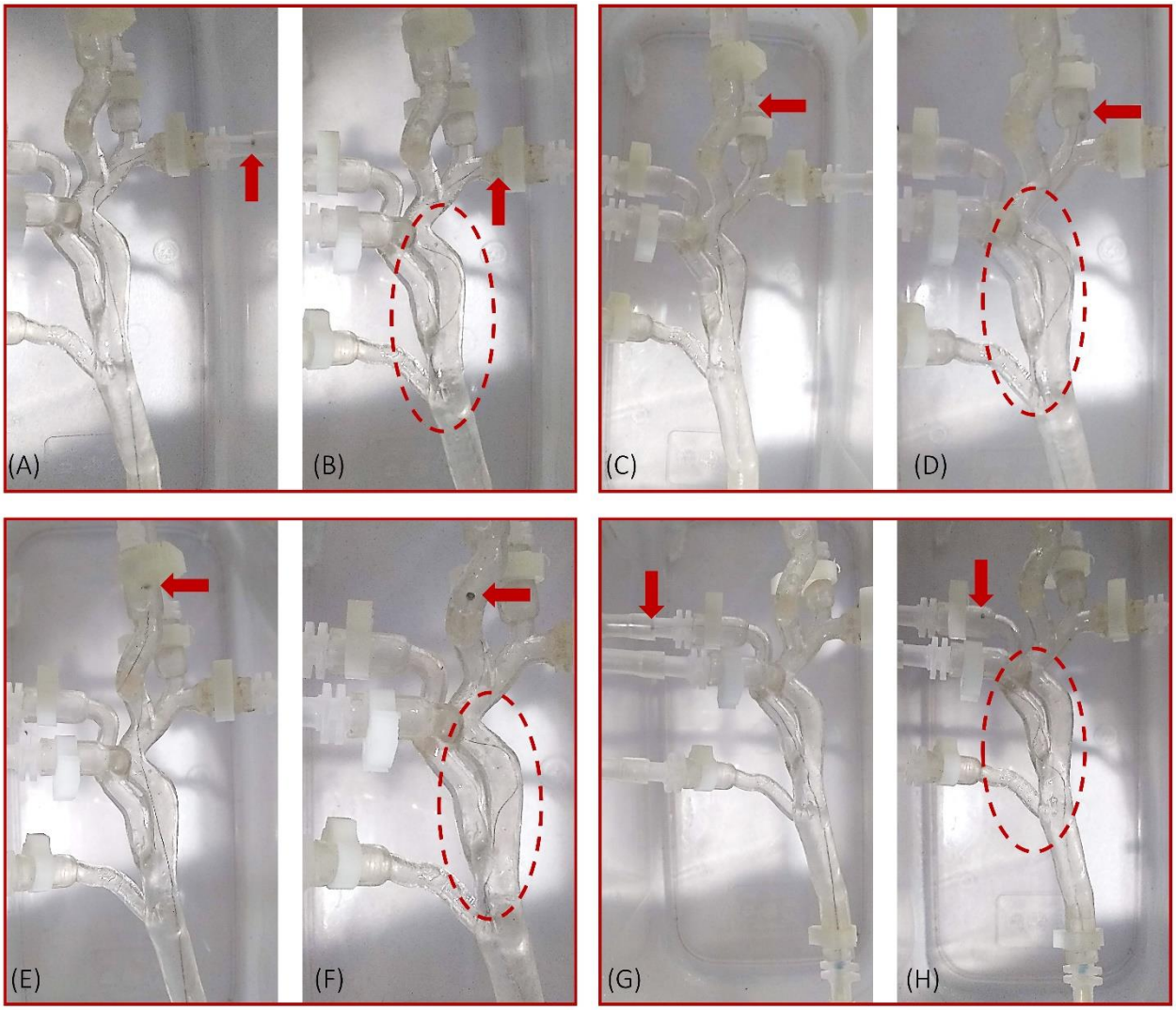

Figure 4.9 (A, C, E, and G) examples of the impact of using the pulling force applied on the tip of the guidewire to insert the guidewire beyond the limit of the possibility of insertion manually from the other end of the guidewire (B, D, F, and H). The dashed ovals show the crooks at the distal of the guidewires. Red arrows point to the tip of the guidewire.

guidewire device was a neurological guidewire which is in clinical use, inability to insert the device without the pulling force on its tip, it shows that this force is essential to access to the locations deeper in the vascular system. These results are evidence that the strong pulling force applied on the tip enables to insert the guidewire further into the blood vessel when the insertion of the guidewire from the other end is not adequate for the advancement of the tip of the guidewire in vessels.

4.7 Robustness in FFN

FFN is based on the robotic positioning of the patient in the magnetic fringe field of the MRI scanners. The method of the navigation can be interpreted as the positioning of a point inside the body of the patient at a point inside the space of the room with proper orientation. Different factors can violate the accuracy of the positioning. For example, the abdominal organs are deformable, and respiration and gravity can change the form and direction of the vessels. Also, Body of the patient may move throughout of a whole FFN procedure. Distortion artifact in the MRI imaging affects the accuracy of the vascular model while the placement of the reference markers and their localization in the medical images is prone to error. These examples and other possible reasons may lead to inaccuracy in the patient positioning required in FFN. One way to approach this problem is to investigate the robustness of FFN against the error in the positioning of the blood vessels. In chapter 2, the structure of the fringe field and the curvature of the lines of the field was investigated. It was shown that the local uniformity in front of the MRI tunnel is relatively large. This local uniformity is considered a mean to define the robustness in FFN against the error in the positioning.

This robustness was investigated *in vitro* by placing the phantom at a location different than the location used for defining the sequences of FFN. For the 2D model, this distance was up to 4cm and success in the steering the guidewire was achieved for all the bifurcations. For the 3D model, the error of up to 2cm was included in the positioning and navigation to the different targets was achieved. Results of these experiments are evidence that the navigation with FFN is robust against the accuracy in the positioning. However, the extent of this robustness which is depended on the zone in the fringe field used for the navigation and the structure of the vessels and the bifurcations is not investigated.

4.8 Discussion and Conclusion

In vitro FFN experiment was performed on the vascular models with multiple bifurcations. A microguidewire with a magnetic tip with a diameter of 1mm was advanced into a vessel with almost the same diameter (Target 2) after passing a tortuous path and 3 bifurcations. FFN provides a large range of magnetic actuation. It was shown that the size of the tip can be optimized to make targeting

vessels with a diameter in the range of 1mm possible. Robustness of FFN against error in 6 DOF robotic positioning was also investigated. The large size of MRI and so the fringe field motivated the investigation in the local uniformity in the fringe field which in this chapter its importance on the robustness of FFN was empirically investigated. All these results, and the safety of automatically planning an FFN intervention which can be broken down to the set of the sequences along with a protocol to follow for an experiment in a more complicated context of *in vivo* were bases to proceed to perform FFN experiment on an animal model as it is presented in the next chapter.

CHAPTER 5 *IN VIVO* FFN EXPERIMENTS

5.1 General

In vivo FFN experiment was performed in the neck and brain arteries of swine animal model to navigate microguidewire with a magnetic tip into branches of the common carotid artery (CCA). Two animals with the weights of 25Kg and 24 Kg were used for the experiment. All the animals were treated humanely and according to the guideline of the ethics committee of the University of Montréal. The ethics committee of the University of Montréal approved the protocol of the experiment. The animal model was a farm breed swine. In this chapter, the required facilities, steps of the preparation of the animal, and the results of FFN experiments are presented. A Matlab Application was prepared for performing different computations required for an FFN experiment. This app is described in Appendix E.

5.2 Intervention facility

This section aims to describe the preliminary steps and peripheral facilities for performing *in vivo* experiment. The complete facility for *in vivo* FFN experiment has a larger extent than the requirements for an *in vitro* experiment. The layout of the room facility includes spaces for keeping the animal and a place dedicated to the preparation of the animal for the experiment including the surgeries. Intubation of the respiratory tract and putting the animal under general anesthesia is done in a separate room. After anesthesia, the animal is transferred to the overlay part of the patient table which is fixed on a portable table for initial catheterization. In this step, the animal is transferred to a second room to perform surgery for vascular access and vascular intervention. At this step, access to the femoral artery of the animal, and placing a catheter in the carotid artery are performed. Catheterization of the carotid artery was done under fluoroscopy guidance which it requires using a radio-opaque portable table for the surgery. After completion of the catheterization of the carotid artery, the animal was immobilized to the patient table and transferred to the FFN intervention room. The layout of the intervention facilities for the *in vivo* experiment is presented in Figure 5.1.

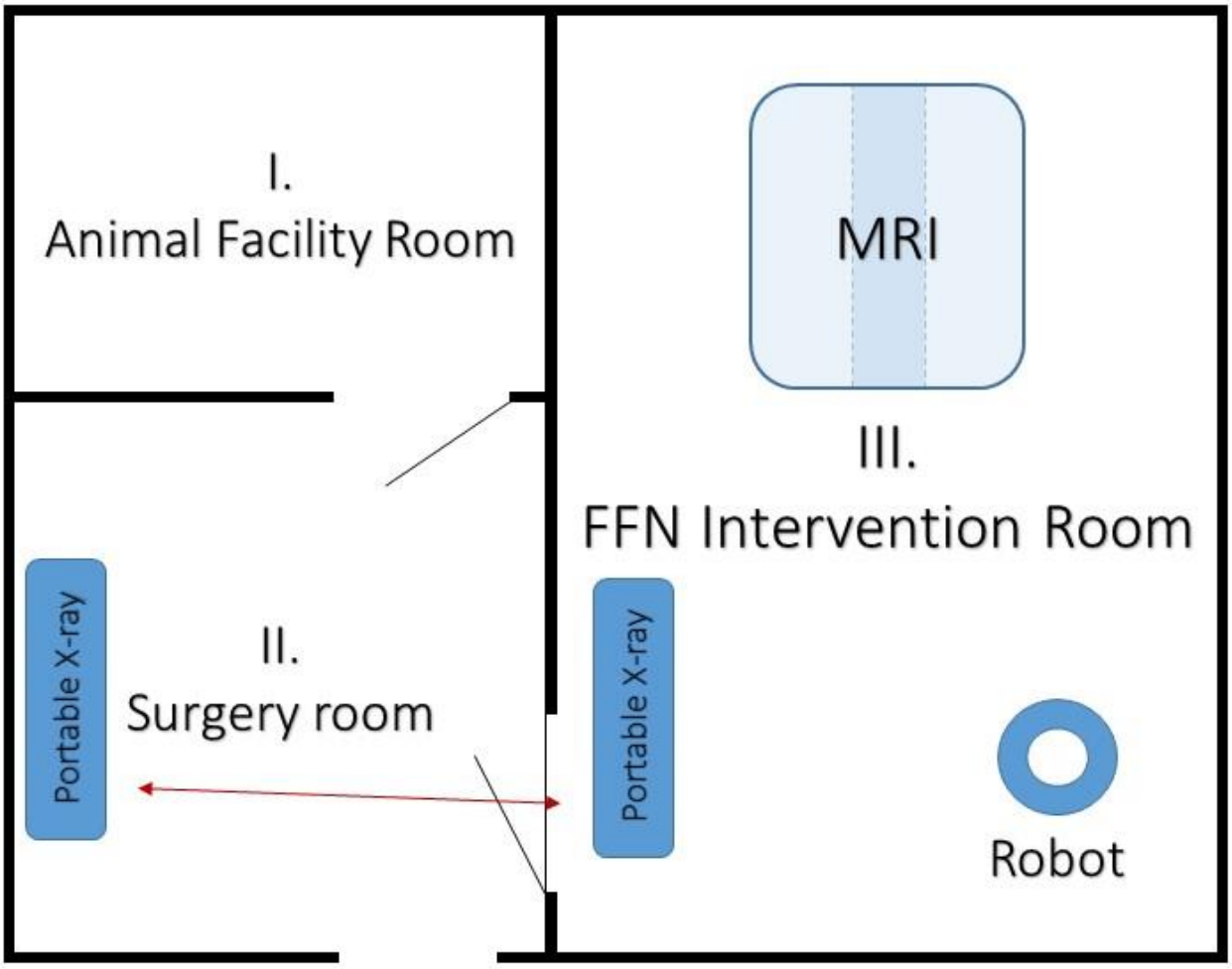

Figure 5.1 the layout of the rooms and the facilities for *in vivo* FFN experiment

The X-ray imaging system is a portable unit that was used for guiding the catheterization and FFN experiment, and it was transferred between the two rooms for each stage of the experiment.

One of the causes of the complications in catheterization is the mechanical force between the vessel walls and the catheter. A critical step in an FFN procedure is transferring the patient after the surgery to the venue of FFN intervention and mounting the patient overlay on the robotic manipulator or the table of the MRI scanner. Minimizing the risk of damaging the vessels during transferring the patient is critical.

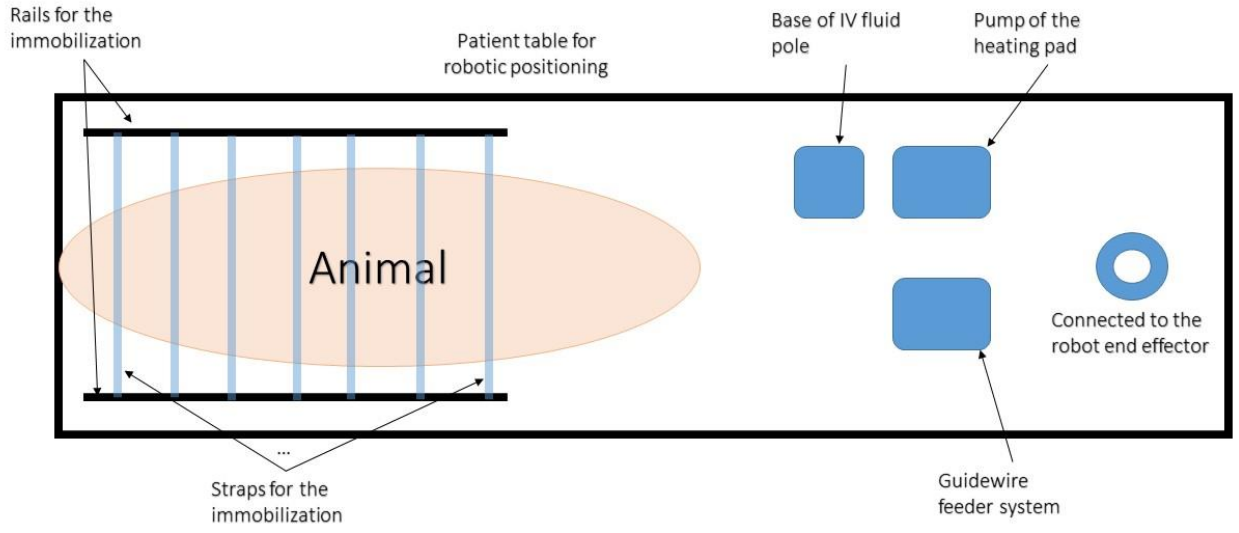

Figure 5.2 the schematic layout of different components on the patient table for *in vivo* experiment

5.2.1 Preparation of the robotic patient table

The robotic patient table required additional components to accommodate the requirements for *in vivo* experiment. Two rails of plastic were fixed on the overlay on either side of the animal for immobilization. Some straps were used for immobilizing the patient, and those were wrapped around the patient and the rails, and the space between the skin of the animal and the straps were filled with pillows. A heating pad for regulating the temperature of the animal was placed under the animal. The pump of the heating pad was fixed at the bottom of the overlay near the location of the feeder system. Also, a base was prepared for the pole of IV fluid on the overlay. So, throughout of robotic patient positioning, the pump of the heating pad, and the bag of the IV fluid were moving with the table. Figure 5.2 shows the layout of the table and different components on it for *in vivo* experiment.

5.3 Animal preparation

FFN experiments were planned to be done in the cerebral arteries of the animal. Vascular access was made in the femoral artery. A 6Fr catheter (Guider Softip XF, Boston Scientific) was then navigated into the CCA. After finishing the catheterization, the animal was put in a supine position on the table.

Before the beginning of the experiment, the grid of fiducial markers was fixed on the table as shown in Figure 5.3. Multi-modality markers are used for referencing the vascular trajectory on the patient table, calibration of the X-ray image, and vessel registration. Location of the markers was chosen in a way to be visible in Field of View (FOV) of MRI angiography of the neck and brain as well as FOV of the X-ray. After selective catheterization of the CCA, the animal was transferred to the MRI for angiography of the neck and the brain arteries. A Phase Contrast MRI imaging sequence was used for the angiography. The imaging parameters were TR=29ms TE=3.4ms, and the size of the voxel was 0.25×0.25×0.5mm. Figure 5.3 shows the animal on the patient table placed on the MRI table for the angiography and the flex antenna used for the imaging is placed on the animal. Some spacers were also fixed on the rails of the MRI table as the spacer between the MRI table and the robotic table. After MRI angiography, the table was mounted on the robot and was moved to the X-ray for imaging and registration.

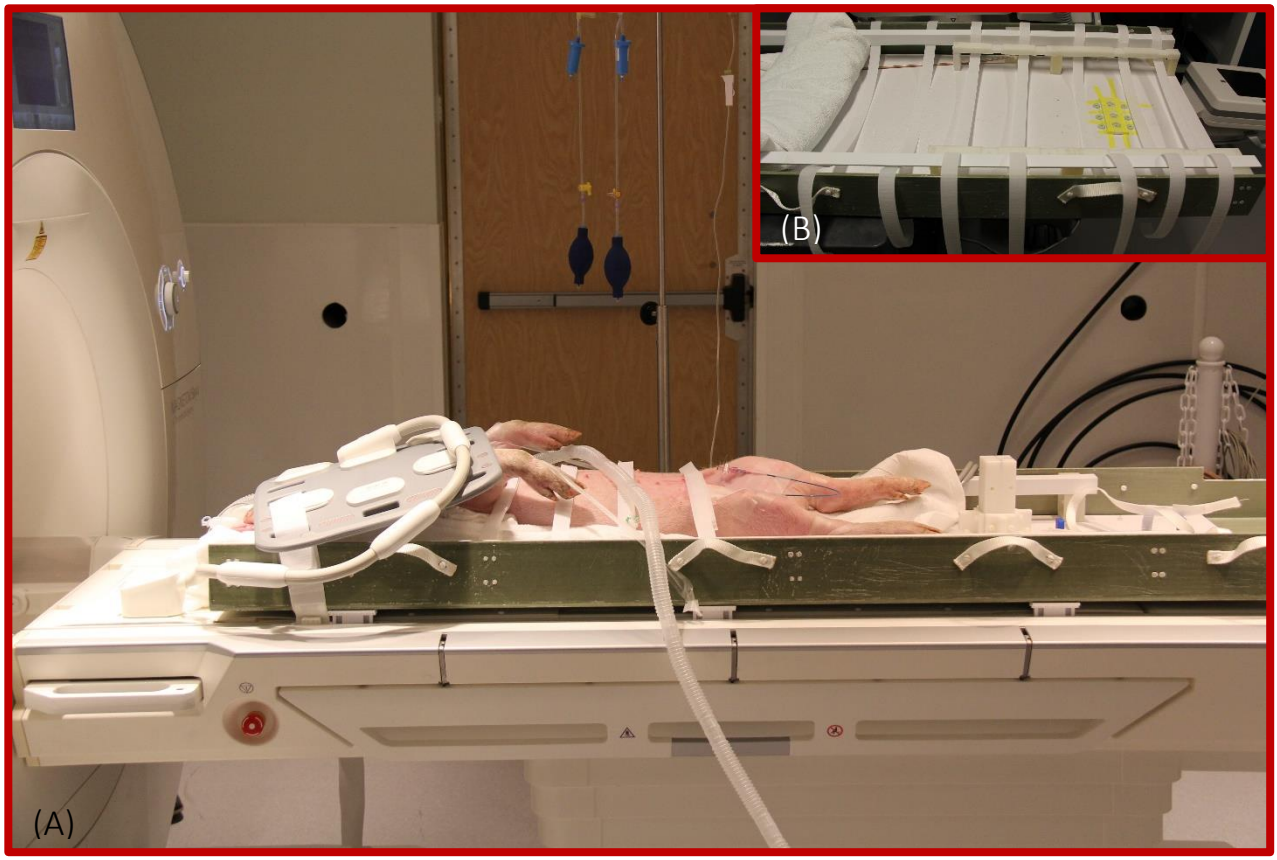

Figure 5.3 (A) a picture of the animal on the MRI table for the time of angiography and (B) shows the markers ad the straps of immobilization on the table.

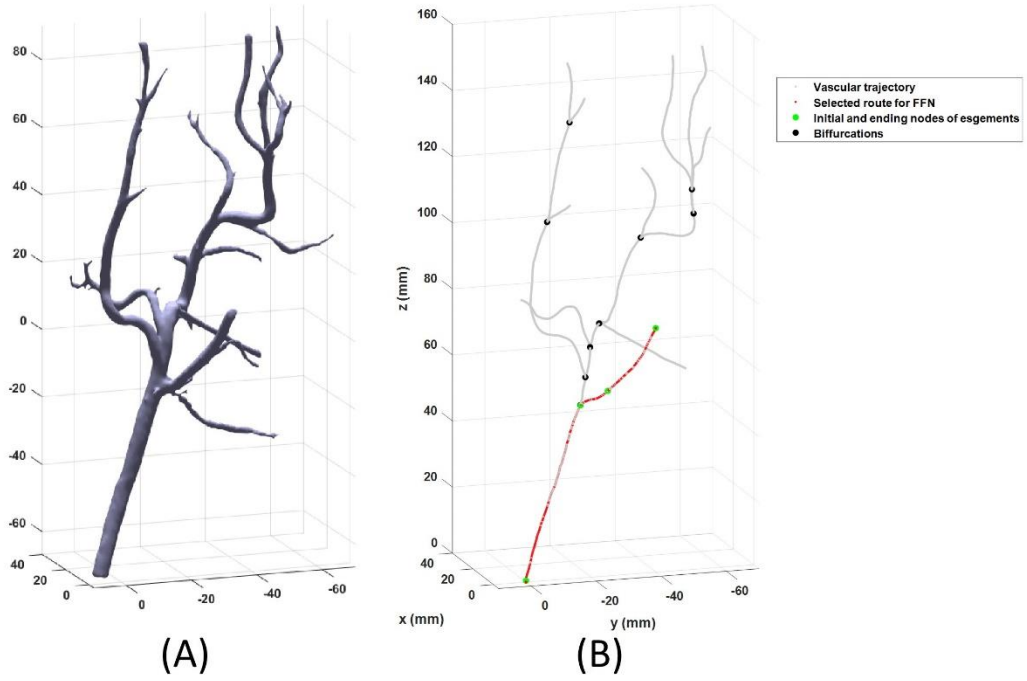

Figure 5.4 (A) 3D model of cerebral arteries of swine animal model and (B) the vascular trajectory of the vessels

5.4 Vascular model and trajectory

Segmentation of the arteries from the MRI image of the brain of the animals was done by use of the software of 3D slicer. Then, the 3D model was imported to the software of VMTK for the extraction of the vessel centerline. The trajectory of the arteries of the brain was then generated by the method presented in chapter 3 and was used for defining sequences of the FFN. Figure 5.4 shows the vascular model of the branches of CCA in swine. However, for *in vivo* experiments, the vascular model of the catheterized side of the brain for each of the *in vivo* experiments was incomplete and the vessels, either partially in animal model 1 or invisible in animal model 2. The vascular model presented in this figure is for the CCA of the brain of the animal model on the side that most of the arterial branches were visible in the MRI image.

5.5 *In vivo* animal model 1

Figure 5.5 shows an example of the animal on the patient table mounted on the robotic manipulator. For animal 1, FFN experiment was performed inside the left CCA. Due to the physiological feature

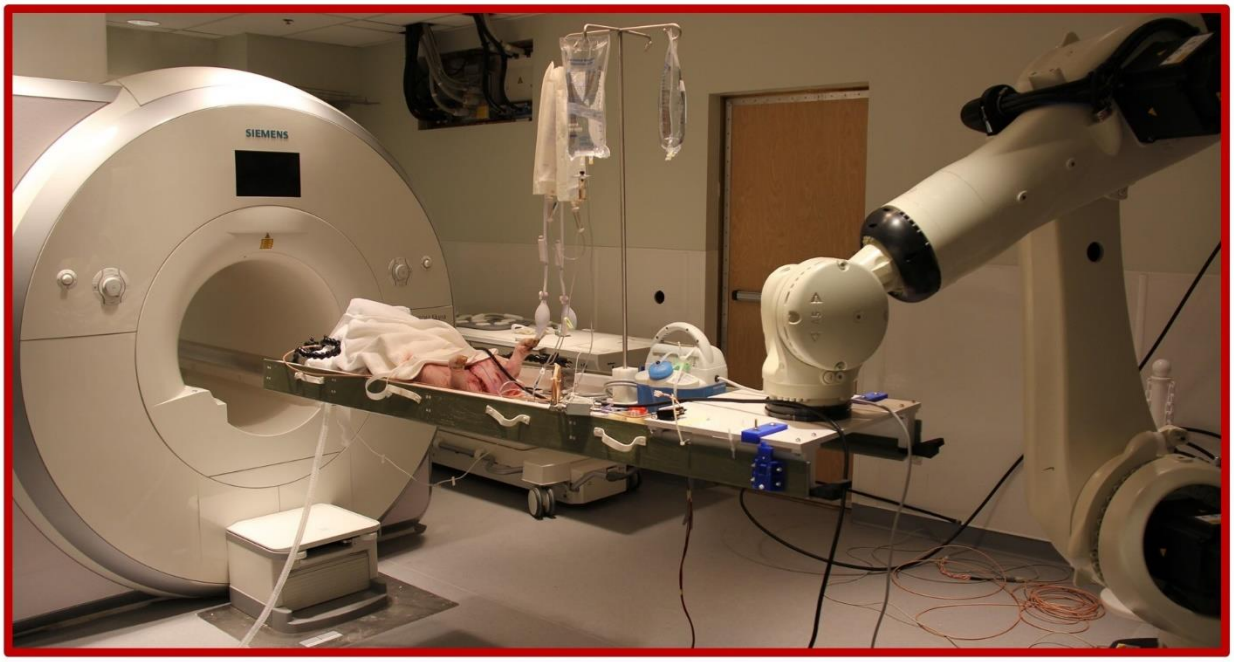

Figure 5.5 animal on the robotic patient table for FFN experiment

of Rete Mirabile in swine[159], the path of the external carotid artery (ECA) was chosen for the navigation. Also, this target required passing three branches to reach the target including the lingual artery and ascending pharyngeal artery (APA). The magnetic guidewire was fabricated by bonding a cylindrical neodymium permanent magnet with length and diameter of 1mm to the tip of the same type of the microguidewire used in *in vitro* experiments. The microguidewire was placed retrogradely inside a microcatheter (Fastracker 18, Boston Scientific) and the composition was inserted into the 6 Fr catheter priory placed inside the left CCA. The end of the microcatheter was fixed to the outlet of the guidewire feeder system, and IV fluid was administered into the microcatheter to reduce the friction between the microguidewire and the microcatheter. An X-ray image was taken at the beginning of the experiment, and the vascular trajectory was registered on it. The tip of the guidewire was placed inside the CCA at a location that corresponded to the initial point of the trajectory of the vessels deduced from the vascular registration. Figure 5.6 shows the vascular model and the trajectory of the animal model 1 prepared for the *in vivo* experiment.

The selected path for FFN experiment was segmented, and sequences of navigation were defined for each segment. Sequential positioning and insertion of the guidewire followed by a step of localization of the tip under X-ray were performed. For animal 1, the magnetic guidewire was

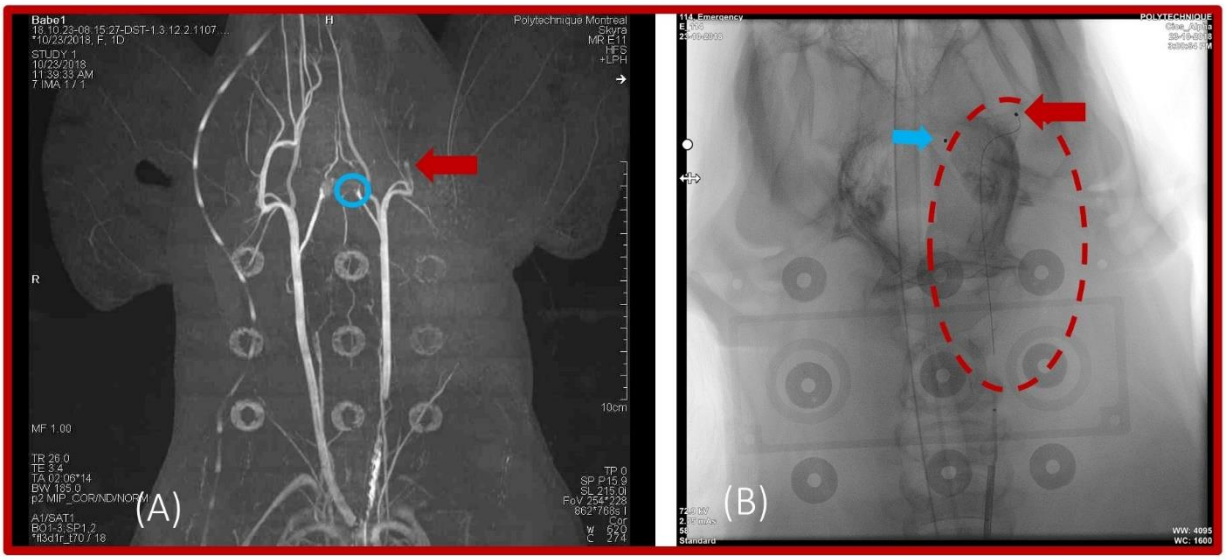

Figure 5.6 result of first *in vivo* experiment. Red arrows point to (A) the selected target of the experiment in MRI image and (B) the location of the tip at the end of the experiment. Blue arrow points to a magnet that brock from the tip of the guidewire during the experiment and was trapped inside Rete Mirabile of the animal shown in the blue circle in (A).

successfully navigated to the selected target for the navigation. Fig. 5 shows the X-ray image taken at the end of the experiment.

Feeding the guidewire was performed without problems of friction between the guidewire and the microcatheter. Administration of the IV fluid into the microcatheter and hydrophobic coating of the guidewire were the general factors for the facilitation of feeding the guidewire. Figure 5.7 shows a sequence of FFN executed during the *in vivo* experiment.

5.5.1 Vascular Registration for animal model 1

Also, the registration of the trajectory on the X-ray image was done *in vivo*, and its accuracy was evaluated by registration on a digital subtracted angiography (DSA) image shown in Figure 5.8. This registration was done before performing any FFN positioning with the spatial rotation of the animal. The figure shows the overlap between the registered vessel and the blood vessels through

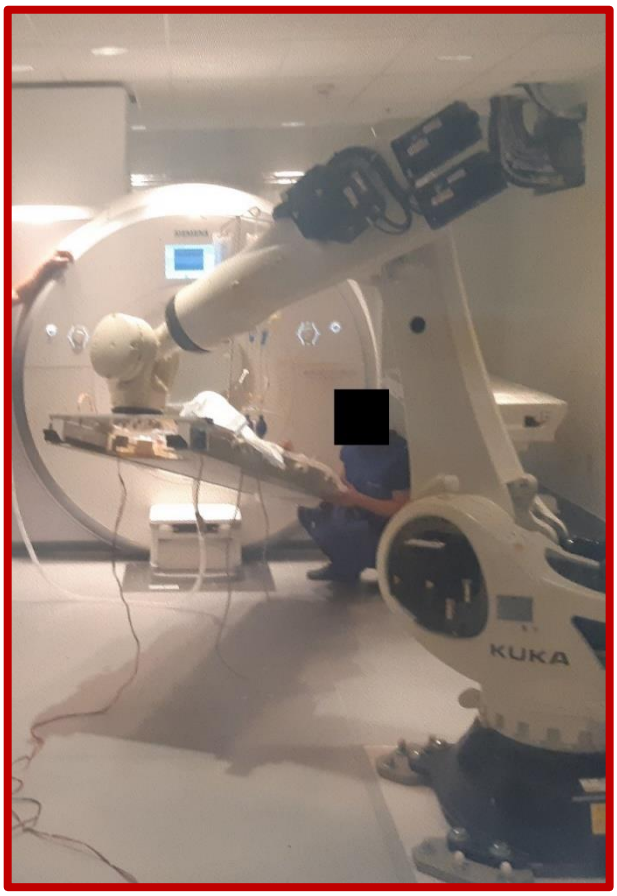

Figure 5.7 example of a FFN sequence of positioning of the animal

them the contrast media flew during taking the DSA image. However, a slight movement of the patient throughout of FFN can occur due to the spatial rotation of the patient that can corrupt the registration accuracy. Also, the method developed for the correction of the error in the registration was used for the result of the vascular registration for animal model 1. The error was applied to the result of the registration, and then the method was used to correct the error. Both binarization of the DSA image and the correction of the registration were performed successfully as shown in Figure 5.8.

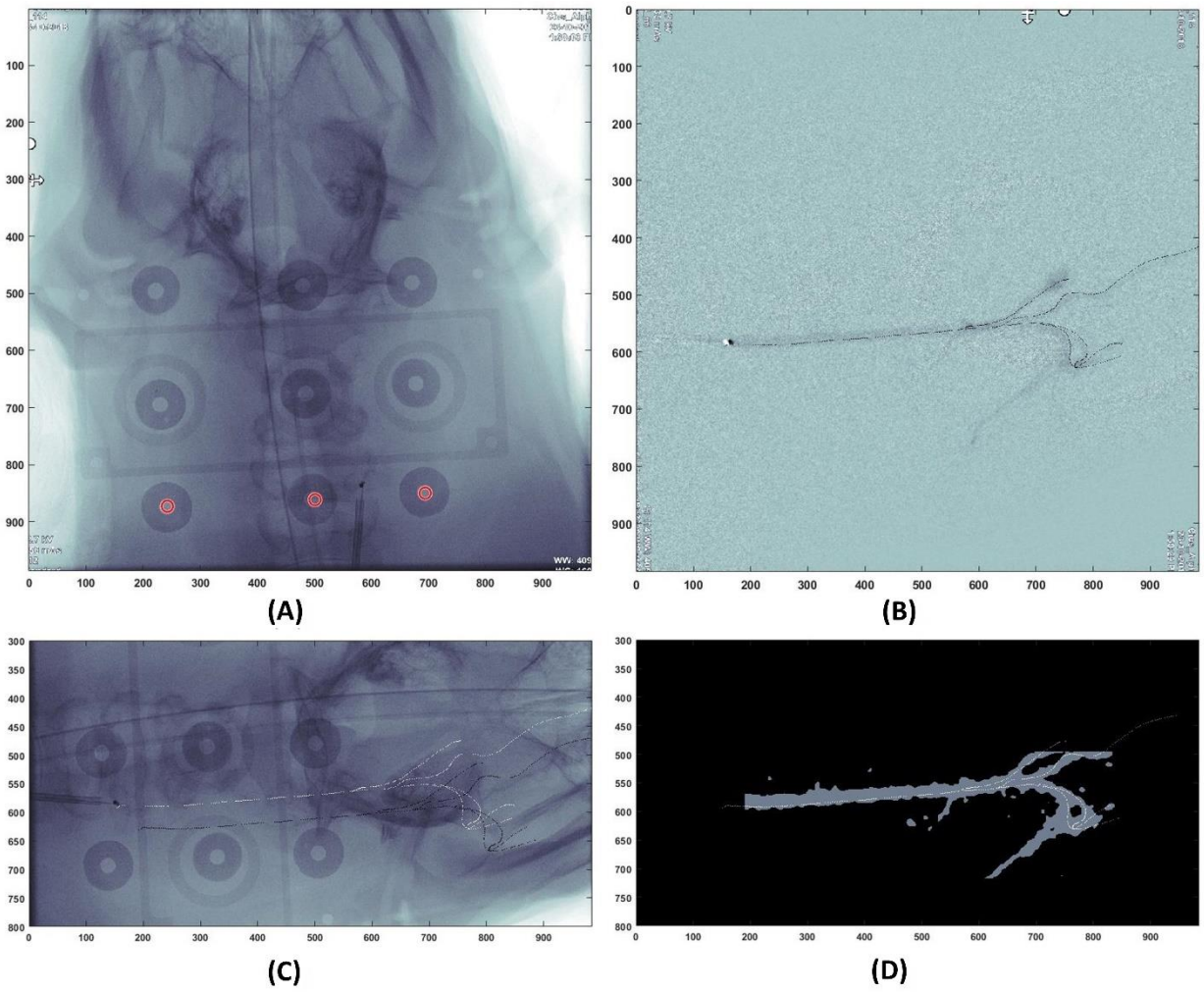

Figure 5.8 (A) shows the detection of the circular markers with Hough Transform. (B) shows the result of the registration of the vascular trajectory on a DSA image. (C) and (D) show the correction of the error in the registration of the vascular trajectory. White dashed lines in (A) are corrected of black dashed lines. (D) shows the binarized DSA image and the white dashed lines shows the vascular trajectory after applying the transformation to correct for the error (Details of the method is presented in chapter 3).

5.6 *In vivo* animal model 2

For animal model 2, the 6 Fr catheter was placed in the right CCA. The arteries of the catheterized side of the brain were invisible in MR angiography, as shown in Figure 5.9. Therefore, planning the trajectory, and vascular registration was not possible. In this experiment, the animal was in a

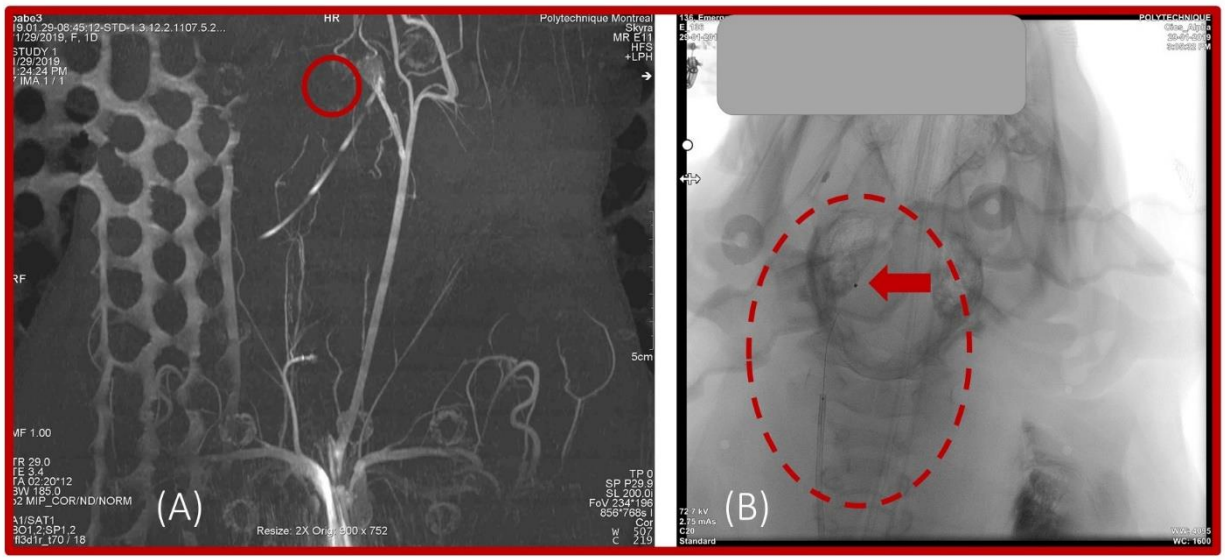

Figure 5.9 result of the second *in vivo* experiment on animal model 2. (The red arrow in X-ray image (B) shows the tip of the guidewire place at the selected target (red circle) in (A) MRI image. (A) shows that the arteries of the animal were not visible in the MRI image. The gray area in (B) is related to an instrument from a separate experiment.

supine pose with its head straight. So, the mirror of the arteries of the left side of the brain was used for defining the vascular trajectory. The vessel selected for the target of FFN was APA which is the first branch of the CCA. The diameter of APA was 2mm in the left side of the brain of the animal. The guidewire was prepared by bonding a tubular neodymium permanent magnet with ID of 0.5mm, OD of 1mm and the length of 1mm. The volume of the magnetic tip used for the second *in vivo* experiment was 25% less than the volume of the tip used in the first animal model. The navigation to the APA was done by placing the tip of the magnetic microguidewire less than 1cm before the bifurcation, moving the table to the position of the sequence of FFN and 2cm insertion of the guidewire. Navigation into APA was done successfully and with repeatability (twice in a row without failure). The strength and the gradient of the magnetic field used for the navigation was about 0.6T and more than 2T/m, respectively. Figure 5.9 shows the results of *in vivo* experiment on animal model 2.

5.6.1 Robustness in FFN

Results of investigation on the structure of the fringe field and its local uniformity were presented in chapter 3. Also, robustness in FFN against error in 6 DOF positioning of the patient was investigated *in vitro* by adding intentional error in the location of the vascular model on the table. In this *in vivo* experiment, an approximate of the location and the direction of APA was used to define FFN sequence. This result is another evidence to demonstrate the robustness in FFN against error in 6 DOF positioning of the patient in the fringe field which can be related to the structure of the fringe field and its local uniformity.

5.6.2 Impact of the magnetic gradient pulling force

The impact of the pulling force exerted on the tip for further insertion of the guidewire that was demonstrated *in vitro* was validated in animal model 2. It was done by pulling the guidewire back to the beginning of the APA from the position the tip was placed at the end of FFN experiment (the tip is still inside the APA) and trying to insert the guidewire under fluoroscopy while the animal is far away from the MRI scanner (B~0.5mT). As a result, insertion of the guidewire without using a pulling force on the tip was not possible, and the guidewire did not advance into APA. Figure 5.10 shows the result of the insertion of the guidewire without using FFN which led to crooking distal of the guidewire. It can be concluded that for a microguidewire with a magnetic tip, a pulling force is necessary to insert the guidewire in a vessel when insertion of the guidewire is not possible.

5.7 Autonomy in FFN

After MRI angiography of the cerebral arteries, the steps of 3D reconstruction of the vessels, extraction of the vessel centerlines, finding the relative location of the markers and the vascular model were done manually. Then, planning the vascular trajectory, calculation of FFN sequence and the generation of the trajectory for robotic positioning of the patient table were done automatically. After placement of the tip of the guidewire at an approximate location in the CCA of the animal corresponding to the beginning of the vascular segment, a task for automatic

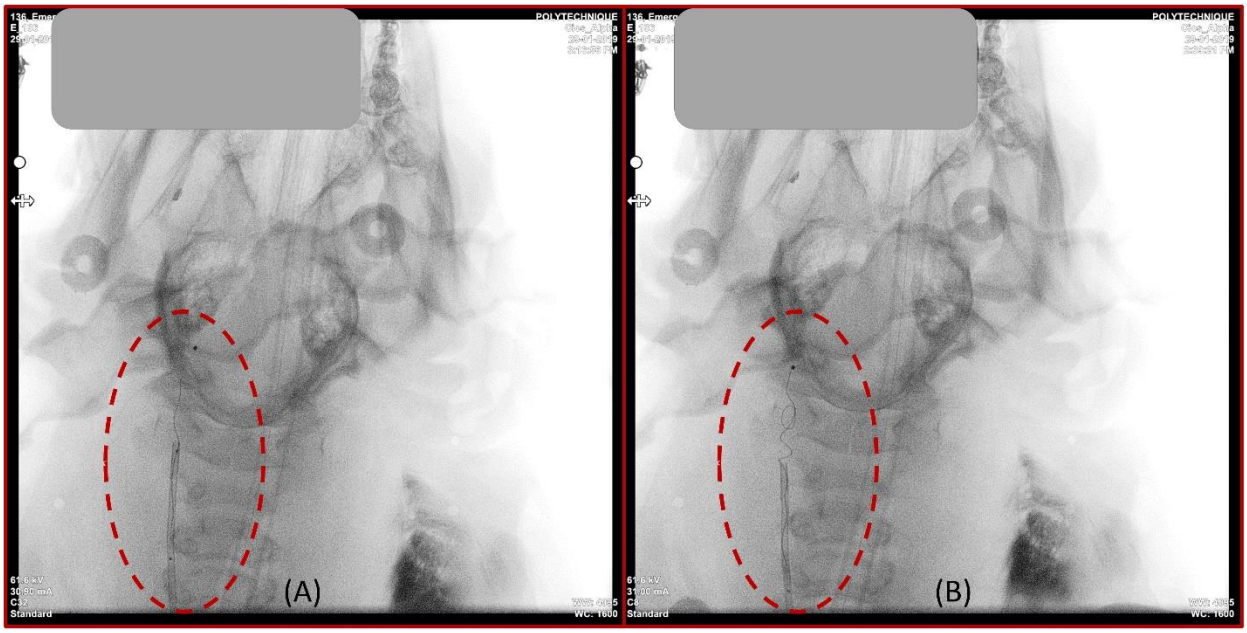

Figure 5.10 (A, and B) show examples that the insertion of the guidewire without applying a pulling force at the tip of the guidewire was not possible and the distal of the guidewire (shown in dashed ovals) crooked. The gray area in both images is related to an instrument used for another experiment.

positioning of the table, and feeding the guidewire was performed automatically (initiated by a person). It can be described as Task Autonomy[13] in the automatization of FFN.

5.8 Conclusion

Successful targeting of an artery with a diameter of about 2mm and proven effectiveness of the impact of the pulling force on the tip for the advancement of the tip of the guidewire inside the vascular system is so promising. Two examples of super-selective catheterization in human are: targeting the branches of the common hepatic artery and the cerebral arteries like the ophthalmic artery. For the former, the vessels have a range of diameter of between 4 to 6mm[160, 161]. The success of the *in vivo* experiment in this work and demonstration of the possibility of miniaturization of the size (volume) of the tip can help to reach to a conclusion that FFN can be an effective robotic approach to be considered for performing super-selective interventions.

CHAPTER 6 PROPOSITION FOR THE TIP OF THE GUIDEWIRE

An important part of a catheter-based procedure is the retrieval of the guidewire. Selection of the combination of the catheter and guidewire is done in the way that the lumen diameter of the catheter is larger than the diameter of the guidewire at its largest cross section. In FFN, a magnetic body is attached to the tip of the guidewire. In all the experiments in this work and the previous research that aimed to use magnetic actuation for the navigation of the microguidewires[162], the size of the tip was relatively larger than the tether. This problem is mentioned in previous research as an obstacle in the retrieval of the guidewire[69].

The most common magnetic body used for the tip of the guidewires is neodymium permanent magnet[163]. First, it is because this material has the highest magnetization among all the commercially available permanent magnets. Also, neodymium permanent magnets are a better solution for utilization with different systems for magnetic navigation. The reason is that the strength of the magnetic field available in those systems is not high enough (as presented in chapter 2) to bring the soft magnetic bodies to its magnetic saturation state. Use of the soft magnet materials is limited in the development of the magnetic guidewires.

A unique feature of FFN is the high strength of the magnetic field in comparison with other systems for magnetic navigation. The high strength of the magnetic field available in FFN can be used to saturate soft magnetic materials. Therefore, different configurations regarding the material and the shape of the magnetic tip can be investigated.

6.1 Concept of the spring

Retrieval of the guidewire is performed by pulling out the flexible guidewire through the lumen of a catheter along a curved path in the vascular system. For a guidewire with an implanted magnet at its tip which is generally larger than the tether, solid tip constraints the minimum size of the catheter that has to be used with the guidewire. While the possibility of the miniaturization of the permanent magnet tip is one solution, another solution investigated in this chapter is using a spring or a coil fabricated by winding a magnetic wire as the tip. Such a tip can be fabricated by the use of soft or hard magnetic materials. The higher magnetic moment is favorable in magnetic navigation as it increases the actuation, either the magnetic torque or the magnetic gradient force.

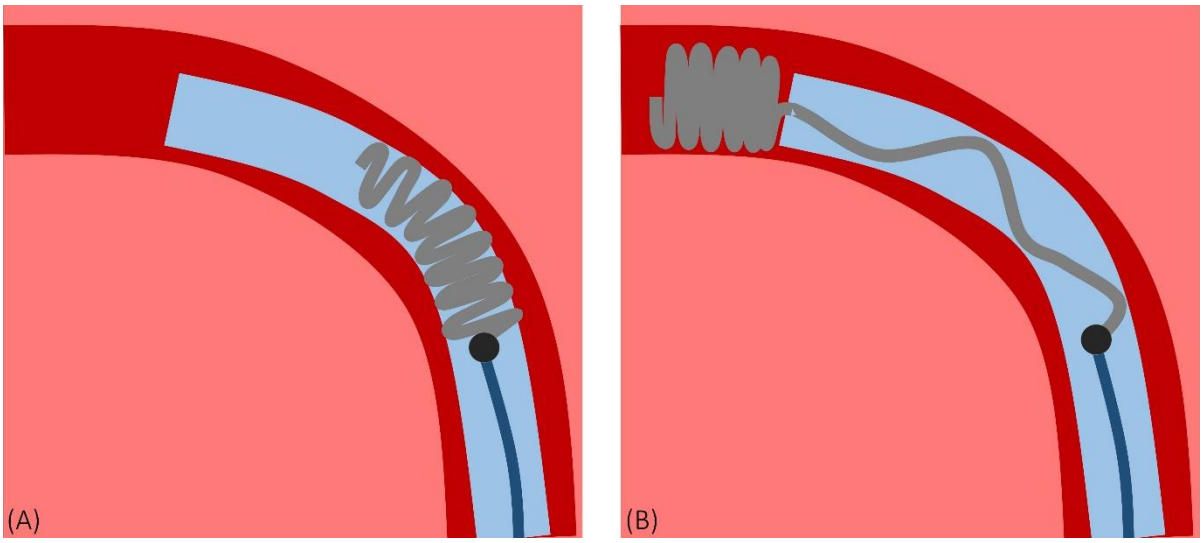

Figure 6.1 envisioned mechanism of deformation of the spring tip of the guidewire during retrieval through the catheter (A) bending inside the catheter and (B) unwinding.

Bringing a soft or hard magnetic material to its saturation state is depended on the strength of the external magnetic field. The high strength of the magnetic field available in FFN enables bringing the tip to its magnetic saturation state. Deformability is another characteristic to improve the functionality of the tip for the envisioned purpose. A spring or coil can bend and flex along its length or unwind. For the tip of the guidewire, the envisioned mechanisms for the deformation of the tip during the step of retrieving the guidewire are either the spring tip bend inside the catheter or unwind while the tether is being pulled out as shown in Figure 6.1. So, at the end of an FFN procedure that the tip of the guidewire has been placed at a desired location inside the vascular system, first, the catheter has to be inserted over the guidewire to the target. Then, retrieval of the guidewire can be done. Such a scenario leads to disposability of the guidewire as the shape of the coil tip changes at the end of an intervention.

6.2 Magnetic interaction

In the literature, no work that investigated how a spring behaves in an external magnetic field was found. So, characteristics of the springs in interaction with the magnetic field were empirically investigated in this work. Main geometrical configurations of spring are the length and diameter of the spring, the diameter of the wire and the pitch distance of the spring. Springs with different configurations were fabricated by use of the same type of the wire. The wire was grade 430 of

stainless steel which is a deformable material, and the diameter of the wire was 0.2mm. Winding the spring was done by use of different mandrels and fabricating the spring by turning the wire around it. The specific characteristic of the springs was as follow:

- Springs with pitch distance larger than the diameter of the wire and springs with pitch distance equal to the diameter of the wire (no gap between the turns of the wire)
- Spring with length to diameter ration of smaller than 1.5
- Springs with length to diameter ratio of larger than 2

The experiment was performed by observing the orientation of the spring relative to the direction of the external magnetic field lines at different strength of the magnetic field. Such a condition corresponds to the stable condition of the alignment of the magnetic moment of the spring with the external field (m.B=0). The range of the magnetic field varied between 0.1T to 3T and it was done by placing the samples at different locations along the center axis of the MRI between the isocenter of the MRI to a distance of more than 1m from the front face of the MRI outside of the scanner. Results of how the configuration of the spring impacts how it interacts with the magnetic field are as follow (and shown in Figure 6.1):

- For spring with the pitch distance of ~0 when the ratio of the length to the diameter of the coil is larger than 2, the spring magnetizes along its center axis at different zones in front of the MRI scanner.
- Once the pitch distance is larger than the diameter of the wire and there is a gap between the turns of the spring, the spring orients in the way that its axis aligns perpendicular to the direction of the external magnetic field.
- For springs with the ratio of the length to the diameter of less than 2, the spring's orientation in the magnetic field varies by changing the strength of the magnetic field. When the strength of the magnetic field is ~1T and higher, the spring aligns its center axis with the external field. By reducing the strength of the magnetic field, the spring rotates until its axis is perpendicular to the direction of the external magnetic field when the strength of the magnetic field is about 0.1T.

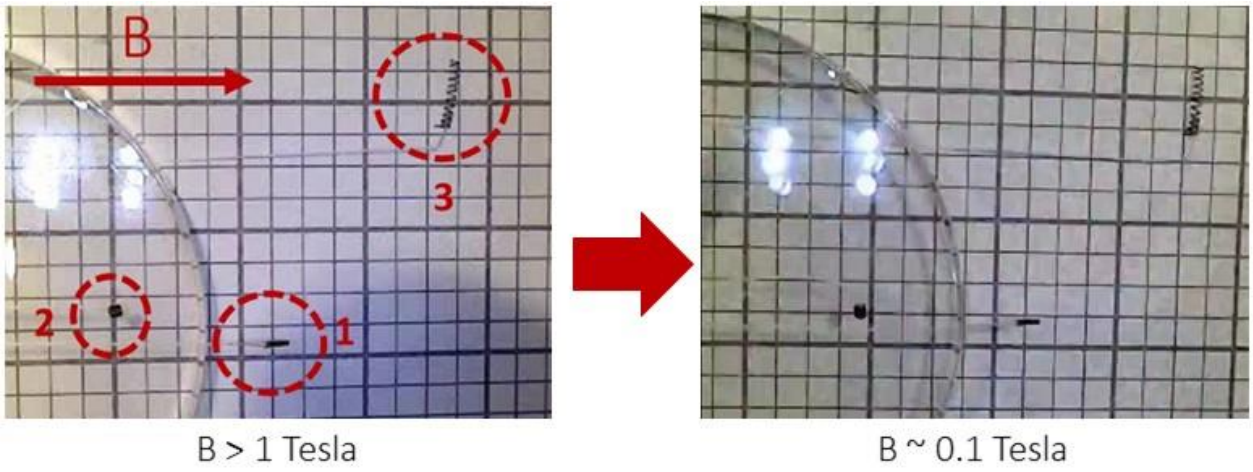

Figure 6.2 the interaction of spring with different configuration with the external magnetic field. (1) is tightly winded and L/D > 2. (2) is tightly winded and L/D ~ 1 and the orientation of the spring changes with the strength of the external magnetic field. (3) is spring with a gap between its turns and it is perpendicular to the direction of the external magnetic field.

A conclusion of these observations is that the appropriate configuration for spring to be used at the tip of the guidewire is a spring with length to diameter ratio of bigger than two which has no gap between its turns. It is because the magnetization of the tip is stable and it is the simplest model for the calculation of the direction of the magnetic gradient force. Same as a permanent magnet, a spring with described configuration can be assumed to have a constant magnetization direction.

By selecting the proper configuration of the spring for the tip of the guidewire, its magnetic saturation characteristic was investigated by the method of Vibratory Sample Measurement (VSM). The VSM test (shown in Appendix F) showed that the coil reaches 95% of its magnetic saturation state when the strength of the external magnetic field is around 0.5T, which is less than the maximum available strength of the magnetic field in FFN. The diagram of the magnetization of two samples with the weights of 3.5mg and 5mg and the density of 7.8cm/m^3 is presented in figure X. The samples had the length to diameter ratio of ~3 and ~5 and the same material and wire were used for the fabrication of the springs.

6.3 FFN Experiments

The magnetic guidewire was prepared by bonding a spring to the tip of the microguidewire with an epoxy resin compound. The spring was fabricated by winding a deformable wire of Stainless

Steel 430 with the diameter of 0.2mm. The spring that was fabricated for the tip of the guidewire had the length of ~2mm and the diameter of ~0.7mm. *In vitro*, FFN experiments were performed by use of the same map of the magnetic gradient force that was calculated for a permanent magnet tip. FFN experiments were performed to navigate the guidewire to targets 1, 3, 4, 5, and 6 in 3D vascular model that was used in *in vitro* experiments. Figure 6.3 shows the results of the navigation of the guidewire to the different targets. However, the possibility of retrieving the guidewire through the catheter is not investigated as the material used for bonding the tip to the tether solidified the tip.

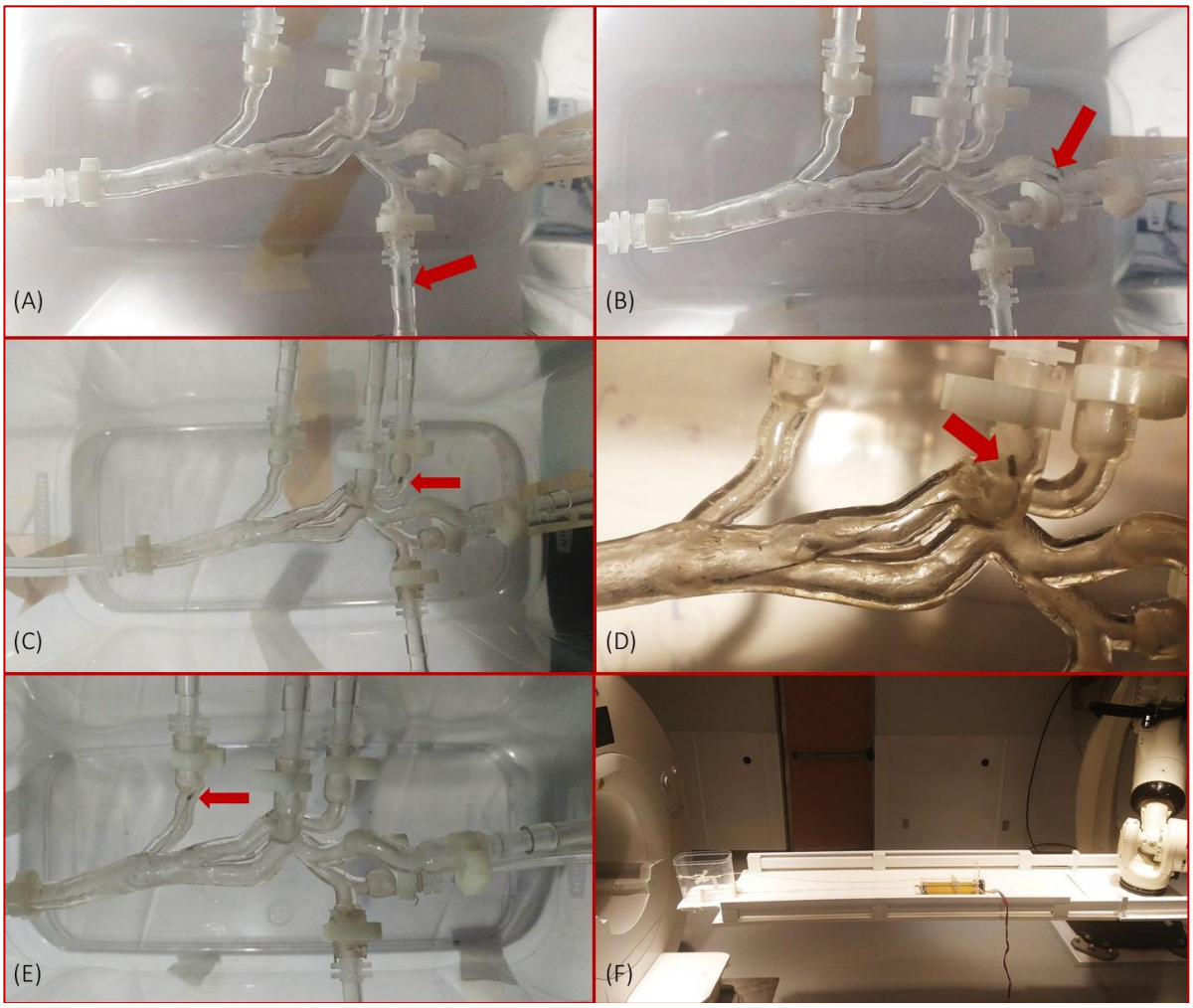

Figure 6.3 (A – E) shows results of *in vitro* FFN experiment with a spring at the tip of the guidewire and arrows are pointing to the location of the tip and (F) is the setup of the experiments

CHAPTER 7 GENERAL DISCUSSION

In this work, it is demonstrated that the idea of using a strong pulling force exerted on the tip of a soft guidewire is useful and effective for steering and insertion of the guidewire. The composition of the magnetic torque and the magnetic gradient force in FFN can steer and pull the guidewire inside the blood vessels. The strong magnetic actuation in FFN also is a mean to miniaturize the size of the tip of the guidewire. A valuable result of it is the possibility of targeting the narrower vessels in the vascular system.

- **Autonomy:** In robotization of the vascular catheterization, increasing the autonomy of the procedure is valuable. Reducing the impact of requiring high experience from the practitioner can help to perform more procedures while developing more methods of the treatment based on vascular access. Steering and navigation of a guidewire with FFN can be performed with task autonomy. Task autonomy is the level of the autonomy in which a human can initiate a robotic medical procedure and supervise its execution while the robot performs the task[13]. In our *in vivo* experiment after placing the tip of the guidewire at a certain location inside the CCA, task autonomy was achieved by execution of a sequence of robotic patient positioning for FFN which was calculated from the vascular model and the map of the magnetic field to navigate the guidewire along a certain path. This whole step can be considered as a task autonomy. Current technologies for robotic catheterization in clinical use has a lower level of autonomy as a human continuously controls the instrument from a dedicated workstation[71, 74, 75, 77, 136].
- **Robustness:** It is shown that FFN is robust against limited error in the robotic positioning of the patient inside the external magnetic field. Structure of the fringe field and so the curvature of the lines of the magnetic field is the mean of explaining this robustness. The relatively large size to the MRI scanner to the size of the human body provides this robustness.
- **Recumbent position of the patient on the robotic table:** In FFN, the way the patient lays on the robotic table plays an important role as it changes the direction of the vessels. Different recumbent positions change the direction of the vessels on the patient table. It affects the efficiency of the FFN regarding the strength of the magnetic actuation as the magnetic force in FFN is mainly toward the MRI bore while the pitch and roll rotation of

the table has to be limited. Common endovascular interventions in the abdomen area are performed in different branches of the aorta, and super selective catheterization aims to place the catheter deeper inside the vascular system. For each specific target in the abdomen, the recumbent position of the patient influences the efficiency of FFN. For instance, supine or prone positions can be the best position for navigation into the branches of renal arteries with FFN. For navigation into the branches of the celiac trunk or the superior mesenteric artery, the lateral recumbent positions could be preferred. For intervention inside the brain, turning and bending the neck also influences the efficiency of FFN. For targeting each section of the brain, one particular position of the neck and head may yield the highest efficiency. For intervention inside the legs, the proper positioning of the patient could require putting the head near the end effector while the legs are laying toward the other end of the table. To avoid underrepresenting the potential of FFN for specific endovascular intervention, case-specific studies to find the proper body position of the patient on the table for each intervention is a recommendation for the future work.

- **Custom sizing of the guidewire device:** From these values and the result of the *in vivo* and *in vitro* experiments, one conclusion can be the possibility of using FFN for targeting branches of these arteries down to few folds. As FFN can perform an intervention with task autonomy, performing super-selective interventions would be beneficial and possible with FFN to perform local diagnosis and treatments.
- **Map of the magnetic gradient force:** To calculate the direction of the magnetic gradient force, the orientation of the tip of the guidewire inside the body has to be known. The stiffness of the tether, the contact forces with the vessel walls and blood flow speed can have some impacts on the orientation of the tip inside the blood vessels. In calculating the map of the magnetic gradient force, the direction of the tip of the guidewire is assumed to align with the external magnetic field. This assumption is made based on (1) we used guidewires with floppy distal to reduce resistance against bending and (2) FFN use strong magnetic field (larger than 0.5T). These assumptions were validated throughout our experiments for the configuration of the guidewire that was prepared for the experiments.
- **Time of a procedure of FFN:** An important factor regarding FFN is the required time to perform a procedure. A procedure of FFN begins with MR imaging which may take up to

half an hour. Then, 3D reconstruction, extraction of the centerline, planning the trajectory and the sequences are the steps that has to be performed which may take about half an hour, which it makes up 1 hour. Then the FFN can be executed which every sequence of FFN may take about 3 to 4 minutes to move the patient to the location of sequence of FFN, feed the guidewire and return the patient table back to the HOME position. Each sequence of robotic positioning of the patient for navigation was taking about 1 to 2 minutes to transport the patient to the target position from a general position. This transportation was executed with limited velocity and acceleration for the smooth displacement of the patient table. FFN is proposed for performing selective steering of the guidewire at bifurcations and to insert the guidewire in narrow blood vessels by applying a pulling force on the tip. A way to optimize the time of an intervention is to limit performing FFN sequences to challenging parts in the vascular system that the magnetic actuation from THE FRINGE FIELD is essential. For example, in *in vivo* experiment on animal model 2, the FFN was only used at the bifurcation that the APA artery branched from the CCA. At this section, using the actuation at the tip of the guidewire was essential for the success of the navigation. However, placement of the tip of the guidewire at a location near and before the bifurcation was performed manually under the X-ray imaging. Such a scenario improved the efficiency of the experiment regarding the required time to perform successful navigation. This scenario is extendable to the case of navigation through a multibifurcation path.

- **Trajectory planning for robotic patient positioning:** The strategy for robotic positioning of the patient is a key element in the autonomy of FFN. Safety is the basic requirement for any strategy. Definition of a sub-space as the safe working zone for FFN allows protecting the robot from entering the zones where the strength of the magnetic field and the magnetic gradient force can be problematic. The trajectory of the movement of the robot is critical regarding this criterion. This problem was solved in this work by defining different zones around the MRI inside the working space of the robot and analyzing the required movements to propose safe trajectories of movement that are a composition of basic movements of rotation along the major axes and orthogonal translations. While a more advanced trajectory planning strategy that moves the table along a smoother path may reduce this time, still the physical transportation of the patient table requires a certain time

to execute a sequence. In my view, an improvement in the motion planning strategy has a low priority as the implemented strategy in this work is proven to be effective and safe to perform the positioning in a reasonable amount of time.

- **Fabrication of the guidewire with a spring tip:** The possibility of using a deformable magnetic tip enhances the potential of the catheter-based procedure by facilitating the step of guidewire retrieval. Here, the concept of a microguidewire with a spring at its tip is proposed and *in vitro* navigation of such a guidewire in a vascular model is achieved. Among all the systems developed for magnetic navigation, FFN features a unique high strength of the magnetic field that brings such a tip to saturation level. One remaining aspect to be investigated is the method of bonding the coil to the tether to enable retrieval of the guidewire. Dissimilar welding followed by heat treatment can be a method of fabrication to attach NiTi wire as the tether to a coil made of stainless steel[164]. Optimization of the diameter of the wire and dimensions of the coil is required for the success of retrieval.

- **Pulling the tip:** The microguidewire is in contact with the vessel wall and under tension. Pulling the tip of the guidewire leads to slippery friction which may be a cause of complication in FFN. It is similar to the engineering static problem of tension in the ropes on a pulley wheel. One way to approach this problem is to consider that enough actuation is not essentially the maximum available. While the fringe field of MRI scanners provides a wide range of the amplitude for the magnetic actuation, this problem may be tackled by using the zone in FFN where the actuation is strong enough to enable navigation while it may not be the maximum available. Also, the microcatheter used for the procedure can be inserted after each sequence of FFN so the slippery friction occur on the surface of the inside of catheter while hydrophobic coating of the guidewire reduces the resistive force.

- **Error in the accuracy of the trajectory:** The trajectory of the vasculatures is generated by using the angiography image taken at the beginning of an intervention. Calculating the sequences of FFN are done by using the trajectory. The movement of the patient on the table can violate the accuracy of the trajectory and induce error. It can be eliminated by proper immobilization of the body. However, immobilization of the patient fixes the external surface of the body while the internal organ is deformable. Respiration can deform

the internal organs, especially in the abdomen. Gating the respiration for the time of feeding the guidewire device during an FFN procedure can be considered as a solution for this issue. However, gravity is another cause of deformation of the internal organs when the 6 DOF positioning of the patient is performed. It is a complex problem in FFN. However, the large size of the MRI scanners and the local uniformity in the field investigated in section 3.3.3 and the basic in vitro experiments performed in chapter 4 and the success of the navigation of the guidewire in vivo on the animal model 2 and presented in section 5.6 are evidences of robustness in FFN against error in the positioning of the patient which can be extended to the error in the accuracy of the trajectory of the vessels.

CHAPTER 8 CONCLUSION AND RECOMMENDATIONS

The stray magnetic field around the MRI scanner and generated by the superconducting coils has been used for steering and insertion of a guidewire inside the vessels. By applying a pulling force and torque on the tip, steering and insertion of the costume guidewire with a magnet at its tip are achieved. It has been shown that the high strength of the magnetic field, as well as the magnitude of the gradient of the magnetic field, allows reducing the size of the magnetic tip to a sub-millimeter body. This outcome allows targeting narrow vessels in an endovascular intervention in a robotic manner and independent of the experience of the interventionist. In addition, it is shown that FFN which relies on the 6 DOF patient positioning is robust against the error in the positioning of the patient in the MRI stray field. Successful implementation of the FFN protocol for robotic catheterization in an *in vivo* experiment and navigation of the guidewire into a narrow blood vessel (2mm diameter) demonstrates the potential of FFN to be considered as a novel tool for performing catheter-base procedures. Also, FFN as a robotic approach brings task autonomy to performing endovascular catheterization.

8.1 Future Work

A major recommendation for future works on the FFN is the case-specific studies on the application of FFN for different types of interventions at different locations inside the body. At the first level, the case-specific studies have to be divided into specific projects that investigate the potential of FFN for the navigation of the guidewire in different organs. The intervention in different abdominal branches of the aorta or the neurovascular intervention is different specific cases of the investigation. Setting the goal of the depth of targeting in the vascular system is a fundamental requirement of the study. For each group, two different parameters have to be investigated. First, the recumbent position of the patient on the table that leads to exploiting the stronger magnetic actuation for the navigation. The requirement of this study is (1) the vascular anatomy of different organs, and (2) the range of the height of the patient as it defines the approximate location of the organ on the robotic table. Result of this study will propose the proper recumbent position of the table for each type of the intervention and the range of the strength of the magnetic field and the magnitude of the gradient of the magnetic field that can be used for the intervention. The goal of this step is finding the recumbent position that allows exploiting stronger actuation. Next step is

designing the custom guidewire regarding the size of the magnetic tip. Requirements for this step are, (1) the range of the diameter of the blood vessels and the common gauge of the catheter that can be inserted in the blood vessels, and (2) the result achieved from the previous study to design the tip for the costume guidewire. At this level, choosing the type of the magnetic tip of the guidewire between a simple permanent magnet or a deformable tip (the coil type proposed in chapter 6) has to be done. Variables to be considered for this choice are the size of the vessels and so the size of the catheter that can be used. In this level, if the use of the more complicated guidewire with a deformable magnetic tip is essential, the step of fabricating the costume guidewire with the coil for its tip has to be followed.

REFERENCES

1. Blakemore, C., S. Jennett, and S. Jennett, *The Oxford companion to the body*. Vol. 7. 2001: Oxford University Press Oxford.
2. Schneider, P., *Endovascular skills: guidewire and catheter skills for endovascular surgery*. 2008: CRC Press.
3. Owens, C.D. and Y. Yeghiazarians, *Handbook of endovascular peripheral interventions*. 2011: Springer Science & Business Media.
4. Bonatti, J., et al., *Robotic technology in cardiovascular medicine.* Nature Reviews Cardiology, 2014. **11**(5): p. 266.
5. Goodney, P.P., et al., *National trends in lower extremity bypass surgery, endovascular interventions, and major amputations.* 2009. **50**(1): p. 54-60.
6. Connors III, J.J., et al., *Training, Competency, and Credentialing Standards for Diagnostic Cervicocerebral Angiography, Carotid Stenting, and Cerebrovascular Intervention: A Joint Statement from the American Academy of Neurology 1, American Association of Neurological Surgeons 1, American Society of Interventional and Therapeutic Radiology 1, American Society of Neuroradiology 1, Congress of Neurological Surgeons 1, AANS/CNS Cerebrovascular Section 1, and Society of Interventional Radiology 1 2.* 2005. **234**(1): p. 26-34.
7. Ramcharitar, S., et al., *Technology insight: magnetic navigation in coronary interventions.* Nature Reviews Cardiology, 2008. **5**(3): p. 148.
8. Kerzner, R., et al., *Radiofrequency ablation of atrioventricular nodal reentrant tachycardia using a novel magnetic guidance system compared with a conventional approach.* Heart Rhythm, 2006. **3**(3): p. 261-267.
9. Veltri, A., et al., *Radiofrequency thermal ablation (RFA) after transarterial chemoembolization (TACE) as a combined therapy for unresectable non-early hepatocellular carcinoma (HCC).* 2006. **16**(3): p. 661-669.
10. Cunningham, D., et al., *Perioperative chemotherapy versus surgery alone for resectable gastroesophageal cancer*. 2006. **355**(1): p. 11-20.
11. Hirsch, A.T., et al., *ACC/AHA 2005 practice guidelines for the management of patients with peripheral arterial disease (lower extremity, renal, mesenteric, and abdominal aortic) a collaborative report from the American Association for Vascular Surgery/Society for Vascular Surgery,* Society for Cardiovascular Angiography and Interventions, Society for Vascular Medicine and Biology, Society of Interventional Radiology, and the ACC/AHA Task Force on Practice Guidelines (writing committee to develop guidelines for the management of patients with peripheral arterial disease): endorsed by the American Association of Cardiovascular and Pulmonary Rehabilitation; National Heart, Lung, and Blood Institute; Society for Vascular Nursing; TransAtlantic Inter-Society Consensus; and Vascular Disease Foundation.* 2006. **113**(11): p. e463-e654.
12. Sundt, J.T., et al. *Bypass surgery for vascular disease of the carotid system*. in *Mayo Clinic Proceedings*. 1976.
13. Yang, G.-Z., et al., *Medical robotics—Regulatory, ethical, and legal considerations for increasing levels of autonomy.* Sci. Robot, 2017. **2**(4): p. 8638.
14. Ahlering, T.E., et al., *Successful transfer of open surgical skills to a laparoscopic environment using a robotic interface: initial experience with laparoscopic radical prostatectomy.* 2003. **170**(5): p. 1738-1741.

15. Livraghi, T.J.J.o.h.-b.-p.s., *Radiofrequency ablation, PEIT, and TACE for hepatocellular carcinoma.* 2003. **10**(1): p. 67-76.
16. Lencioni, R., et al., *Radio-frequency thermal ablation of liver metastases with a cooled-tip electrode needle: results of a pilot clinical trial.* 1998. **8**(7): p. 1205-1211.
17. Zlotta, A., et al., *Percutaneous transperineal radiofrequency ablation of prostate tumour: safety, feasibility and pathological effects on human prostate cancer.* 1998. **81**(2): p. 265-275.
18. Girelli, R., et al., *Feasibility and safety of radiofrequency ablation for locally advanced pancreatic cancer.* 2010. **97**(2): p. 220-225.
19. Favaro, A., et al. *Steerable needle DBS path planning safeguards deep nuclei and white matter tracts*. in *Joint Workshop on New Technologies for Computer/Robot Assisted Surgery (CRAS)*. 2018. GBR.
20. D'amico, A.V., et al., *Biochemical outcome after radical prostatectomy, external beam radiation therapy, or interstitial radiation therapy for clinically localized prostate cancer.* 1998. **280**(11): p. 969-974.
21. Hynynen, K., et al., *MR imaging-guided focused ultrasound surgery of fibroadenomas in the breast: a feasibility study.* 2001. **219**(1): p. 176-185.
22. Serruys, P.W., et al., *Percutaneous coronary intervention versus coronary-artery bypass grafting for severe coronary artery disease.* 2009. **360**(10): p. 961-972.
23. Sergio, A., et al., *Transcatheter arterial chemoembolization (TACE) in hepatocellular carcinoma (HCC): the role of angiogenesis and invasiveness.* 2008. **103**(4): p. 914.
24. Fagogenis, G., et al., *Autonomous robotic intracardiac catheter navigation using haptic vision.* 2019. **4**(29): p. eaaw1977.
25. Jang, I.-K., et al., *Visualization of coronary atherosclerotic plaques in patients using optical coherence tomography: comparison with intravascular ultrasound.* 2002. **39**(4): p. 604-609.
26. Fischman, D.L., et al., *A randomized comparison of coronary-stent placement and balloon angioplasty in the treatment of coronary artery disease.* 1994. **331**(8): p. 496-501.
27. Theron, J.G., et al., *Carotid artery stenosis: treatment with protected balloon angioplasty and stent placement.* 1996. **201**(3): p. 627-636.
28. White, C.J., et al., *Renal artery stent placement: utility in lesions difficult to treat with balloon angioplasty.* 1997. **30**(6): p. 1445-1450.
29. Sigwart, U., et al., *Intravascular stents to prevent occlusion and re-stenosis after transluminal angioplasty.* 1987. **316**(12): p. 701-706.
30. McFadden, E.P., et al., *Late thrombosis in drug-eluting coronary stents after discontinuation of antiplatelet therapy.* 2004. **364**(9444): p. 1519-1521.
31. Giustino, G., et al., *Duration of dual antiplatelet therapy after drug-eluting stent implantation: a systematic review and meta-analysis of randomized controlled trials.* 2015. **65**(13): p. 1298-1310.
32. Marrouche, N.F., et al., *Phased-array intracardiac echocardiography monitoring during pulmonary vein isolation in patients with atrial fibrillation: impact on outcome and complications.* 2003. **107**(21): p. 2710-2716.
33. Peters, P.J. and S.J.J.o.t.A.S.o.E. Reinhardt, *The echocardiographic evaluation of intracardiac masses: a review.* 2006. **19**(2): p. 230-240.

34. Mangrum, J.M., et al., *Intracardiac echocardiography-guided, anatomically based radiofrequency ablation of focal atrial fibrillation originating from pulmonary veins.* 2002. **39**(12): p. 1964-1972.
35. Hannan, E.L., et al., *Adult open heart surgery in New York State: an analysis of risk factors and hospital mortality rates.* 1990. **264**(21): p. 2768-2774.
36. DeVita, V.T. and E.J.C.r. Chu, *A history of cancer chemotherapy.* 2008. **68**(21): p. 8643-8653.
37. Geschwind, J.-F.H., et al., *Transcatheter arterial chemoembolization of liver tumors: effects of embolization protocol on injectable volume of chemotherapy and subsequent arterial patency.* 2003. **26**(2): p. 111-117.
38. Martel, S. *Exploiting electromagnetic fields to enhance the delivery of therapeutics to tumors*. in *2015 9th European Conference on Antennas and Propagation (EuCAP)*. 2015. IEEE.
39. Martel, S., *Microrobotics in the vascular network: present status and next challenges.* Journal of Micro-Bio Robotics, 2013. **8**(1): p. 41-52.
40. Martel, S., *Presenting a New Paradigm in Cancer Therapy: Delivering therapeutic agents using navigable microcarriers.* IEEE pulse, 2014. **5**(3): p. 48-55.
41. Martel, S., *Targeting active cancer cells with smart bullets.* Therapeutic delivery, 2017. **8**(5): p. 301-312.
42. Nosrati, Z., et al., *Development of a coflowing device for the size-controlled preparation of magnetic-polymeric microspheres as embolization agents in magnetic resonance navigation technology.* 2018. **4**(3): p. 1092-1102.
43. Mehra, R.J.J.o.e., *Global public health problem of sudden cardiac death.* 2007. **40**(6): p. S118-S122.
44. Adatia, I., S.S. Kothari, and J.A.J.C. Feinstein, *Pulmonary hypertension associated with congenital heart disease: pulmonary vascular disease: the global perspective.* 2010. **137**(6): p. 52S-61S.
45. Shi, Y., et al., *Translational stroke research on blood-brain barrier damage: challenges, perspectives, and goals*. 2016, Springer.
46. Ferlay, J., et al., *Cancer incidence and mortality worldwide: sources, methods and major patterns in GLOBOCAN 2012.* 2015. **136**(5): p. E359-E386.
47. Bray, F., et al., *Global cancer statistics 2018: GLOBOCAN estimates of incidence and mortality worldwide for 36 cancers in 185 countries.* 2018. **68**(6): p. 394-424.
48. Nelson, B.J., I.K. Kaliakatsos, and J.J. Abbott, *Microrobots for minimally invasive medicine.* Annual review of biomedical engineering, 2010. **12**: p. 55-85.
49. Sitti, M., *Miniature soft robots—road to the clinic.* Nature Reviews Materials, 2018. **3**(6): p. 74.
50. Hu, W., et al., *Small-scale soft-bodied robot with multimodal locomotion.* Nature, 2018. **554**(7690): p. 81.
51. Huang, H.-W., et al., *Adaptive locomotion of artificial microswimmers.* Science advances, 2019. **5**(1): p. eaau1532.
52. Martel, S., *Beyond imaging: Macro-and microscale medical robots actuated by clinical MRI scanners.* Science Robotics, 2017. **2**(3): p. eaam8119.
53. Sitti, M., et al., *Biomedical Applications of Untethered Mobile Milli/Microrobots.* Proceedings of the IEEE, 2015. **103**(2): p. 205-224.

54. Li, J., et al., *Micro/nanorobots for biomedicine: Delivery, surgery, sensing, and detoxification.* Sci. Robot, 2017. **2**(4).
55. Yan, X., et al., *Multifunctional biohybrid magnetite microrobots for imaging-guided therapy.* Science Robotics, 2017. **2**(12): p. eaaq1155.
56. Kummer, M.P., et al., *OctoMag: An electromagnetic system for 5-DOF wireless micromanipulation.* IEEE Transactions on Robotics, 2010. **26**(6): p. 1006-1017.
57. Zhang, L., et al., *Artificial bacterial flagella: Fabrication and magnetic control.* Applied Physics Letters, 2009. **94**(6): p. 064107.
58. Ricotti, L., et al., *Biohybrid actuators for robotics: A review of devices actuated by living cells.* Science Robotics, 2017. **2**(12): p. eaaq0495.
59. Martel, S., *Nanorobotics for bioengineering and medical interventions.* Encyclopedia of Nanotechnology, 2014: p. 1-15.
60. Martel, S. *Advantages and limitations of the various magnetic manipulation methods of untethered agents in the human body*. in *2014 IEEE/ASME International Conference on Advanced Intelligent Mechatronics*. 2014. IEEE.
61. Palagi, S., et al., *Structured light enables biomimetic swimming and versatile locomotion of photoresponsive soft microrobots.* 2016. **15**(6): p. 647.
62. Wang, W., et al., *Autonomous motion of metallic microrods propelled by ultrasound.* 2012. **6**(7): p. 6122-6132.
63. Magdanz, V., S. Sanchez, and O.G.J.A.M. Schmidt, *Development of a sperm-flagella driven micro-bio-robot.* 2013. **25**(45): p. 6581-6588.
64. Carlsen, R.W. and M.J.S. Sitti, *Bio-hybrid cell-based actuators for microsystems.* 2014. **10**(19): p. 3831-3851.
65. Paxton, W.F., et al., *Catalytic nanomotors: autonomous movement of striped nanorods.* 2004. **126**(41): p. 13424-13431.
66. Felfoul, O., et al., *Magneto-aerotactic bacteria deliver drug-containing nanoliposomes to tumour hypoxic regions.* Nature nanotechnology, 2016. **11**(11): p. 941.
67. Martel, S. and M. Mohammadi, *Switching between magnetotactic and aerotactic displacement controls to enhance the efficacy of MC-1 magneto-aerotactic bacteria as cancer-fighting nanorobots.* Micromachines, 2016. **7**(6): p. 97.
68. Yang, G.-Z., et al., *The grand challenges of Science Robotics.* Science Robotics, 2018. **3**(14): p. eaar7650.
69. Lalande, V., et al., *In vivo demonstration of magnetic guidewire steerability in a MRI system with additional gradient coils.* Medical physics, 2015. **42**(2): p. 969-976.
70. Le, V.N., et al., *Accurate modeling and positioning of a magnetically controlled catheter tip.* Medical physics, 2016. **43**(2): p. 650-663.
71. Rafii-Tari, H., C.J. Payne, and G.-Z. Yang, *Current and emerging robot-assisted endovascular catheterization technologies: a review.* Annals of biomedical engineering, 2014. **42**(4): p. 697-715.
72. Gang, E.S., et al., *Dynamically shaped magnetic fields: initial animal validation of a new remote electrophysiology catheter guidance and control system.* Circulation: Arrhythmia and Electrophysiology, 2011. **4**(5): p. 770-777.
73. Tremblay, C., et al. *Fringe field navigation for catheterization*. in *6th European Conference of the International Federation for Medical and Biological Engineering*. 2015. Springer.

74. Ali, A., D.H. Plettenburg, and P. Breedveld, *Steerable catheters in cardiology: Classifying steerability and assessing future challenges.* IEEE Transactions on Biomedical Engineering, 2016. **63**(4): p. 679-693.
75. Carpi, F. and C. Pappone, *Stereotaxis Niobe® magnetic navigation system for endocardial catheter ablation and gastrointestinal capsule endoscopy.* Expert review of medical devices, 2009. **6**(5): p. 487-498.
76. Pappone, C., et al., *Robotic magnetic navigation for atrial fibrillation ablation.* Journal of the American College of Cardiology, 2006. **47**(7): p. 1390-1400.
77. Shamsudhin, N., et al., *Magnetically guided capsule endoscopy.* Medical physics, 2017. **44**(8): p. e91-e111.
78. Klein, L.W., et al., *Occupational health hazards of interventional cardiologists in the current decade: results of the 2014 SCAI membership survey*. Catheterization and Cardiovascular Interventions, 2015. **86**(5): p. 913-924.
79. Kerber, C.J.R., *Balloon catheter with a calibrated leak: A new system for superselective angiography and occlusive catheter therapy.* 1976. **120**(3): p. 547-550.
80. Bartynski, W. and J.J.A.J.o.N. Boardman, *Catheter angiography, MR angiography, and MR perfusion in posterior reversible encephalopathy syndrome.* 2008. **29**(3): p. 447-455.
81. Dellimore, K.H., et al., *A review of catheter related complications during minimally invasive transcatheter cardiovascular intervention with implications for catheter design.* 2014. **5**(3): p. 217-232.
82. Hessel, S.J., D.F. Adams, and H.L.J.R. Abrams, *Complications of angiography.* 1981. **138**(2): p. 273-281.
83. Taliercio, C.P., et al., *Risks for renal dysfunction with cardiac angiography.* 1986. **104**(4): p. 501-504.
84. Maecken, T. and T.J.C.c.m. Grau, *Ultrasound imaging in vascular access.* 2007. **35**(5): p. S178-S185.
85. Kos, S., et al., *MR-guided endovascular interventions: a comprehensive review on techniques and applications.* 2008. **18**(4): p. 645-657.
86. Bock, M. and F.K.J.J.o.M.R.I.A.O.J.o.t.I.S.f.M.R.i.M. Wacker, *MR-guided intravascular interventions: Techniques and applications.* 2008. **27**(2): p. 326-338.
87. Dehmer, G.J., et al., *Anticoagulation with heparin during cardiac catheterization and its reversal by protamine.* 1987. **13**(1): p. 16-21.
88. Kessler, R., et al., *Patient body weight-tailored contrast medium injection protocol for the craniocervical vessels: a prospective computed tomography study.* 2014. **9**(2): p. e88867.
89. Roguin, A., et al., *Brain and neck tumors among physicians performing interventional procedures.* The American journal of cardiology, 2013. **111**(9): p. 1368-1372.
90. Vano, E., et al., *Radiation-associated lens opacities in catheterization personnel: results of a survey and direct assessments.* Journal of Vascular and Interventional Radiology, 2013. **24**(2): p. 197-204.
91. Alexandre, D., et al., *Wearing lead aprons in surgical operating rooms: ergonomic injuries evidenced by infrared thermography.* 2017. **209**: p. 227-233.
92. Association, A.M., *CPT Professional 2018*. 2017: American Medical Association.
93. Chuang, V., et al., *Superselective catheterization technique in hepatic angiography.* 1983. **141**(4): p. 803-811.

94. Matsui, O., et al., *Interventional oncology: new options for interstitial treatments and intravascular approaches: superselective TACE using iodized oil for HCC: rationale, technique and outcome.* 2010. **17**(4): p. 407-409.
95. Wang, M.Q., et al., *Treatment of symptomatic polycystic liver disease: transcatheter super-selective hepatic arterial embolization using a mixture of NBCA and iodized oil.* 2013. **38**(3): p. 465-473.
96. Brisman, J.L., J.K. Song, and D.W.J.N.E.j.o.m. Newell, *Cerebral aneurysms.* 2006. **355**(9): p. 928-939.
97. Homma, H., et al., *A novel arterial infusion chemotherapy for the treatment of patients with advanced pancreatic carcinoma after vascular supply distribution via superselective embolization.* 2000. **89**(2): p. 303-313.
98. Funaki, B., et al., *Superselective microcoil embolization of colonic hemorrhage.* 2001. **177**(4): p. 829-836.
99. Shields, C.L., et al., *Superselective catheterization of the ophthalmic artery for intraarterial chemotherapy for retinoblastoma.* 2009. **29**(8): p. 1207-1209.
100. Ginat, D.T., et al., *Transcatheter renal artery embolization: clinical applications and techniques.* 2009. **12**(4): p. 224-239.
101. Pelage, J.-P., et al., *Fibroid-related menorrhagia: treatment with superselective embolization of the uterine arteries and midterm follow-up.* 2000. **215**(2): p. 428-431.
102. Kasirajan, K., et al., *Technique and results of transfemoral superselective coil embolization of type II lumbar endoleak.* 2003. **38**(1): p. 61-66.
103. Pouponneau, P., G. Bringout, and S.J.A.o.b.e. Martel, *Therapeutic magnetic microcarriers guided by magnetic resonance navigation for enhanced liver chemoembilization: a design review.* 2014. **42**(5): p. 929-939.
104. Raza, A. and G.K.J.W.j.o.g.W. Sood, *Hepatocellular carcinoma review: current treatment, and evidence-based medicine.* 2014. **20**(15): p. 4115.
105. Michaud, F., et al., *Selective embolization with magnetized microbeads using magnetic resonance navigation in a controlled-flow liver model.* Medical physics, 2019. **46**(2): p. 789-799.
106. Bigot, A., et al., *Magnetic resonance navigation of a bead inside a three-bifurcation pmma phantom using an imaging gradient coil insert.* IEEE Transactions on Robotics, 2014. **30**(3): p. 719-727.
107. Latulippe, M. and S. Martel, *Dipole field navigation: Theory and proof of concept.* IEEE Transactions on Robotics, 2015. **31**(6): p. 1353-1363.
108. Taherkhani, S., et al., *Covalent binding of nanoliposomes to the surface of magnetotactic bacteria for the synthesis of self-propelled therapeutic agents.* 2014. **8**(5): p. 5049-5060.
109. Tabatabaei, S.N., et al., *Hyperthermia of magnetic nanoparticles allows passage of sodium fluorescein and Evans blue dye across the blood–retinal barrier.* International Journal of Hyperthermia, 2016. **32**(6): p. 657-665.
110. Tabatabaei, S.N., et al., *Remote control of the permeability of the blood–brain barrier by magnetic heating of nanoparticles: a proof of concept for brain drug delivery.* Journal of controlled release, 2015. **206**: p. 49-57.
111. Seppenwoolde, J.H., et al., *Fully MR-guided hepatic artery catheterization for selective drug delivery: A feasibility study in pigs.* 2006. **23**(2): p. 123-129.

112. Kos, S., et al., *First magnetic resonance imaging-guided aortic stenting and cava filter placement using a polyetheretherketone-based magnetic resonance imaging-compatible guidewire in swine: proof of concept.* 2009. **32**(3): p. 514-521.
113. Elgort, D.R., et al., *Image-guided and-monitored renal artery stenting using only MRI.* 2006. **23**(5): p. 619-627.
114. Kos, S., et al., *Feasibility of Real-Time Magnetic Resonance–Guided Angioplasty and Stenting of Renal Arteries in Vitro and in Swine, Using a New Polyetheretherketone-Based Magnetic Resonance–Compatible Guidewire.* 2009. **44**(4): p. 234-241.
115. Bakker, C.J., et al., *MR-guided endovascular interventions: susceptibility-based catheter and near-real-time imaging technique.* 1997. **202**(1): p. 273-276.
116. Razavi, R., et al., *Cardiac catheterisation guided by MRI in children and adults with congenital heart disease.* 2003. **362**(9399): p. 1877-1882.
117. Paetzel, C., et al., *Magnetic resonance-guided percutaneous angioplasty of femoral and popliteal artery stenoses using real-time imaging and intra-arterial contrast-enhanced magnetic resonance angiography.* 2005. **40**(5): p. 257-262.
118. Clogenson, H.C., J.J.J.o.I. vd Dobbelsteen, and I. Radiology, *Catheters and guide wires for interventional MRI: are we there yet?* 2016. **2**: p. 28.
119. Kos, S., et al., *MR-compatible polyetheretherketone-based guide wire assisting MR-guided stenting of iliac and supraaortic arteries in swine: Feasibility study.* 2009. **18**(3): p. 181-188.
120. Saikus, C.E. and R.J.J.J.C.I. Lederman, *Interventional cardiovascular magnetic resonance imaging: a new opportunity for image-guided interventions.* 2009. **2**(11): p. 1321-1331.
121. Omary, R.A., et al., *Real-time MR imaging-guided passive catheter tracking with use of gadolinium-filled catheters.* 2000. **11**(8): p. 1079-1085.
122. Rhode, K.S., et al., *A system for real-time XMR guided cardiovascular intervention.* 2005. **24**(11): p. 1428-1440.
123. Markelj, P., et al., *A review of 3D/2D registration methods for image-guided interventions.* 2012. **16**(3): p. 642-661.
124. McRobbie, D., *Occupational exposure in MRI.* The British journal of radiology, 2012. **85**(1012): p. 293-312.
125. Grady, M.S., et al., *Experimental study of the magnetic stereotaxis system for catheter manipulation within the brain.* Journal of neurosurgery, 2000. **93**(2): p. 282-288.
126. Polygerinos, P., et al., *MRI-compatible fiber-optic force sensors for catheterization procedures.* 2010. **10**(10): p. 1598-1608.
127. Polygerinos, P., et al., *MRI-compatible intensity-modulated force sensor for cardiac catheterization procedures.* 2011. **58**(3): p. 721-726.
128. Yokoyama, K., et al., *Novel contact force sensor incorporated in irrigated radiofrequency ablation catheter predicts lesion size and incidence of steam pop and thrombus.* 2008. **1**(5): p. 354-362.
129. Polygerinos, P., et al., *Triaxial catheter-tip force sensor for MRI-guided cardiac procedures.* 2013. **18**(1): p. 386-396.
130. Chi, W., et al. *A learning based training and skill assessment platform with haptic guidance for endovascular catheterization*. in *2017 IEEE International Conference on Robotics and Automation (ICRA)*. 2017. IEEE.

131. Rafii-Tari, H., et al., *Objective assessment of endovascular navigation skills with force sensing.* 2017. **45**(5): p. 1315-1327.
132. Rafii-Tari, H., et al. *Towards automated surgical skill evaluation of endovascular catheterization tasks based on force and motion signatures*. in *2015 IEEE International Conference on Robotics and Automation (ICRA)*. 2015. IEEE.
133. Riga, C.V., et al., *Robot-assisted fenestrated endovascular aneurysm repair (FEVAR) using the Magellan system.* 2013. **24**(2): p. 191-196.
134. Kato, T., et al., *Tendon-driven continuum robot for endoscopic surgery: preclinical development and validation of a tension propagation model.* 2015. **20**(5): p. 2252-2263.
135. Qi, P., et al. *Towards kinematic modeling of a multi-DOF tendon driven robotic catheter*. in *2014 36th Annual International Conference of the IEEE Engineering in Medicine and Biology Society*. 2014. IEEE.
136. Fu, Y., et al., *Steerable catheters in minimally invasive vascular surgery*. 2009. **5**(4): p. 381-391.
137. Konh, B., S. Karimi, and S. Miller. *Feasibility study of an active soft catheter actuated by SMA wires*. in *Smart Structures and NDE for Industry 4.0*. 2018. International Society for Optics and Photonics.
138. Edelmann, J., A.J. Petruska, and B.J. Nelson, *Magnetic control of continuum devices.* The International Journal of Robotics Research, 2017. **36**(1): p. 68-85.
139. Rubin, M.B., *Cosserat theories: shells, rods and points*. Vol. 79. 2000: Springer Science & Business Media.
140. Tang, W., et al., *A stable and real-time nonlinear elastic approach to simulating guidewire and catheter insertions based on cosserat rod.* IEEE Transactions on Biomedical Engineering, 2012. **59**(8): p. 2211-2218.
141. Tunay, I., *Spatial continuum models of rods undergoing large deformation and inflation.* IEEE Transactions on Robotics, 2013. **29**(2): p. 297-307.
142. Webster III, R.J. and B.A.J.T.I.J.o.R.R. Jones, *Design and kinematic modeling of constant curvature continuum robots: A review.* 2010. **29**(13): p. 1661-1683.
143. Huang, D., et al., *A new approach to haptic rendering of guidewires for use in minimally invasive surgical simulation.* Computer Animation and Virtual Worlds, 2011. **22**(2-3): p. 261-268.
144. Wang, H., et al., *A robust and fast approach to simulating the behavior of guidewire in vascular interventional radiology.* Computerized Medical Imaging and Graphics, 2015. **40**: p. 160-169.
145. Khan, E.M., et al., *First experience with a novel robotic remote catheter system: Amigo™ mapping trial.* 2013. **37**(2): p. 121-129.
146. Smitson, C.C., et al., *Safety and Feasibility of a Novel, Second-Generation Robotic-Assisted System for Percutaneous Coronary Intervention: First-in-Human Report.* 2018. **30**(4): p. 152-156.
147. Chapra, S.C. and R.P. Canale, *Numerical methods for engineers*. 2010: Boston: McGraw-Hill Higher Education.
148. Azizi, A., C. Tremblay, and S. Martel. *Magnetic Fringe Field Navigation of a guidewire based on Thin Plate Spline modeling*. in *2016 IEEE International Conference on Automation Science and Engineering (CASE)*. 2016. IEEE.
149. Rosensweig, R.E., *Ferrohydrodynamics*. 2013: Courier Corporation.

150. Abbott, J.J., et al., *Modeling magnetic torque and force for controlled manipulation of soft-magnetic bodies.* IEEE Transactions on Robotics, 2007. **23**(6): p. 1247-1252.
151. D'haeseleer, W.D., et al., *Flux coordinates and magnetic field structure: a guide to a fundamental tool of plasma theory*. 2012: Springer Science & Business Media.
152. Azizi, A., C. Tremblay, and S. Martel. *Trajectory planning for vascular navigation from 3D angiography images and vessel centerline data*. in *2017 International Conference on Manipulation, Automation and Robotics at Small Scales (MARSS)*. 2017. IEEE.
153. Davies, E.R., *Machine vision: theory, algorithms, practicalities*. 2004: Elsevier.
154. Gen, M., L.J.W.E.o.C.S. Lin, and Engineering, *Genetic algorithms.* 2007: p. 1-15.
155. Hassan, R., et al. *A comparison of particle swarm optimization and the genetic algorithm*. in *46th AIAA/ASME/ASCE/AHS/ASC structures, structural dynamics and materials conference*. 2005.
156. Shigley, J.E., C.R. Mischke, and R.G. Budynas, *Mechanical Engineering Design, International*. 1989: Mc-Graw Hill Book Co., Singapore.
157. Li, N., et al., *MRI-compatible injection system for magnetic microparticle embolization.* 2018.
158. Rymansaib, Z., P. Iravani, and M.N. Sahinkaya. *Exponential trajectory generation for point to point motions*. in *2013 IEEE/ASME International Conference on Advanced Intelligent Mechatronics*. 2013. IEEE.
159. Swindle, M.M. and A.C. Smith, *Swine in the laboratory: surgery, anesthesia, imaging, and experimental techniques*. 2015: CRC press.
160. Basciano, C.A., et al., *Computer modeling of controlled microsphere release and targeting in a representative hepatic artery system.* 2010. **38**(5): p. 1862-1879.
161. Sebben, G.A., et al., *Variations of hepatic artery: anatomical study on cadavers.* 2013. **40**(3): p. 221-226.
162. Heunis, C., et al., *Improved Magnetic Steering, Actuation, and Image-Guided Surgical Instruments.* 2018. **1070**(9932/18): p. 2.
163. Jeon, S., et al., *A magnetically controlled soft microrobot steering a guidewire in a three-dimensional phantom vascular network.* 2018. **6**(1): p. 54-68.
164. Oliveira, J., R. Miranda, and F.B. Fernandes, *Welding and joining of NiTi shape memory alloys: A review.* Progress in Materials Science, 2017. **88**: p. 412-466.

APPENDIX A DEVELOPMENTS IN SUMMARY

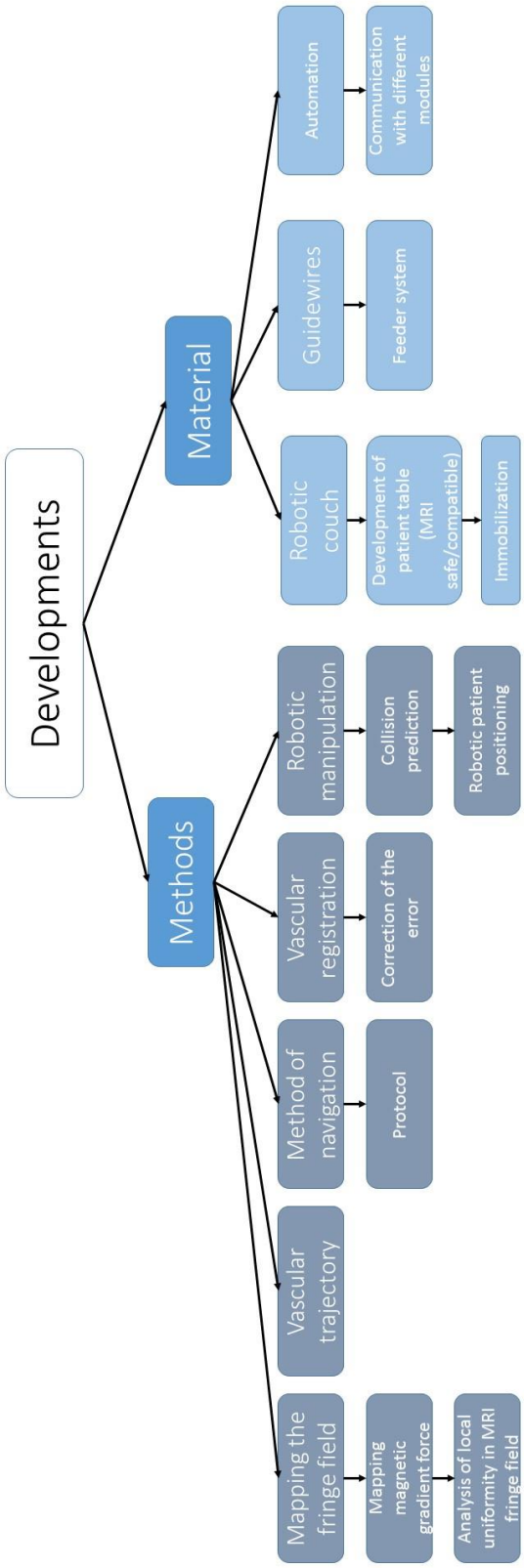

APPENDIX B THIN PLATE SPLINE INTERPOLATION

By having a set of $\{V_i\}$ data corresponding to a set of samples with coordinates (x_i, y_i) with i=1, 2, ..., p , the TPS method generates a function represented by Eq. (1):

$$f(x,y) = a_1 + a_x x + a_y y + \sum_{i=1}^{p} \omega_i U(\|(x_i, y_i) - (x, y)\|)$$

In (3), U (r) = r^2 log (r) and ω_i and a_i are the constant coefficients of the TPS function which minimizes bending energy of Eq. (2).

$$I_f = \iint_{R^2} \left(f_{xx}^2 + f_{xy}^2 + f_{yy}^2\right) dx.dy$$

In order that (x, y) have square integrable second order derivatives, it needs to satisfy the following conditions:

$$\sum_{i=1}^{p} \omega_i = 0 \quad , \quad \sum_{i=1}^{p} \omega_i \, x_i = \sum_{i=1}^{p} \omega_i \, y_i = 0 \quad and \quad f(x_i, y_i) = V_i$$

These conditions yield a linear system Eq. (3) to calculate TPS function coefficients.

$$\begin{bmatrix} K & P \\ P^T & O \end{bmatrix} \begin{bmatrix} \omega \\ a \end{bmatrix} = \begin{bmatrix} V \\ 0 \end{bmatrix}$$

Where $K_{ij} = U(\|(x_i , y_i) - (x_j , y_j)\|)$, O is a 3 × 3 matrix of zeros, o is a column of 3 elements with zero value, ω and V are column vectors formed from ω_i and V_i elements, respectively, $a = [a_1 , a_x, a_y]^T$ and

$$P = \begin{bmatrix} 1 & x_1 & y_1 \\ \vdots & \vdots & \vdots \\ 1 & x_p & y_p \end{bmatrix}$$

Solving Eq. (3) gives us the coefficients required to generate the TPS function.

APPENDIX C FORMULATION FOR MAGNETIC GRADIENT FORCE

The formula for calculation of the magnetic gradient force is expressed by following equation.

$$F = \mu_0 (M.\nabla)\mathrm{H}$$

In this equation F (N) is the force and ∇ is the gradient operator. The expression of $(M.\nabla)\mathrm{H}$ can be rewritten as follow:

$$(M.\nabla)\mathrm{H} = \nabla(\mathrm{M}.\mathrm{H}) - \mathrm{H}.\nabla\mathrm{M} - \mathrm{M} \times (\nabla \times \mathrm{H}) - \mathrm{H} \times (\nabla \times \mathrm{M})$$

For the constant M, it simplifies to

$$(M.\nabla)\mathrm{H} = \nabla(\mathrm{M}.\mathrm{H}) - \mathrm{M} \times (\nabla \times \mathrm{H})$$

Which under the circumstance of no flow of electrical current through the region that is occupied by the body, $\nabla \times \mathrm{H} = 0$ and thus the magnetic gradient force for constant M can be calculated from the following equation:

$$F = \mu_0 v \begin{bmatrix} \frac{\partial}{\partial \mathrm{x}} H^T \\ \frac{\partial}{\partial \mathrm{y}} H^T \\ \frac{\partial}{\partial \mathrm{z}} H^T \end{bmatrix} M$$

References:

Rosensweig, Ronald E. Ferrohydrodynamics. Courier Corporation, 2013.

Abbott, J.J., et al., *Modeling magnetic torque and force for controlled manipulation of soft-magnetic bodies.* IEEE Transactions on Robotics, 2007. **23**(6): p. 1247-1252.

APPENDIX D SCHEMATIC OF THE METHOD OF VASCULAR REGISTRATION (CALIBRATION)

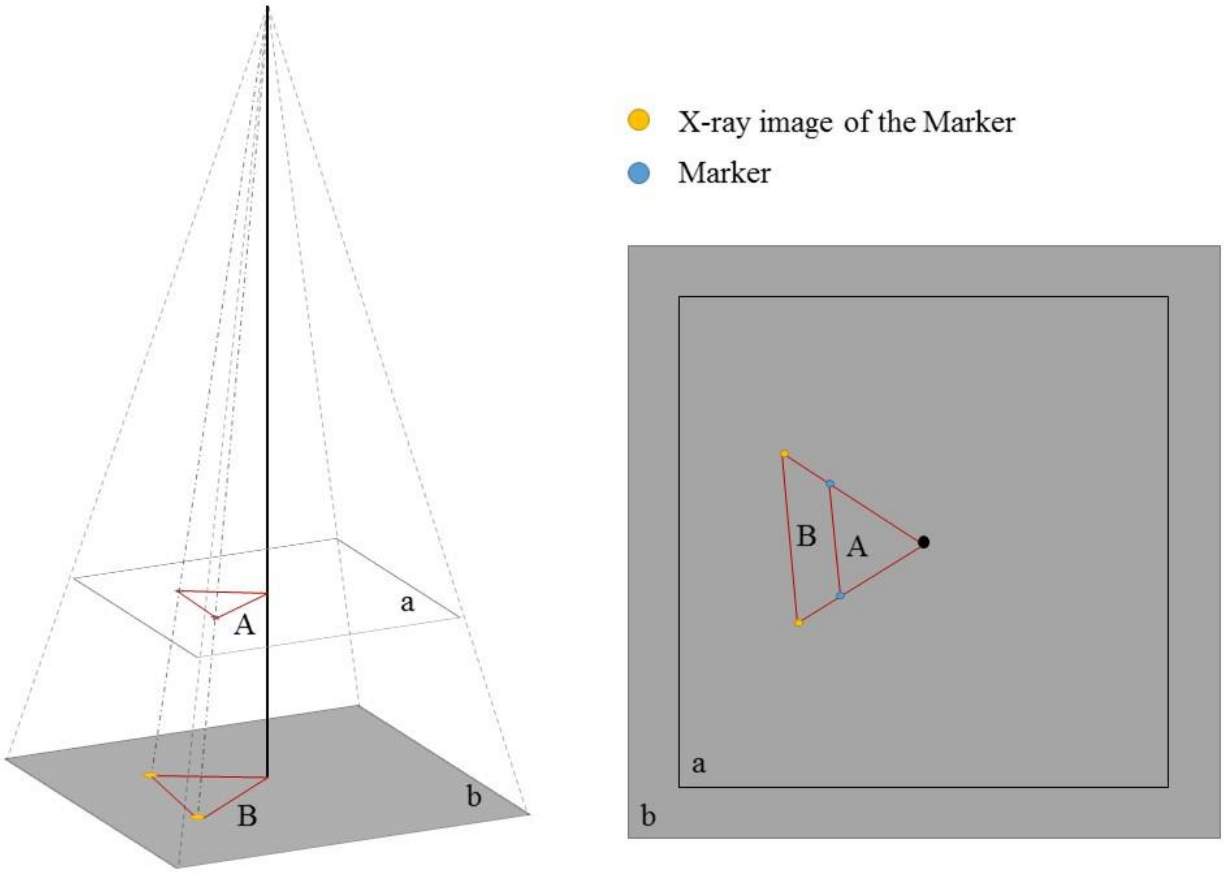

APPENDIX E FFN APPLICATION (SCREENSHOTS)

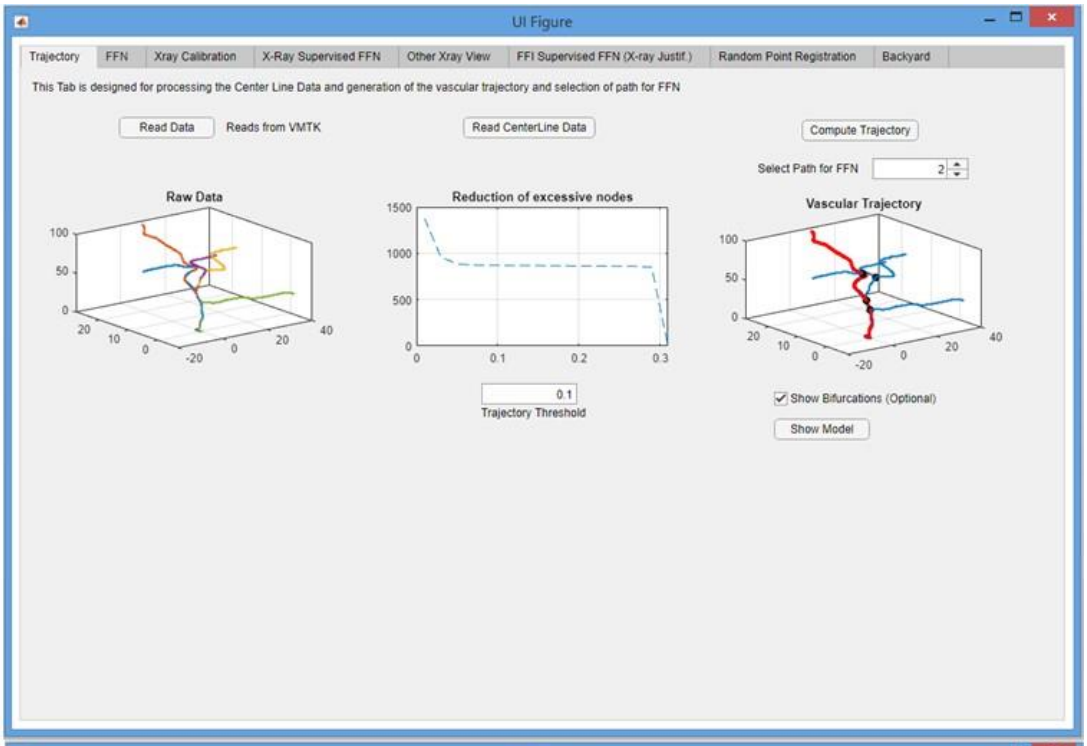

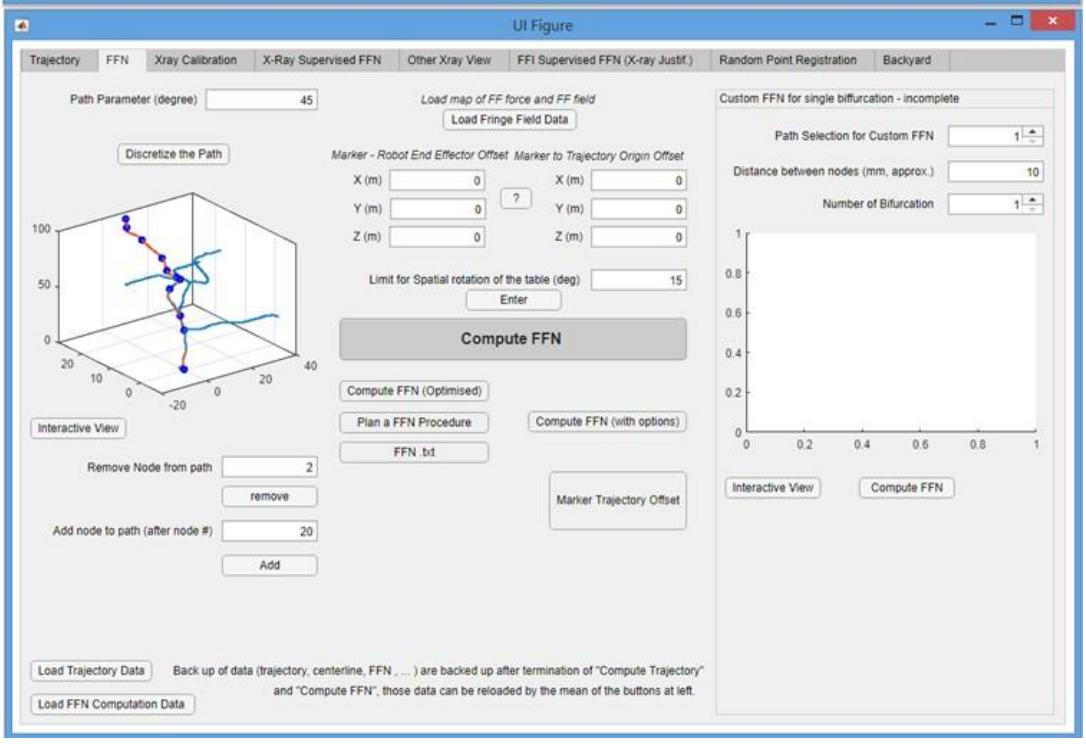

APPENDIX F VSM MEASUREMENT OF SPRINGS

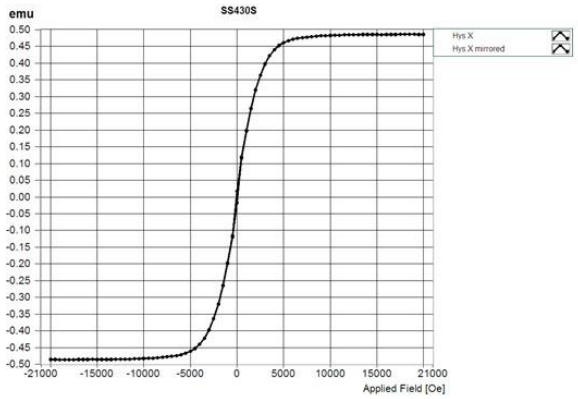

System ID: EV X; SN: XXXXXXXX; Customer: XXXXXXXXX; first started on: Thursday, September 15, 2011
Date and time of last calibration: Thursday, March 22, 2018 10:37:02
Operator: Djamel
Sample name: SS430S
test
Data filename: C:\vsm-lv\Djamel\data\SS430S\SS430S.VHD
Start of measurement: 10:53:54, Thursday, March 22, 2018
Field Angle: -0.00 [deg]

Total measurement time: 00:16:19

Parameters

	Upward Part	Downward part	Average	Parameter definition
Hysteresis Loop				Hysteresis Parameters
Hc Oe	57.553E+0	-57.553E+0	57.553E+0	Coercive Field: Field at which M/H changes sign
Mr emu	-15.249E-3	15.249E-3	15.249E-3	Remanent Magnetization: M at H=0
S	0.031	0.031	0.031	Squareness: Mr/Ms
S*	0.087	0.087	0.087	1-(Mr/Hc)(1/slope at Hc)
Hn Oe	-5017.20	5030.63	5023.92	Nucleation field: field where M starts to drop from saturation (M=0.95 M
Hs Oe	5056.92	-5043.68	5050.30	Saturation field: field at which M reaches 0.95 Ms
SFD	1.00	1.00	1.00	Switching field distribution: dH/Hc, where Hd is the field between 0.5 Mr and

MAGNETICS

MicroSense EasyVSM Software Version EasyVSM 20150226-01

(A)

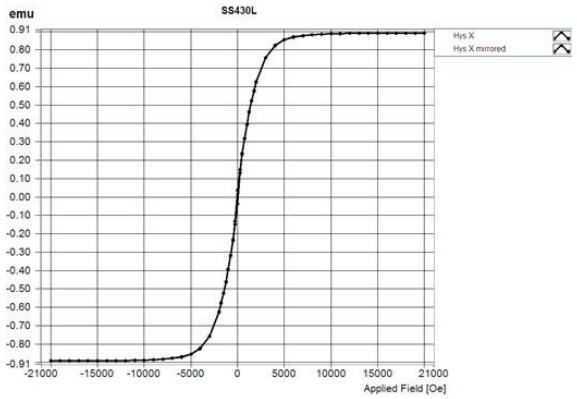

System ID: EV X; SN: XXXXXXXX; Customer: XXXXXXXXX; first started on: Thursday, September 15, 2011
Date and time of last calibration: Thursday, March 22, 2018 10:37:02
Operator: Djamel
Sample name: SS430L
test
Data filename: C:\vsm-lv\Djamel\data\SS430L\SS430L.VHD
Start of measurement: 11:23:58, Thursday, March 22, 2018
Field Angle: -0.00 [deg]

Total measurement time: 00:12:03

Parameters

	Upward Part	Downward part	Average	Parameter definition
Hysteresis Loop				Hysteresis Parameters
Hc Oe	53.390E+0	-53.390E+0	53.390E+0	Coercive Field: Field at which M/H changes sign
Mr emu	-36.085E-3	36.085E-3	36.085E-3	Remanent Magnetization: M at H=0
S	0.041	0.040	0.040	Squareness: Mr/Ms
S*	0.108	0.108	0.108	1-(Mr/Hc)(1/slope at Hc)
Hn Oe	-4729.75	4707.24	4718.49	Nucleation field: field where M starts to drop from saturation (M=0.95 M
Hs Oe	-4723.09	-4745.42	4734.25	Saturation field: field at which M reaches 0.95 Ms
SFD	1.00	1.00	1.00	Switching field distribution: dH/Hc, where Hd is the field between 0.5 Mr and

MAGNETICS

MicroSense EasyVSM Software Version EasyVSM 20150226-01

(B)

(A) and (B) are the results of VSM test of two samples of spring tightly winded with a SS 430 wire with 0.2mm diameter with the external diameter of the spring equal to 0.7mm and the weight of 3.5mg for (A) and 5mg for (B). The density of the material is 7.8gr/cm3.